A Laboratory Study of Three-Dimensional Breaking Waves

by

Ziad Zakharia

B.S., Civil Engineering
Loyola Marymount University, Los Angeles, 1993

Submitted to the Department of
Civil and Environmental Engineering
in Partial Fulfillment of the Requirements
for the Degree of

MASTER OF SCIENCE
in Civil and Environmental Engineering
at the

Massachusetts Institute of Technology

June 1995

Signature of the Author _____
Department of Civil and Environmental Engineering
May 26, 1995

Certified by _____
Heidi M. Nepf
Assistant Professor of Civil and Environmental Engineering
Thesis Advisor

Accepted by _____
Joseph M. Sussman
Chairman, Departmental Committee on Graduate Studies

A Laboratory Study of Three-Dimensional
Breaking Waves
by
Ziad Zakharia

Submitted to the Department of Civil and Environmental Engineering
on May 26, 1995 in partial fulfillment of the requirements for the
Degree of Master of Science in Civil and Environmental Engineering

ABSTRACT

Three-dimensional breaking waves are studied in a wave basin. A bi-directional frequency-modulated wave packet is generated by superposing 32 components of different frequencies. The input signal is tapered laterally to produce a 1m crest length. The packet evolves and results in a single breaker. Four different cases are run: plunger, spiller, incipient, and two-dimensional plunger. The variation of the surface elevation is recorded in a 4m x 3m region with a grid spacing of 30cm x 20cm.

Wave energy dissipation due to breaking is computed for the plunger and spiller from the spectra of the wave packet records. The two other cases, incipient and 2D plunger, are used in the analysis to characterize viscous dissipation and lateral redistribution of wave energy. For the plunger, a wave energy dissipation of 12% is obtained at the centerline, and for the spiller, a loss of 4%.

The wave steepness at the inception of breaking is 0.45 which is typical for a breaking wave generated in a short wave tank. The lateral variation of the wave steepness is also computed for the different breakers.

Thesis Advisor: Dr. Heidi M. Nepf

Title: Assistant Professor of Civil and Environmental Engineering

To Mayrig

Acknowledgments

Prior to this point, little was I aware of the number of people who have assisted in this thesis.

First, I would like to thanks my advisor, Heidi Nepf, whose enthusiasm for experimental research and keen physical insight guided me through the project. I also want to thank Chin-Hsien Wu who gave me a valuable hand in carrying out the experiments. His "research philosophy" made working with him a great learning experience. Early on in the project, Eng-Soon Chan's input on fine-tuning the breaking wave is extremely appreciated. Also, thanks to Hoang Tran and Paul Moody, not only for being great neighbors in the wave basin, but also for their assistance in keeping the basin up and running.

Immeasurable gratitude goes towards my parents and my brother, Khaled, who have lent me their ears at all times. Without their love and support, I would not have reached as far as I have.

When Rudyard Kipling advised all youth, "If all men count with you, but none too much", as examples of those who should, he surely had in mind the likes of Boutros Abboud-Klink and Ahmad Kreydieh. Thank you both for your friendship and support.

This research was funded by Tau Beta Pi, Schoettler, and National Science Foundation Graduate Fellowships.

TABLE OF CONTENTS

LIST OF FIGURES

LIST OF TABLES

CHAPTER 1

Introduction

1.1 Importance of Breaking Waves

Breaking waves play a key role in the complex exchanges across the air-sea interface. There are fluxes of momentum, energy, and gas from the atmosphere into the oceans, and breaking activity plays a major role in these transfers. An application to understanding the breaking activity is also found in the area of remote sensing. Images of the ocean surface taken from satellites are used to extract information on the basic air-sea variables. Such variables include data on wave heights, global distribution of ocean wind stress, and wind direction. Breaking activity can have an effect on the interpretation of these data.

A more prominent role for investigation is the turbulence associated with the breaking wave. A wave group propagating along the surface of the ocean loses a fraction of its energy upon breaking. About 70% of the energy lost is accounted for in surface currents while the remaining 30% is transferred to turbulent kinetic energy beneath the free surface (Rapp and Melville, 1990). This turbulence enhances vertical mixing. Wave breaking is a mechanism in which the atmosphere imparts momentum and energy to the ocean; however, some momentum is imparted directly from the wind due to drag. In addition, air entrainment is also associated with wave breaking. The bubble cloud forming beneath the breaker enhances the flux of gases across the air-sea interface. The importance of this phenomena is seen by the example of CO_2. If there is a greater of carbon dioxide from the atmosphere into the oceans due to breaking, then that could retard a global warming effect (Csanady, 1990). A study has also been done to estimate the percentage of whitecap on the ocean surface (Toba and Chen, 1973). It was found that even for moderate values of wind speed, an estimate of 1% of the total ocean surface is covered by whitecap at any given instant.

In addition to the wind, there are other mechanisms responsible for local increase in wave height. One of which is wave focusing. The wave focusing mechanism involves fast carrier waves propagating through a wave envelope and overtaking the slower higher frequency waves. The effect is an increase in the wave height to a point of breaking. Experiments have been done that show that wave-wave interactions alone in a three-

dimensional sea state can give rise to a significant amount of whitecapping in the absence of wind (Kjeldsen, 1984). So, although wind effects are not used in generating the breaking waves in the basin, the wave focusing approach is taken as being an equivalently good model for wave breaking in the field. In reality, both wind and wave-wave interaction have an effect on breaking. A more in-depth discussion on frequency focusing is given in Chapter 2.

1.2 Breaker Classification

The experiments described here deal with deep-water breaking waves for which the depth is greater than half the wavelength. There are three types of deep-water breaking waves: plungers, spillers, and incipients (figure 1.1). The classification is based on observation. The most vigorous of the these is the plunger. A plunging wave forms a tube of air as it rolls over (see figure 1.1). Upon breaking, a considerable amount of splashing takes place, and the tube of air is entrained below the free surface. In the event of a spiller, whitecap is observed but a tube is not formed. The white foam formed initially at the crest slides down the front face of the wave. The third case is not quite a breaking wave; it is the wave which is on the verge of breaking (i.e. spilling) but does not quite break.

1.3 Steady versus Unsteady Breakers

Steady breakers are typically generated in a laboratory by towing a submerged hydrofoil in a steady, uniform current (Banner & Melville, 1976; Banner & Fooks, 1985; Banner & Cato, 1988; and Banner, 1990). Based on these experiments, models for the later stages of breaking have been proposed. One of them is based on a turbulent gravity current riding down the forward slope of the wave (Longuet-Higgins, 1974). This model predicts that the energy dissipation over one wave period is 12% of the energy in the base wave. Steady breakers are most applicable to spillers.

Unsteady breakers have also been generated in several studies (Kjeldsen and Myrhaug, 1978; Bonmarin 1989; She et al, 1992), by focusing the wave energy in space to cause a local increase in energy density. In a flume, this can be done by either using a converging channel wall (Van Dorn, 1975) or by longitudinal focusing caused by frequency dispersion (Rapp and Melville, 1990). In a wave basin, many wave paddles can

Plunger

Spiller

Incipient

Figure 1.1 Schematic of plunger, spiller, and incipient breakers.

generate a breaking wave by spatially focusing the energy at a fixed center point (She et al, 1994).

The most complete study is that of Rapp and Melville (1990) which uses two-dimensional frequency focusing to produce breaking. The technique adopted for the present study also uses frequency focusing but with a three-dimensional evolution of the wave packet. (Note that future references to the work done by Rapp and Melville (1990) will be abbreviated as RM).

1.4 Current Project

The research was carried out in the newly developed three-dimensional Robert J. Gunther wave basin housed in the Parsons Laboratory at the Massachusetts Institute of Technology. The three dimensionality of the wave generated in the current project makes it a more realistic representation of wave breaking in nature. There are advantages in running the experiment in the laboratory rather than out in the field due to the difficulty of following a wave packet as it propagates in the open ocean. Moreover, since wave breaking is a highly nonlinear process, analytical (Longuet-Higgins, 1980; Greenhow, 1983) and numerical (Dommermuth et al, 1988) work have been able to successfully describe the evolution of the wave packet up to the point of breaking but not beyond.

This project is based on work done by Rapp and Melville (1990). The set of experiments run by RM were extensive; however, their work was two-dimensional since the experiments were conducted in a long but narrow flume which dictated uniform conditions in the lateral direction. The main point of this study are the characterization of the wave packets and the energy dissipation that occurs during breaking. The loss of wave energy due to breaking is estimated by differencing the energy of the wave packet before and after breaking. The addition of the third dimension adds considerable complexity to the problem since the wave envelope is now allowed to propagate in two dimensions across the water surface.

The first step of this project is to generate a breaker. The next is to measure the displacement of the free surface throughout the wave basin. This information is used for the spectral analysis from which preliminary estimates of energy dissipation are computed.

CHAPTER 2

THE EXPERIMENT

2.1 Experimental Facility

The experiment is conducted at the Parsons Lab at MIT in the Robert J. Gunther Wave Basin (figure 2.1). The wave basin is 10m x 17m. It allows a depth of water of up to 1m. An array of 47 independently programmed paddles are lined up along one side. Each paddle has its own hydraulic connection, servo motor, and control electronics. The paddles are supported from above by an aluminum structure, are attached to stainless steel rods from the top, and are guided by a stainless steel rail from the bottom. The separation between the paddles is about 2mm. Each paddle is 1ft. wide and has a stroke of up to 2ft. The paddles can oscillate with a frequency of up to 3Hz and are capable of receiving data at up to 100Hz. An absorber beach is on the opposite side of the basin. It has a slope of 1/6 with an amplitude reflection coefficient of about 12%. The facility is also comprised of two other rooms. The hydraulic room houses the cooling system and the eight pumps that drive the paddles. The second room is the control room which is the main station from where all tasks are executed. The main system that runs the wave basin is an IBM PC interfaced to the control box which houses the control cards. Besides the control of the wavemaker, the experiment is run from a Dell Optiplex 486/100MHz computer.

2.2 Software: Atlantis and Pipeline

The software Atlantis that controls the operation of the paddles was written and developed in our lab by Hoang Tran. It can run the paddles either in real time or from a data file. A data file is typically used if the wavemaker is generating waves that are not sinusoidal or circular, and if it is running for a short enough duration so that there is enough memory to store all the information in the data file. The breaking wave could not be run in real time unless more code was added to Atlantis. But luckily, the breaking wave is a transient phenomena and hence does not require the wavemaker to be running for more than 20 seconds. Consequently, the breaker can be run from a data file. The breaking wave program, Pipeline (Appendix 1), was written to generate the required file

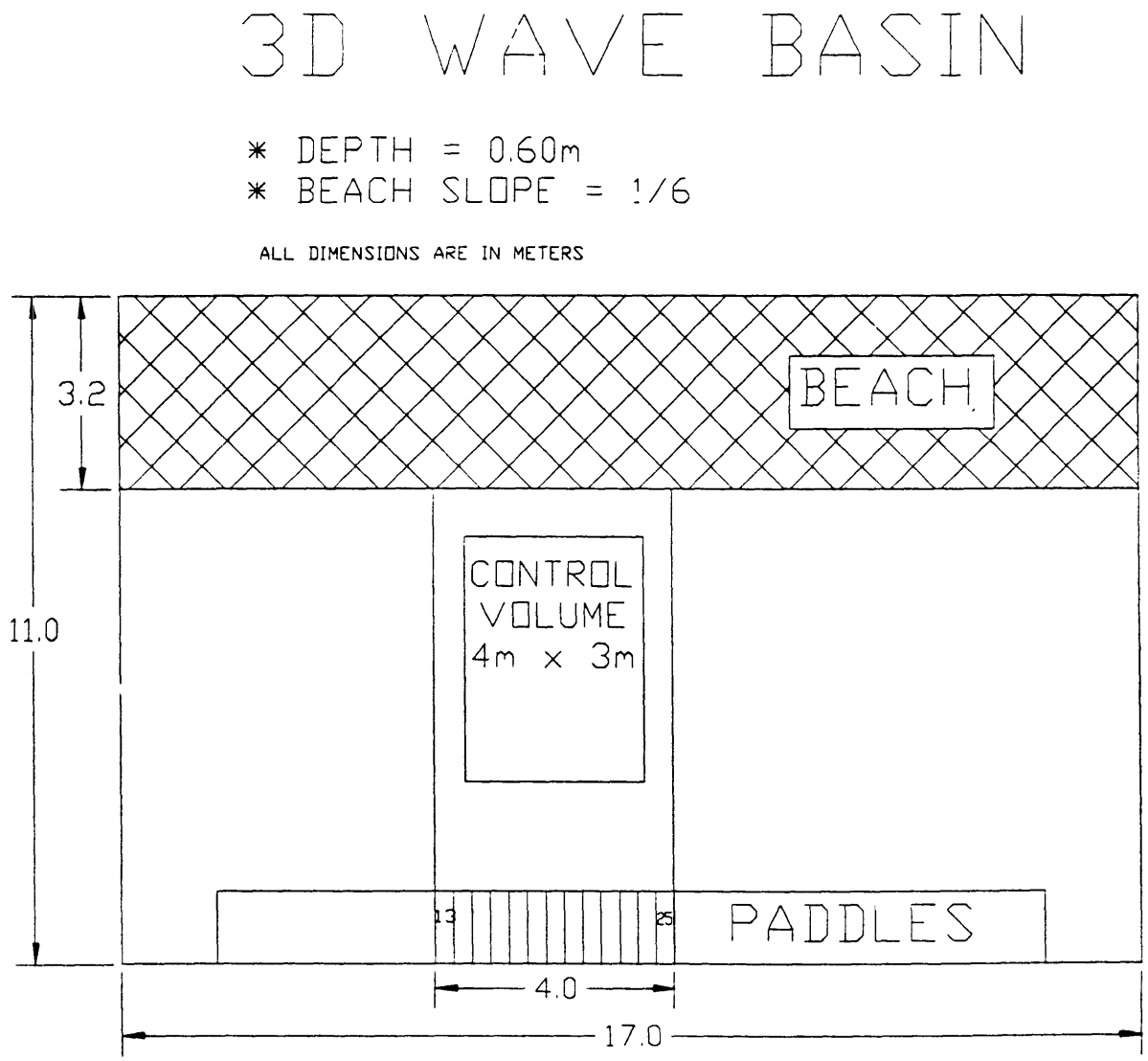

Figure 2.1 Robert J. Gunther wave basin.

that described the motion of the paddles, or the input signal to the paddles. The signal is sampled at 25Hz and has a duration of 20 seconds. The output of Pipeline is a data file that contains 47 x 500 numbers. The 47 columns dictate the motion of each individual paddle (although only 13 are in motion), and the 500 rows describe the motion of each paddle for 20 seconds at a sample rate of 25Hz (although the actual signal ends up being 11.5 seconds long). Figure 2.2 includes a flowchart of the above description and of the surface elevation sampling process that will be discussed in more detail next.

2.3 Experimental Section

The experiment section is 4m wide. Thirteen paddles are used to generate the breaking wave. Channel walls defined the study area and ensure that the flow field generated is symmetric about the centerline of the breaker. Although, as is discussed later on, some wall effects have to be taken into account, it is essential in defining the flow field that the breaker and the associated surface displacement be symmetric. Wooden panels were built from sheets of marine plywood and were placed in the basin to form channel walls. The panels were weighed down by cinder blocks placed on the outer side of the channel.

2.4 Wave Gauges and Wavemaker Repeatability

The surface displacement is recorded using resistance-type wave gauges. The wave gauges are 40cm in length. A voltage reading, which is proportional to the resistance of the exposed metal tubing (Ohm's law), is converted to a surface elevation value by a cm/V ratio. The gauges are equipped with a sensor that accounts for variability in salinity and temperature of the water. Seven wave gauges are used in this experiment. Four of them are from DHI, the Danish Hydraulic Institute, Inc. The other three along with the amplifier are from Protecno, Inc., an Italian company. The data acquisition system used is the DAS1602 board from Keithley Metrabyte, Inc. The sampling software however was developed in our lab. This software allows sampling of up to 8 channels simultaneously. Only 7 are needed for the experiment. The program prompts for the sampling rate of the wave gages and for the duration of sampling. The resolution is better than a tenth of a millimeter. The wave gauges are linear in terms of the surface elevation-to-volts conversion.

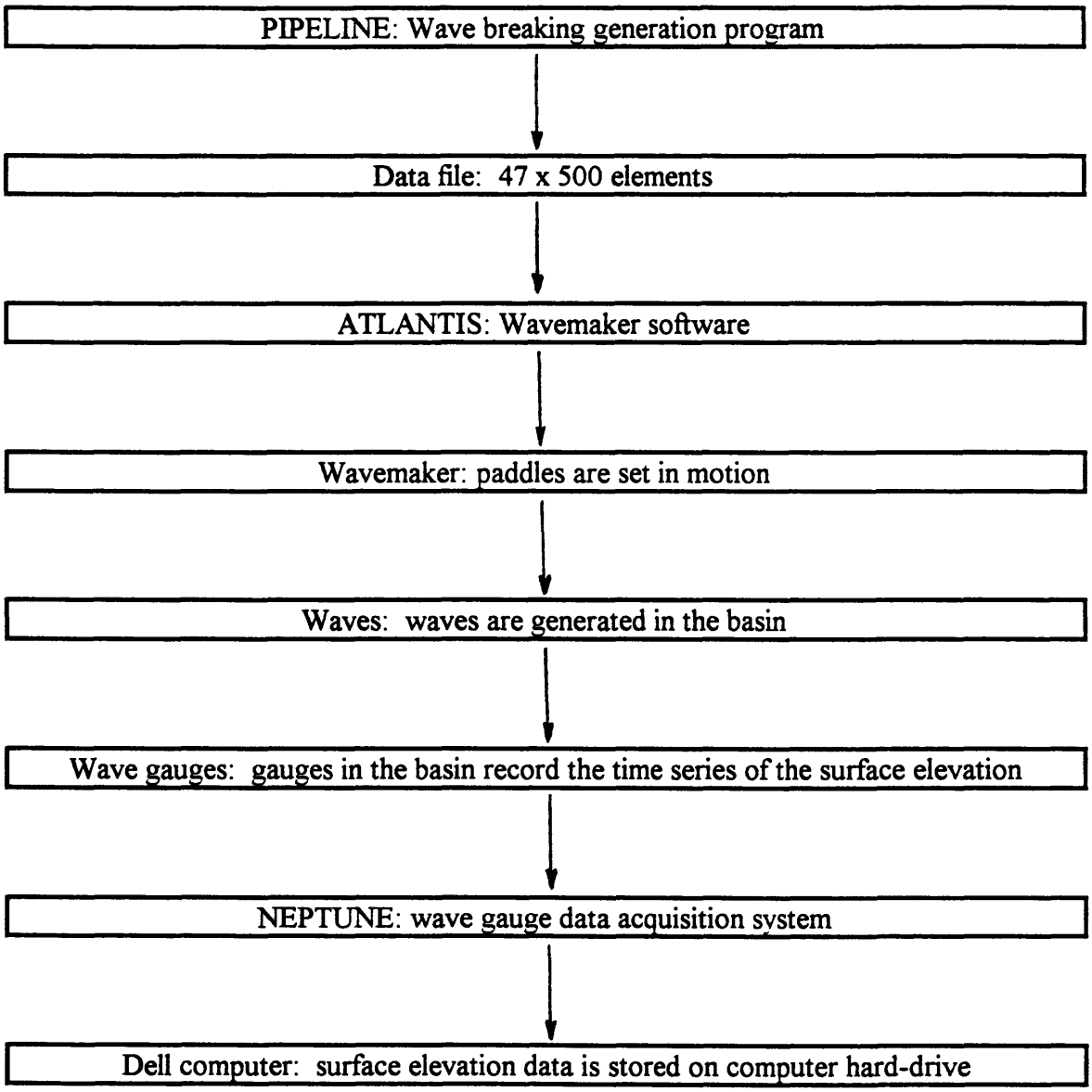

Figure 2.2 Integrated environment with the role of each individual component

Before running the experiment, the wave gauges require calibration. The first step is to set the offset of the amplifier to zero. Then, since the gauge readings are linear, the voltage at only two points, +/-10cm, needs to be calibrated using the gain of the amplifier. A 2cm / 1V ratio is used since the sampling card supports up to a +/-10V signal, and waves of about a maximum of 15cm amplitude are being generated. The gain on the amplifier has no electronic drift. However, the offset value of zero is susceptible to drift. The drift is minor, about 0.1V (i.e. 2mm), and the offset is constantly zeroed between runs. Moreover, as far as the spectral analysis is concerned, a small drift in the offset value has no effect since a spectrum has the mean value of the signal, which is typically zero, subtracted out. While running the experiments, the midpoint of each wave gauge is set at the mean water level. The data acquisition sample rate is 40Hz in order to capture the rapid variation of the breaker and to prevent aliasing from occurring.

A set of six wave gauges are aligned in the lateral direction starting at the centerline and extending towards the wall (figure 2.3). The coordinate system adopted is defined on this figure. The longitudinal direction is defined by the y-axis, the lateral by the x-axis, and the vertical by the z-axis. The origin is located midway between the channel walls, 180cm from the mean position of the paddles, and on the free surface The grid shown in figure 2.3, which defines the location where the surface elevation is recorded, has a spacing of 30cm in the lateral direction and 20cm in the longitudinal direction. The reason that the longitudinal direction has a higher resolution step size is because the variations occurring along the direction of wave propagation are more severe than those occurring across. A 50cm gap is left near the side walls. The maximum control volume to be scanned is 4m x 3m which requires 231 locations at which the free surface displacement is to be determined.

Since the wave gages span only one lateral section each time the wavemaker is run, they were slid in the longitudinal direction along the channel walls in order to scan the whole study area. This requires 21 runs of the wavemaker for each type of breaking wave. So, the wave packet generated by the paddles has to be tested for repeatability. A stationary seventh wave gauge is used to synchronize the different runs and to check the repeatability of the wave signal (figure 2.3). The wave packet is defined in figure 2.4.

Two independent runs of the wavemaker paddles are recorded by the reference wave gage (figure 2.5). The records are practically indistinguishable especially for the wave envelope which represents the time interval of interest in the signal (3sec to 13sec). The spectrum of the signal is also shown. The energy content of the wave packet for both runs is labeled on the figure in cm^2, and the comparison is exact, $20.9cm^2$ confirming the exact repeatability of the wave signal.

CONTROL VOLUME

* CONTROL VOLUME 4M X 3M
* X-MARKS DENOTE LOCATIONS OF WAVE GAUGES
* GRID SIZE OF 30CM X 20CM (231 LOCATIONS)
* PADDLE-CV DISTANCE = 3*DEPTH

ALL DIMENSIONS ARE IN METERS

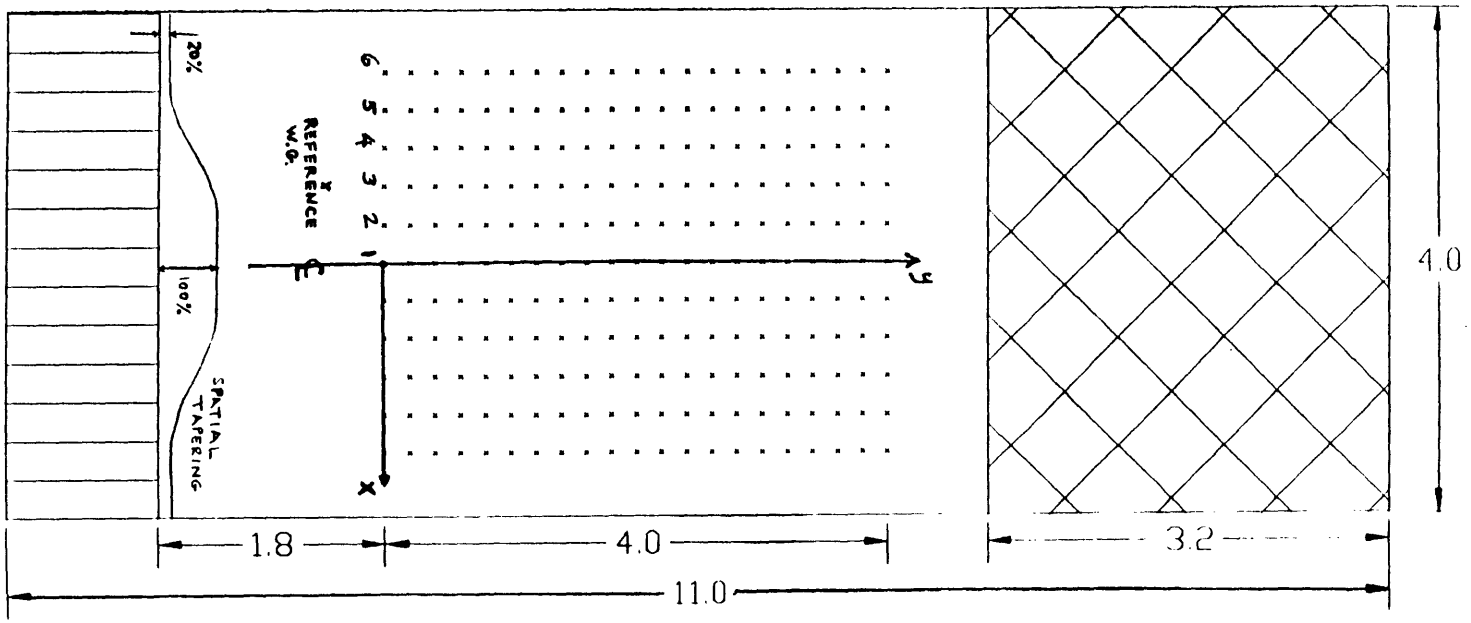

Figure 2.3 Top view of test section.

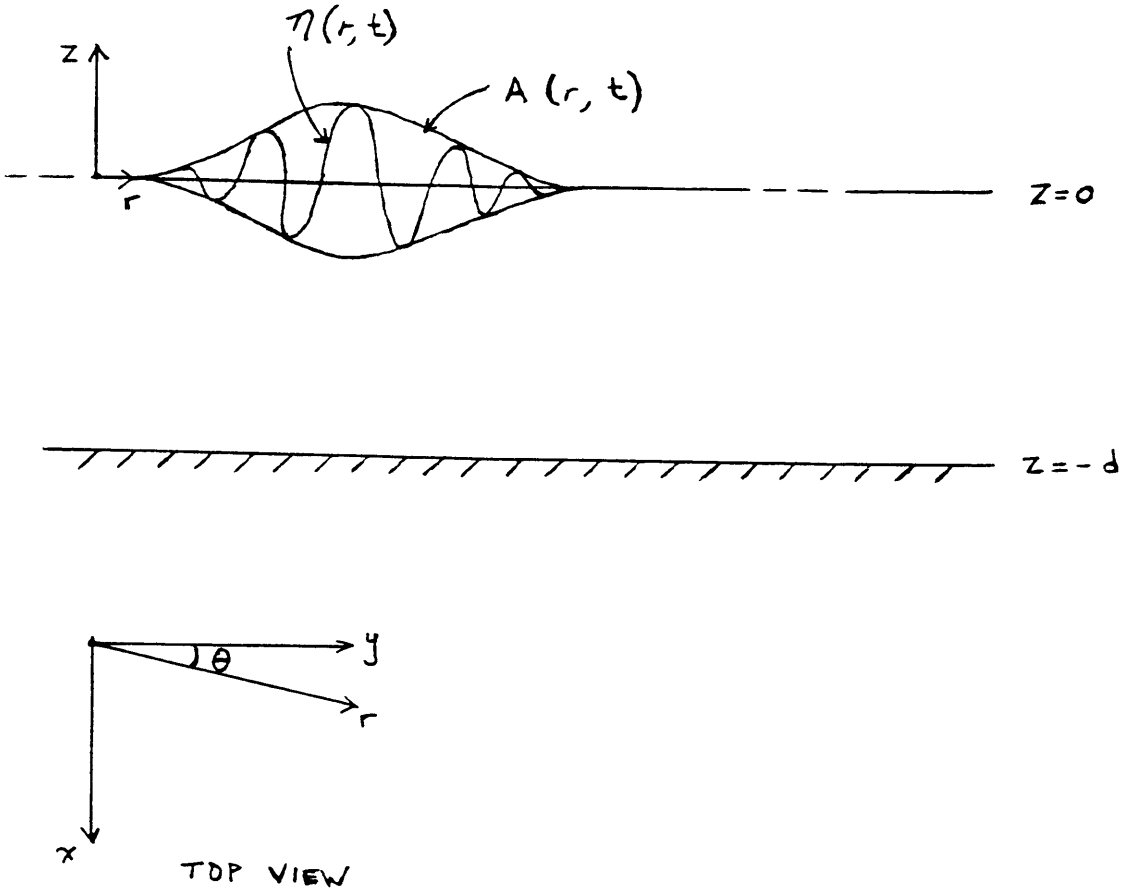

Figure 2.4 Wave packet definition.

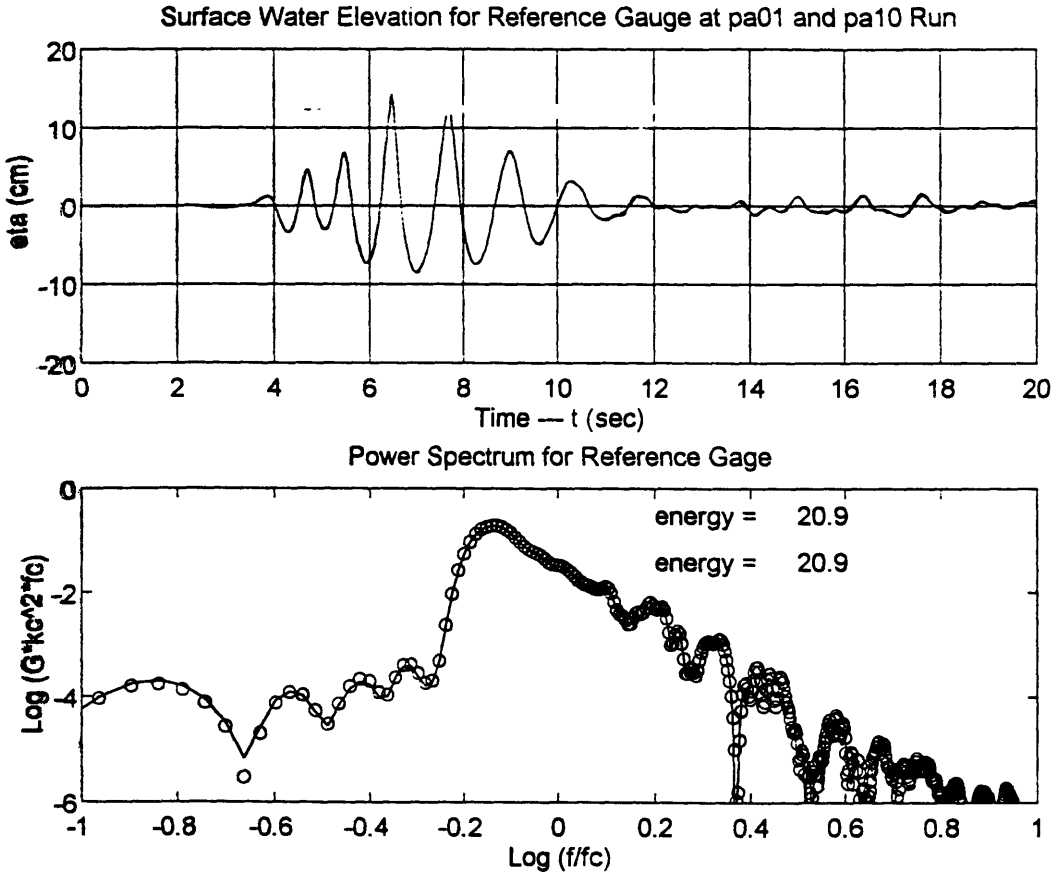

Figure 2.5 Repeatability of wavemaker.

The carriage system rests on 3 beams that stretch laterally over the whole 4m. The system rests on top of the channel walls, and hence nothing hangs in the water except for the series of wave gauges deployed (figure 2.6). The first array of wave gauges is positioned at 180cm (or y = 0), which is three times the depth, from the mean location of the paddles. This is done to let the evanescent modes decay to negligible values (Dean and Dalrymple, 1984). Moreover, a distance of about 75cm is left from the side close to beach since the recordings there are thought to be somewhat imprecise due to the presence of the beach itself. A more elaborate analysis on the effect of the walls and the beach will be discussed later on.

2.5 Generation of the Wave Packet

It is desired that a single breaking event occurs over the reach of the basin. The reason behind avoiding the issue of multiple breakers is to distinctly define the dynamics and evolution of an isolated breaking event without worrying about how, for instance, the turbulence of one breaker would affect the one downstream in the case where they are too close. Unsteady breaking waves are generated in the wave basin using frequency focusing. This technique, which was also used by RM, takes advantage of the fact that wave celerity is a function of frequency for deep water waves:

$$c = \frac{g}{2\pi} * \frac{1}{f}$$

where, c is the wave celerity in m/s, g is the gravitational constant = 9.81 m/s^2, and f is the wave frequency in Hz. This technique was first described by Longuet-Higgins (1974) who determined the variation in the paddle radian frequency, $d\omega/dt$, required to cause breaking at position y_b, i.e.

$$\frac{d\omega}{dt} = -\frac{g}{2y_b}$$

where y_b is the distance from the paddle mean motion taken to be zero for this section. This analysis is based on linear theory and therefore cannot account for nonlinear effects such as amplitude dispersion which occur near the point of breaking. Thirty two equally spaced frequencies are used to define the wave packet. The phase of each component is determined by superposing all components constructively at the breaking location, y_b.

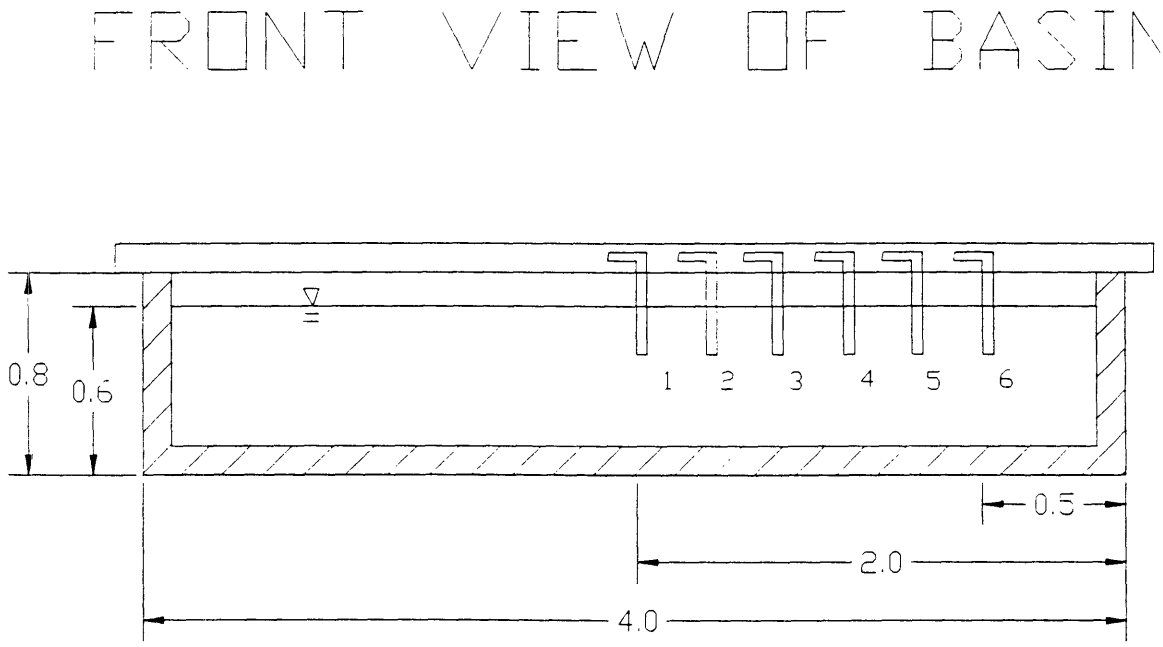

Figure 2.6 Front view of setup.

This enables the boundary condition at the paddles to be solved for and the input signal to be determined as described below.

The free surface displacement, $\eta(y,t)$, can be specified by

$$\eta(y,t) = \Sigma a_n \cos(k_n y - 2\pi f_n t - \phi_n) \qquad (2.1)$$

where a_n is the amplitude of the nth frequency component, k_n is the wavenumber, $2\pi f_n = \omega_n$ is the radian frequency, and ϕ_n is the phase. N is the number of components (equal to 32). k_n and f_n are related by the dispersion relation

$$(2\pi f_n)^2 = k_n g \tanh(k_n h) \qquad (2.2)$$

where h is the water depth.

The phase of each component is computed by setting

$$\cos(k_n y - 2\pi f_n t - \phi_n) = 1$$

at $y = y_b$ and $t = t_b$, the theoretical location and time of focusing.

$$\Rightarrow \quad \phi_n = k_n y_b - 2\pi f_n t_b + 2\pi m \quad (m = ...-2,-1,0,1,2,...)$$

The surface displacement specification becomes

$$\eta(y,t) = \Sigma a_n \cos[k_n(y-y_b) - 2\pi f_n(t-t_b)] \qquad (2.3)$$

For this derivation, the mean paddle position is defined to be $y = 0$, and the desired surface displacement at the paddle is then

$$\eta(0,t) = \Sigma a_n \cos[-k_n y_b - 2\pi f_n(t-t_b)] \qquad (2.4)$$

Variation in t_b will shift the entire signal in time with no change in the theoretical focal point, y_b. To reduce startup transients, the input signal to the paddles was tapered in time. This is done by applying a cosine window to both the start and finish of the signal.

The variables that completely specify $\eta(y,t)$ in equation (2.3) are

$N, a_n, f_n, k_n, y_b, t_b.$

Since f_n and k_n are related by the dispersion equation (2.2), k_n can be eliminated. But in doing so, the depth, h, and gravity, g, are added as independent parameters. The only slight modification done to the RM method for generating breakers is the definition of the individual wave amplitudes. For simplicity, they had taken

$$a_n = a_1 = a_2 = \ldots = a_N = \text{constant}$$

and define

$$a = a_n N.$$

However, further experiments conducted on breaking waves after 1986 show that more refined breaking packets can be generated by setting the individual wave steepness to be a constant (Eng Soon Chan, personal communication; Perlin 1995). This way premature breaking is avoided since all components scale similarly with regard to steepness.

$$a_n k_n = a_1 k_1 = a_2 k_2 = \ldots a_N k_N = \text{constant}$$

and hence the amplitude of the wave is defined as

$$a = \text{const} * \Sigma(1/k_n) \qquad (2.5)$$

The discrete frequencies f_n are uniformly spaced over the band

$$\Delta f = f_N - f_1 \qquad (2.6)$$

and the center frequency is defined as

$$f_c = 1/2 * (f_N + f_1) = 1.08\text{Hz (for the experiments described here)} \qquad (2.7)$$

The non-dimensional wave packet parameters then become

$$ak_c,\ \Delta f/f_c,\ y_b k_c,\ k_c h,\ N$$

where k_c is the wavenumber associated with the center frequency which is determined using

$$(2\pi f_c)^2 = k_c\, g \tanh(k_c h) \qquad (2.8)$$

The water depth at all times is h = 60cm. The resulting $k_c h$ term is 0.99 and hence the waves are effectively deep water waves. However, to be accurate, the k_n values are computed using the full dispersion relation.

N is made large (N = 32) to approximate a continuous spectrum, thereby eliminating the dependence of the form of the wave packet on N. Finally, the following functional relationship results:

$$\eta k_c = \eta k_c(yk_c,\ tf_c;\ ak_c,\ \Delta f/f_c,\ y_b k_c) \qquad (2.9)$$

And for the current study:

ak_c = 0.29, 0.32, 0.45, 0.42
$\Delta f/f_c = 0.73$
$y_b k_c = 28.4$

These three non-dimensional parameters are responsible for classifying the breaker.

Crest length and spatial tapering:

A parameter that defines the three-dimensionality of the breaker is the crest length, L_c. With the amount of space in the basin allotted to this project, the parameter L_c is a parameter that cannot be varied. L_c is set at three paddle widths or 90cm. Since the test section is comprised of thirteen paddles total, the remaining ten paddles are forced with an identical signal to those of the centerline but are attenuated. The spatial tapering of the paddles is done by applying a cosine window to the paddles that tapers down to a uniform value of 20% at the paddles closest to the walls. This is illustrated in figure 2.3. Hence, it is the wave focusing technique along with this spatial tapering of the paddle input signal that allows the generation of the three-dimensional breakers. For the fourth case, the two-

dimensional plunging breaker, has no spatial tapering for the paddles, and thus the wave packet is practically uniform across the 4m lateral section.

The "short-crestedness" of a wave, defined by the parameter Λ, is also used in the literature to define the three-dimensionality of wave fields (She, 1994). It is defined as the ratio of L1 to L2, which are representative length scales in the longitudinal and lateral directions respectively, as depicted in figure 2.7. The greater the value of Λ, the more short-crested a wave will be. A two-dimensional wave corresponds to a value of zero.

ak_c term:

This term represents the characteristic wave steepness of the wave packet. Again, a is the amplitude of the individual component corresponding to the central frequency, and k_c is the central wavenumber. This term is based on the theoretical input signal and not on actual experimental measurements done in the basin. The generation mechanism is designed so that all variables are held constant while the amplitude (gain) is increased. As the gain is increased, the wave group goes from the incipient stage to a spiller and finally to a plunger. Since k_c is held constant, the steepness, ak, increases with the gain. Varying the non-dimensional parameter ak_c effectively changes the wave height and consequently the momentum and energy flux in the wave packet. Therefore, a is a measure of the theoretical wave amplitude and is independent of the two non-dimensional parameters $y_b k_c$ and $\Delta f/f_c$. A more in-depth discussion on wave breaking and steepness criteria is presented in Chapter 4.

To generate isolated breakers in the basin, the input paddle signal is first set such that a very weak wave packet propagates down the basin without even being near the point of breaking. By simply increasing the gain of the input signal (i.e. amplifying the input signal), a spiller is observed to occur downstream at a point close to the theoretical breaking location y_b. This case is defined as the isolated spiller. It corresponds to an ak_c value of 0.32. The value of the gain slightly below that is the incipient case with an ak_c value of 0.29. Then, by further increasing the gain (and consequently ak_c), a second spiller is observed to occur somewhere about a wavelength upstream of the first. The periodicity in whitecaps being described here is also observed in breaking wave groups in the field (Donelan et al, 1972). Now the system is at an intermediate stage where two spillers are being generated in the basin in the same run. By increasing the gain further, the spiller occurring upstream builds into a plunger and the downstream spiller is reduced. To attain a single plunger, the gain must be increased until the plunging wave is vigorous enough that insufficient wave energy remains after plunging for a spiller to develop downstream. This is observed at an ak_c value of 0.45. A fourth wave case is run without

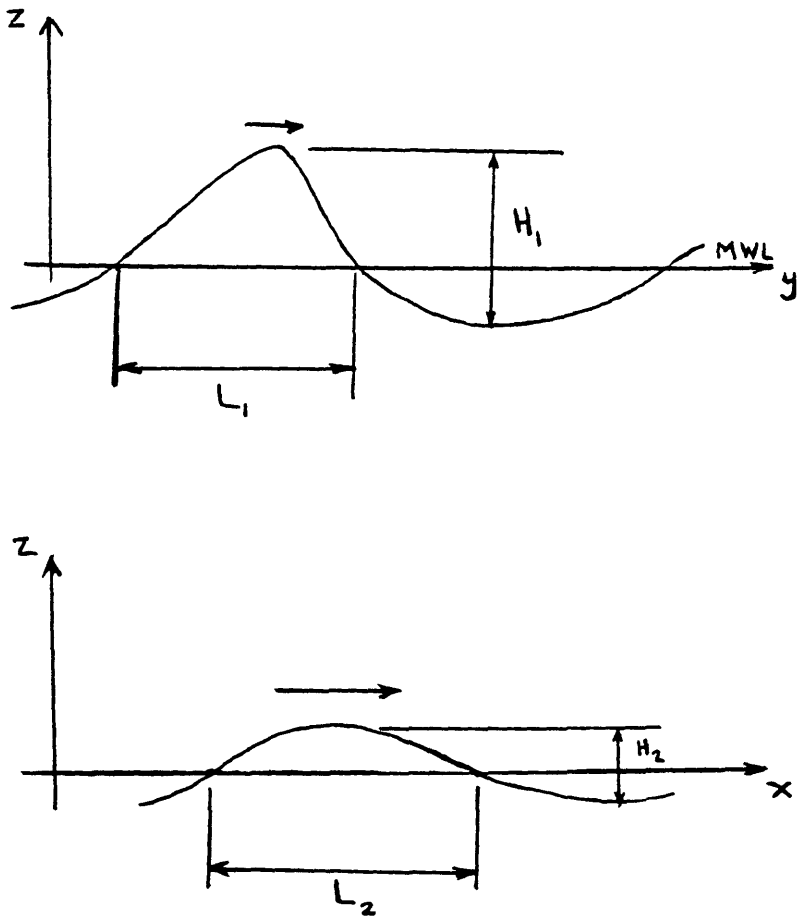

Figure 2.7 Crest length definition: $\Lambda = L1/L2$.

lateral tapering so that a quasi-2d plunger is produced. For this case, ak_c is 0.42. From here on, all references to the three-dimensional plunger will be termed 'plunger', whereas the two dimensional plunger will be noted as '2D plunger'.

$\Delta f/f_c$ and $y_b k_c$ terms:

Based on an extensive series of runs performed in the flume, RM have found that there is hardly any variation in the breaking characteristics if the non-dimensional bandwidth or non-dimensional breaking location values are varied (figures 3.3.4, 3.3.5, 3.4.2, 3.4.3, 3.4.5; Rapp, 1986). Actually , according to linear theory, changes in $y_b k_c$ should have no effect on the breaking dynamics, but only change location of breaking. This can be seen from equation (2.3) where the phase distribution is a function of (y_b-y) and not y_b alone. RM showed that the non-dimensional parameter ak_c is prominently responsible in defining the type of breaker that occurs. Hence, the values for $\Delta f/f_c$ and $y_b k_c$ are set as constants for all four cases.

The following values are used for all four packets: f_c = 1.08Hz, y_b = 6m, t_b = 11.5s. The corresponding non-dimensional values are: $\Delta f/f_c$ = 0.73 and $y_b k_c$ = 28.4. Only the non-dimensional parameter ak_c is different for all the four cases.

Transfer function:

Various tests done on the system by Susan Brown (personal communication) showed that the transfer function is independent of the number of paddles running or the particular set of paddles being run. The transfer function is:

$$|H| = -1.30\,f + 6.24$$

where,

f is the input frequency of the signal (Hz), and

$$|H| = \frac{\xi}{V_{input}}$$

where,

ξ is the dynamic displacement of the paddles (cm), and

V_{input} is the voltage inputted to the system (V).

The static equivalence of input voltage and paddle position is 10.24V = 2ft. The transfer function is used in determining the value of the amplitude, a, in the ak_c term.

Wavemaker equation:

For a piston type wavemaker, the equation that relates paddle stroke to the wave height of the generated wave (Dean and Dalrymple, 1984) is:

$$\frac{H}{S} = \frac{2(\cosh 2k_p h - 1)}{(\sinh 2k_p h + 2k_p h)} \qquad \text{piston motion}$$

This equation was used in the wave generation program. For deep water waves, it reduces to S = a. The fact that the stroke of the wave paddle is equivalent to the amplitude of the generated wave makes it intuitive that the input paddle signal seen in figure 2.8. will be quite similar to the wave packet forming in the basin at the wave paddles.

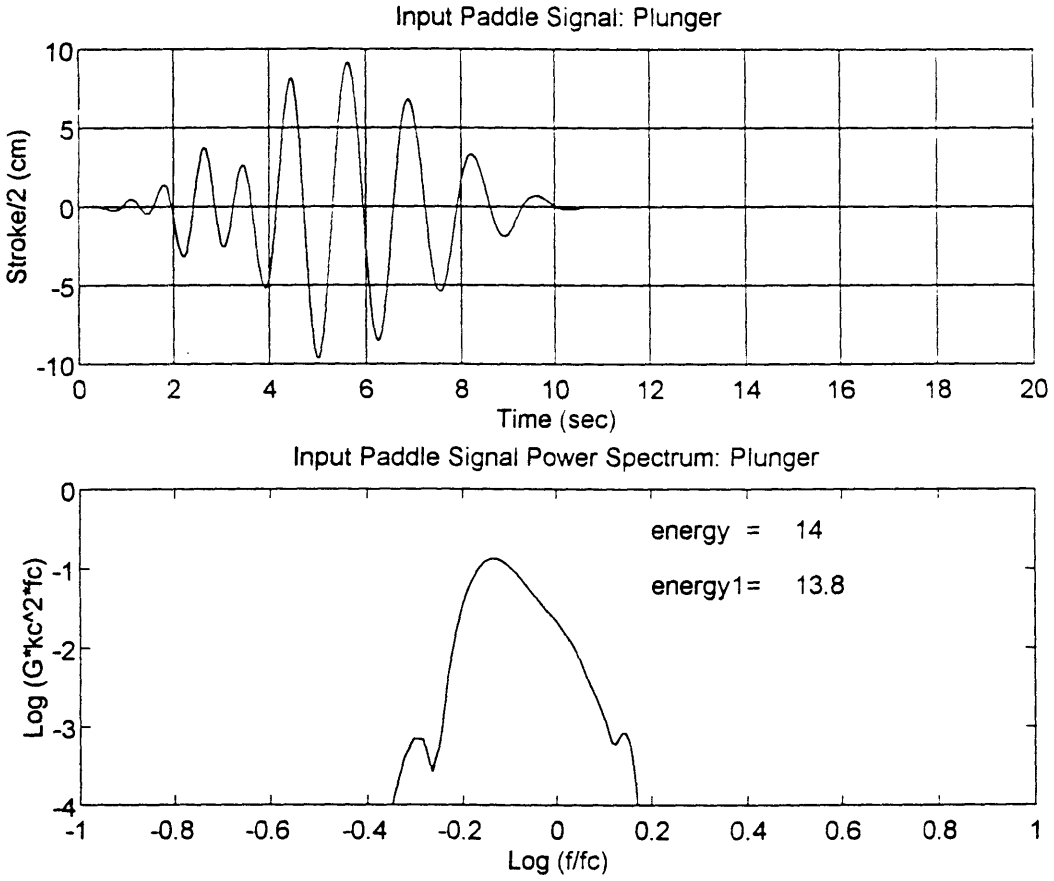

Figure 2.8 Input paddle signal (plunger).

CHAPTER 3

Surface Displacement of Breaking Wave Packets

3.1 Measurement of the Surface Displacement

As described in Chapter 2, a series of 6 wave gages are mounted on a carriage system (refer to figure 2.6). This array of wave gages then scrolls along a set of beams successively measuring the time series of the free surface displacement at different longitudinal positions.

The total size of the section in which measurements are taken is 4m x 3m as is shown in figure 2.3. A smaller control volume section will be defined later on based on the observed effects of the channel walls and the beach.

Since the wave packet is observed to be quite symmetric about its centerline, the number of locations at which the surface elevation has to be recorded will be reduced by half. However, to verify this symmetry, a few locations are also chosen in the other half of the basin. The recorded measurements of any two locations that are mirror images of each other with respect to the centerline match to within a few percent. This is true for the regions before and after breaking. Hence, it is fair to assume that the propagating wave packet is symmetric about its centerline, and consequently only one-half of the basin needs to be scanned with the wave gages.

A typical plot of the six series of wave gages is shown in figure 3.1. Again, the wave packet envelope is distinct from background oscillations. This particular plot is for the plunger case at the upstream location, y = 0 (180cm from the paddles). Obviously, wave gage 6 is the smallest of the six signals because of the spatial tapering. However, since the wave is three-dimensional in nature (i.e. it is not uniform along its crest), some energy will leak to the sides. This energy builds up along the walls because of the no-flux boundary condition, and some of it reflects back into the sampling region thereby contaminating the signal of the evolving breaker. The buildup along the walls can be observed at a station further downstream. For example, at y = 220cm (figure 3.2), the increase in wave energy at gauges 5 and 6 is due to the lateral propagation of wave energy from the centerline towards the wall. The analysis below will show how a control volume is chosen that excludes the effect of the walls.

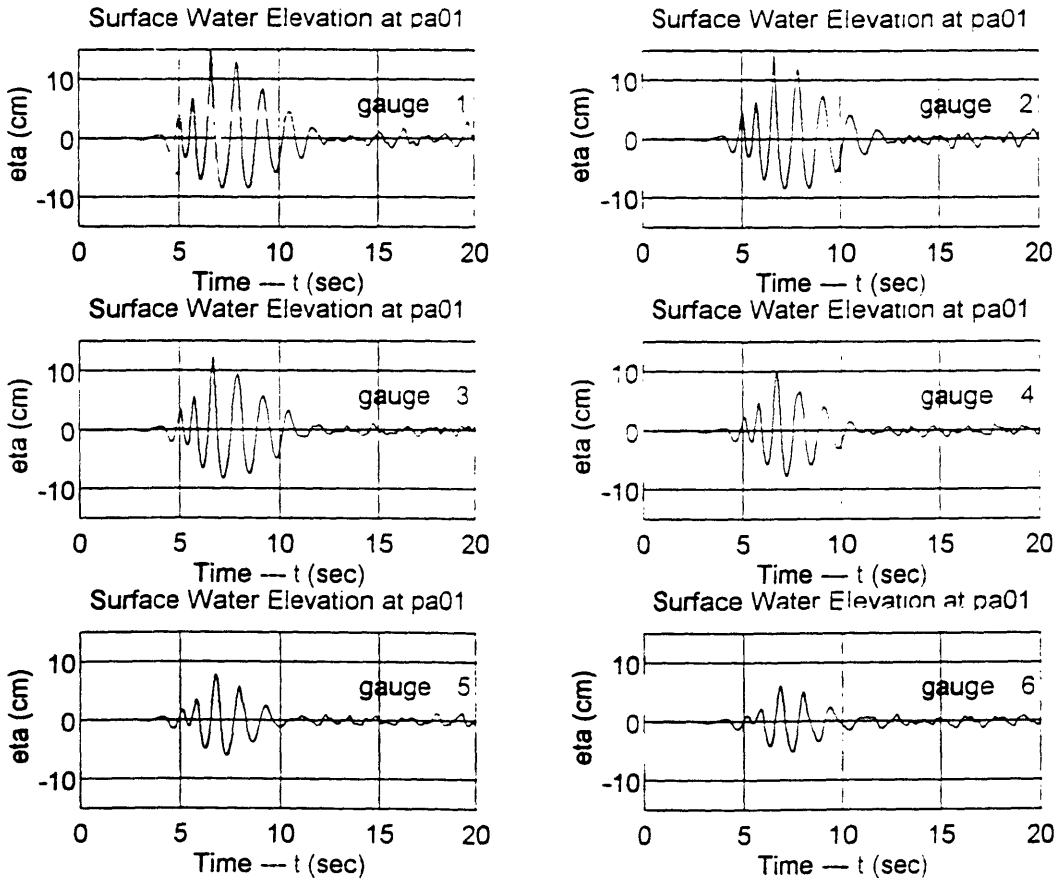

Figure 3.1 Time series $\eta(t)$ (plunger, $y = 0$).

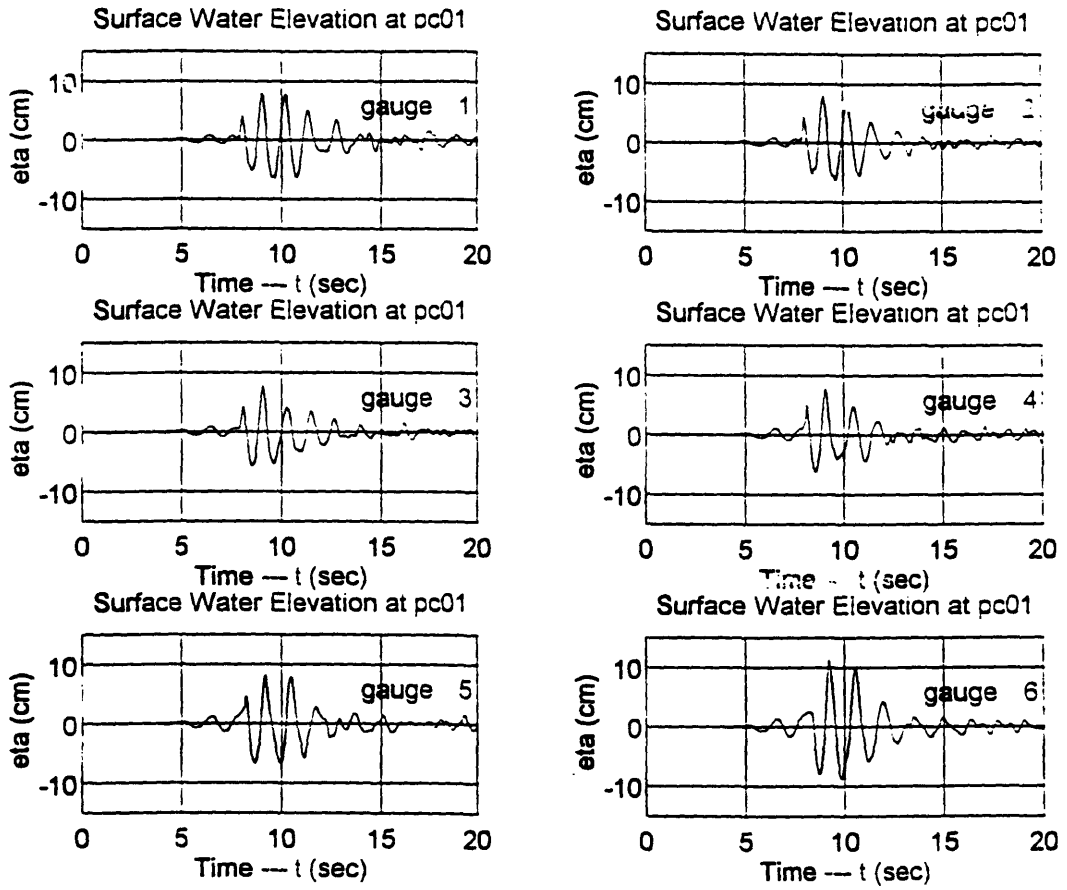

Figure 3.2 Time series η(t) showing energy buildup at the wall (plunger, y = 220cm). The time record for wave gauge 6 is larger than that of the centerline.

Reflections from the beach also interfere with the waves in the test section. The reflection coefficient of the beach with a slope of 1/6 is measured to be about 12%. The reflected waves heading back from the beach eventually contaminate the signal of the wave field being recorded by the wave gages.

The idea of generating higher frequency waves and thus scaling the project down is an option to consider. However, there is a physical limit on the ability of the wavemaker system to generate waves with too high a frequency. The wavemaker is capable of generating a 3Hz wave, yet for the duration and number of times in which the experiment is conducted, it is important not to push the system to its limits. Hence, the central frequency of 1.08Hz is implemented which runs quite well.

3.2 Spectra

3.2.1 Energy Associated with the Wave Packet

Surface displacement spectra are computed for the wave packet signal at each gauge. Specifically, a window is defined to include the wave packet and to exclude the reflected waves. Ten percent of the window is tapered at both ends by a cosine curve. The window length is 10sec, which includes 400 data samples, sampled at 40Hz frequency. Zero padding was done to produce a 2048 point FFT. The spectrum over the input band of frequencies is deterministic, so the spectral estimates do not have errors associated with stochastic processes.

Spectra computed from the wave signals shown in figure 3.1 are shown in figure 3.3. These are the associated spectra of figure 3.1. These plots represent the energy density versus frequency. The axes are both in log scale. This is done in order to magnify the difference in the energy estimates of the different harmonics. The frequency axis is normalized by the central frequency f_c, and the momentum flux density axis in cm^2/s is normalized by $k_c^2 f_c$. Included in Appendix 4 are all the spectral plots for both the plunger and incipient cases for the entire control volume. These figures will be referred to occasionally.

The area under a spectrum curve is a measure of the energy of the wave packet. (The energy is equivalently defined as half the sum of the square of the amplitudes of the individual components). In figure 3.3, the energy term labeled on the plot is the total area underneath the curve. The units are in cm^2. The term energy1 is the area below the first band of harmonics, 0.7Hz to 1.5Hz. This is the band of frequencies which comprise the

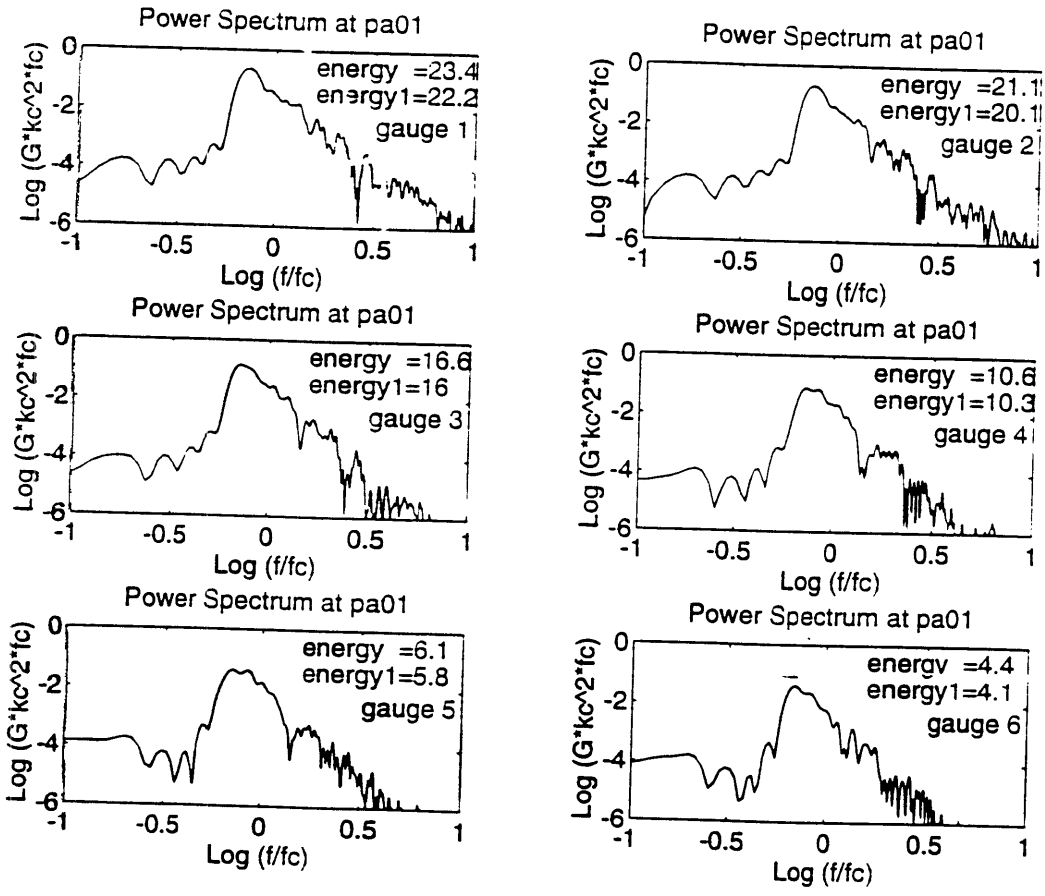

Figure 3.3 Spectra of figure 3.1 (plunger, y = 0).

input signal to the paddles. It is observed that for all the measurements, the energy in the first band of harmonics consisted of over 90% of the total energy of the packet.

The range of frequencies less than 0.7Hz have a negligible amount of energy, yet the evolution of the forced wave can be observed. The forced wave is a long wave that is associated with the startup motion of the wavemaker. In both sets of figures in Appendix 4, plunger and incipient, a growth in the forced wave is observed as the wave packet approaches breaking.

Before any of the experiments are run, the background noise is determined by sampling the water surface without any waves. The spectra computed for this condition are given in figure 3.4. The y-axis here is the log of the spectrum and the x-axis is the frequency. The total energy from these spectra indicate the level of background noise which is clearly negligible, as the computed energy is orders of magnitude lower than the energy recorded for the first or second harmonic bands. However, the severe spikes do reach magnitudes comparable to energy values of the third harmonic. This information will prove useful for the some of the discussion in section 3.3.3.

3.2.2 Control Volume

Since the energy of the wave packet is being radiated away from the centerline, the time series records and their spectra at regions near the wall are going to reflect the energy build up (see figure 3.2). Phrased in another way, for any two adjacent neighboring grid locations in the basin, one will expect a larger energy content at the location closer to the centerline if the walls were not there. Thus, a larger energy content at a location closer to the wall is indicative of energy build up at the wall. Hence, the effect of the walls can be easily determined by comparing the energy content of the wave packet at all neighboring points. The effect of the wall for the plunger case is determined in this manner in figure 3.5 with the effected regions marked with circles. These positions are excluded from the analysis since reflections from the wall contaminate the signal there. In future studies, the walled region will be expanded to decrease the importance of the wall location. A similar analysis is performed for the incipient case, and the effected regions again are marked with circles (figure 3.6). The wall effect is slightly more pronounced for the plunger case since it involves larger waves.

Reflected waves from the beach will also affect the wave packet signal. The area affected by beach reflections can be determined based on a group velocity analysis and is demarcated by a dashed line in figures 3.5 and 3.6. The group velocity is defined as c_g =

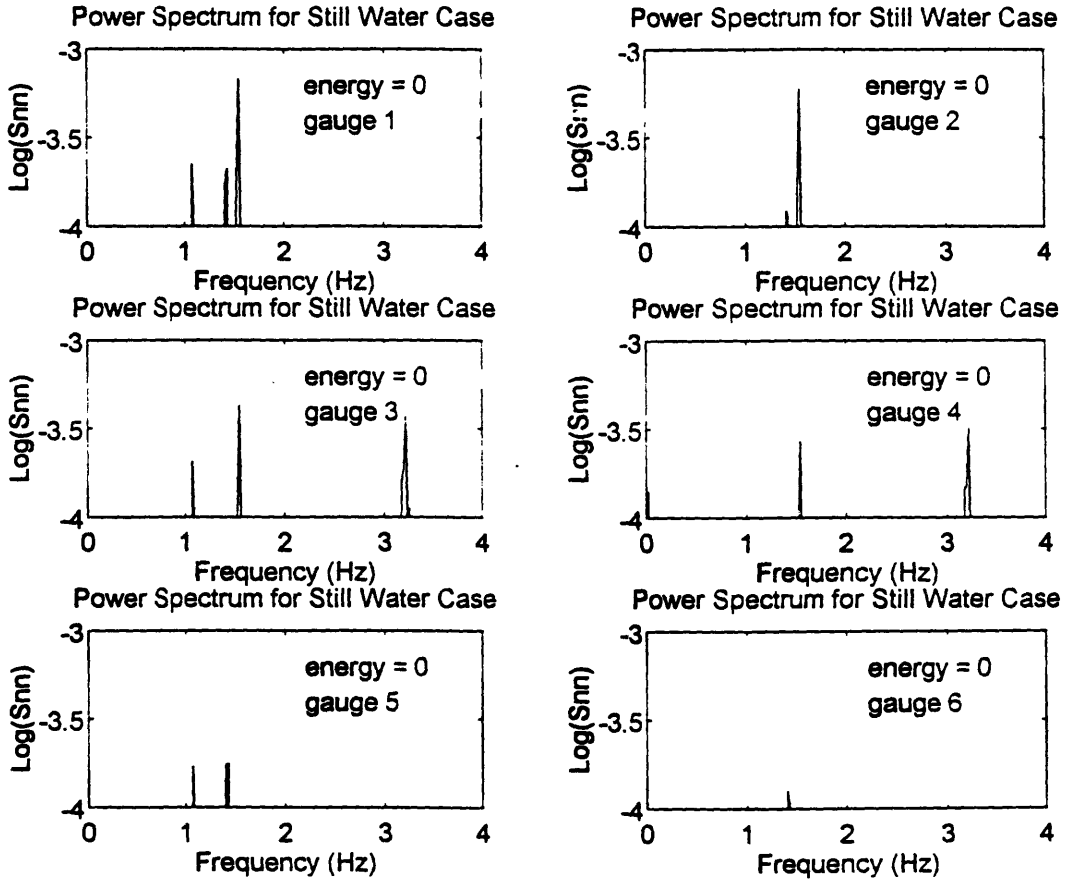

Figure 3.4 Spectrum of background noise.

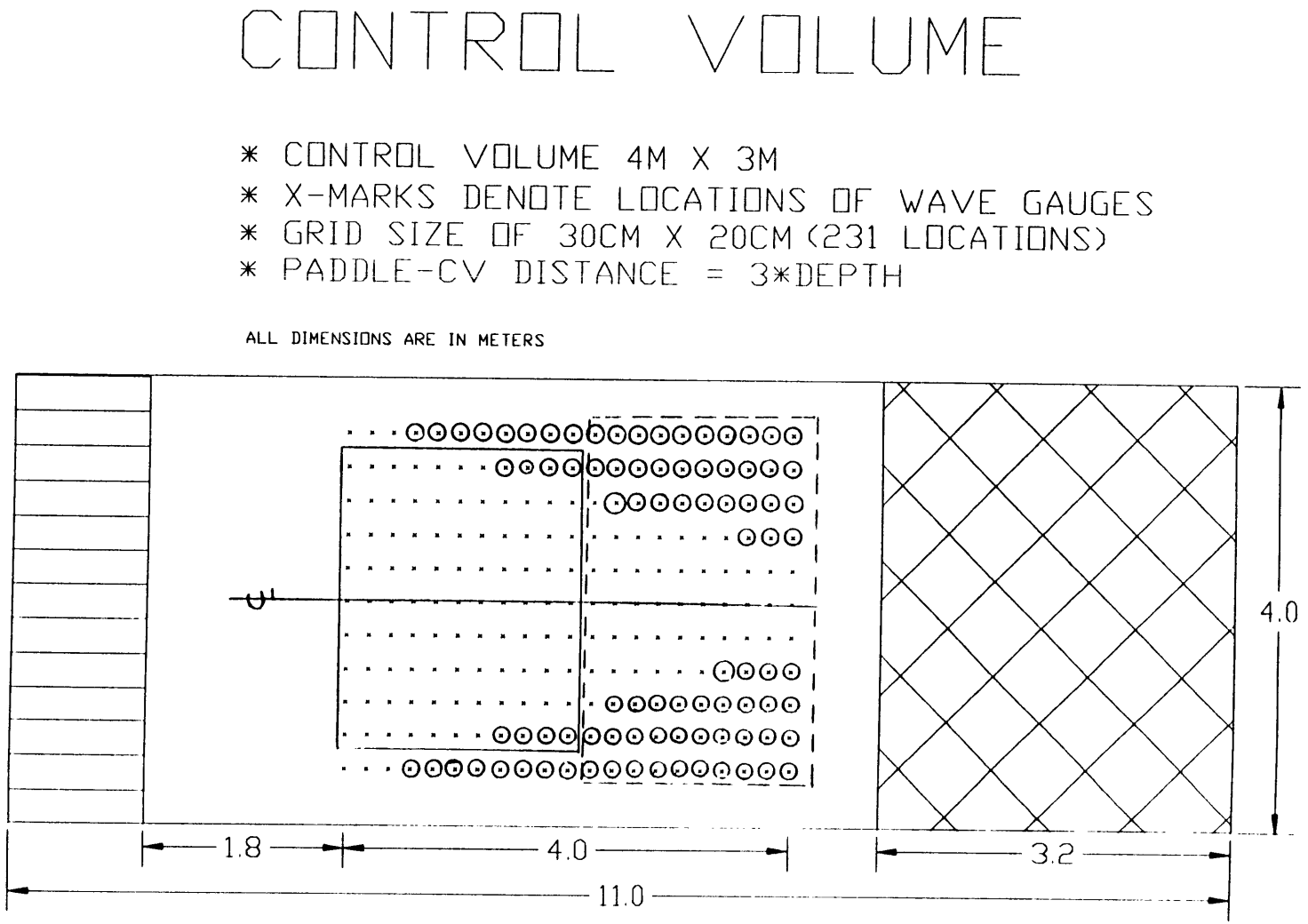

Figure 3.5 Control volume for the plunger (___). The reflection effects from the beach (---) and the walls (o) are marked. The defined control volume is practically outside the contaminated regions due to the reflection. The control volume is 2.0m x 2.8m.

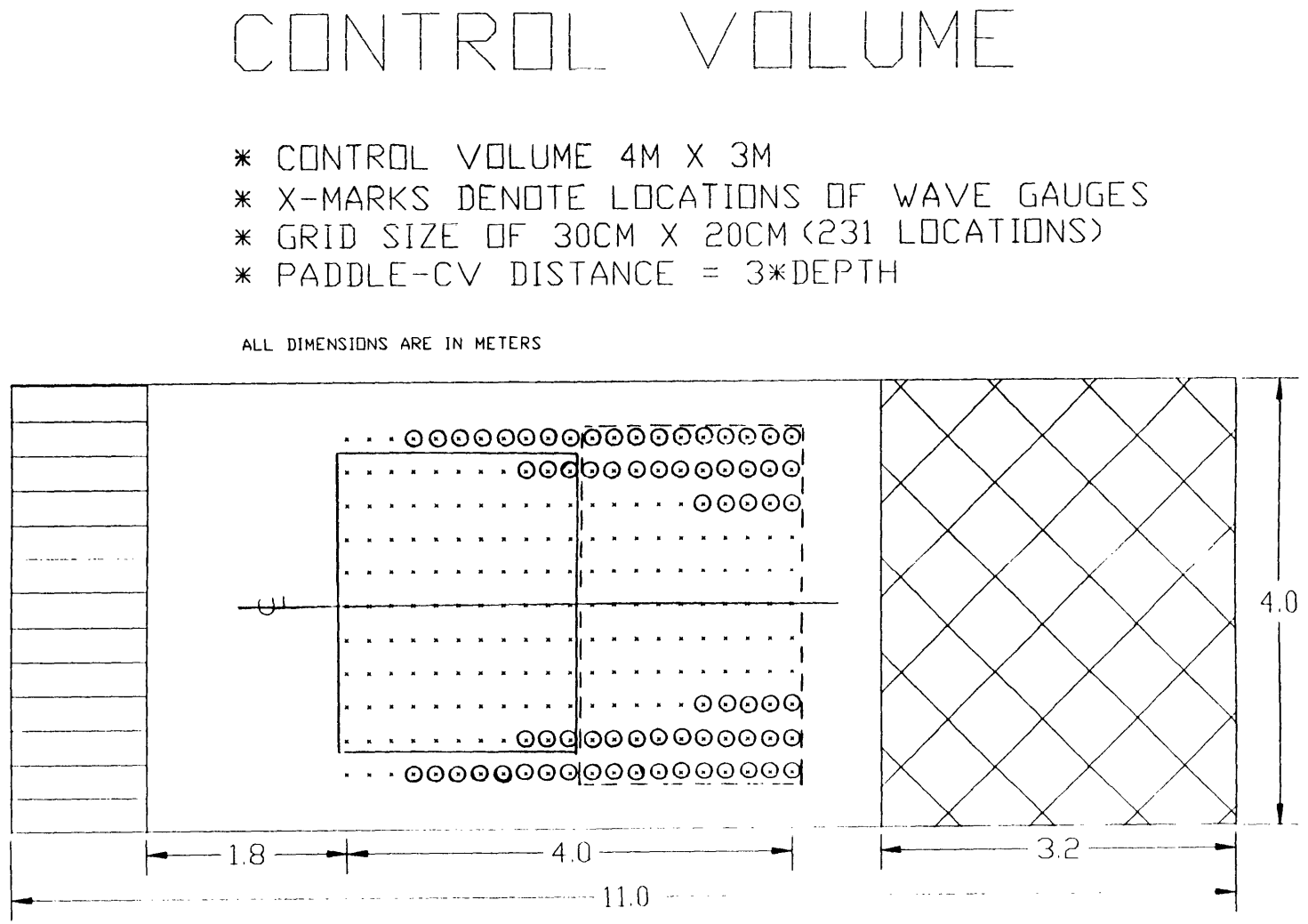

Figure 3.6 Control volume for the incipient (——). The reflection effects from the beach (---) and the walls (o) are marked The defined control volume is practically outside the contaminated regions due to the reflection. The control volume is 2.0m x 2.8m.

0.55 c_c. The reason the deep-water coefficient of 0.50 is modified to 0.55 is because the general dispersion relation is used. The group velocity is equal to 0.78m/sec. Since the reflected waves are of the same frequency as the incident wave components, the group velocity is the same. The region uncontaminated by the reflection from the beach is defined by locations where the wave packet has passed by and yet the reflected waves have not reached. This region is determined to be half of the scanned area. Including any of the demarcated regions of reflection will affect the computed energy values. The final control volume is defined so that both regions of reflection are excluded. This control volume is 2.0m x 2.8m. This region encompasses the plunging breaker only. The spiller, as is mentioned above, occurs further downstream.

Radiating waves have been observed to emanate in all directions from the breaking region following the breaking event (RM, 1990). These waves were reported to contain about 1% of the total energy of the packet. The analysis done by RM was based on regions in the flume in which the wave packet had passed by, but reflection from the beach had not arrived yet. In the case of the wave basin, the longitudinal fetch is not long enough to permit such analysis.

3.3 Energy Losses

There are three possible sinks of wave energy. Energy can be lost from the wave packet by the frictional dissipation produced at the side walls and the bottom. Secondly, energy can also be lost from the control volume by outward radiation of energy. Both of those events should be apparent in the incipient case. The third and most important loss is that due to breaking.

3.3.1 Viscous Dissipation

This loss of wave energy is due to the boundary layers at the wall and the bottom. In laboratory settings, the boundary layers are typically laminar. The equation for viscous dissipation for laminar boundary layers along with the energy loss calculations are given in Appendix 2. In a 4m wide channel and over a length of 4m, the energy loss amounts to 0.6% of the total input energy which is essentially negligible.

In the study done by RM, the total energy dissipated due to the boundary layers in their 0.78m wide flume over a fetch of 20m was about 10% (figure 3.2.1a; Rapp, 1986).

This matches well with the energy loss they observed in their incipient case. In analogy, we expect a similarly from the theory, and therefore we conclude that the loss due to boundary layers is negligible. The two remaining losses are those due to lateral leakage and to breaking.

3.3.2 Leakage

The wave packets being generated by the wavemaker are three-dimensional, i.e. the wave crests are not uniform across the basin. The lateral attenuation in amplitude causes some of the energy in the central region to radiate outward towards the sides. We decided to name this radiation of energy, which occurs for waves propagating bidirectionally, leakage. The incipient case along with the two-dimensional plunging case will be used to quantify the effect of leakage. Unlike the losses due to friction and breaking, leakage is actually a redistribution of energy and only appears as a loss relative to a stationary control volume. If the whole basin is considered, the net leakage losses are zero. Since the region of interest is a control volume smaller than the whole basin, the leakage must be explicitly accounted for. Here it is worth drawing the attention to the fact that experiments conducted in narrow flumes do not allow the breaking wave to evolve by radiating energy directionally outward, and thus are a step further removed from natural breaking events.

3.3.3 First and Second Band of Harmonics

We define the frequency range from 0.7Hz to 1.5Hz as the first band of harmonics because this is the range of frequencies contained within the input signal (i.e. the forcing). This is easily identified in all the spectral plots as the main cap in the center of the figures. Note how the constant wave steepness criterion is reflected in the shape of the right side of the main cap, i.e. the lower wavenumbers contain higher energy because the input amplitudes of these components are greater. In contrast, had a constant individual amplitude approach been adopted to generate the wave packet, the main cap would have had a constant value across the first band of frequencies. The second band of harmonics is identified as the smaller cap to the right of the first band. It ranges from 1.5Hz to 3.0Hz. These are shown in figure 3.7 which depicts the upstream location for the incipient case. Useful information cannot be extracted from the higher harmonics (i.e. third harmonic or

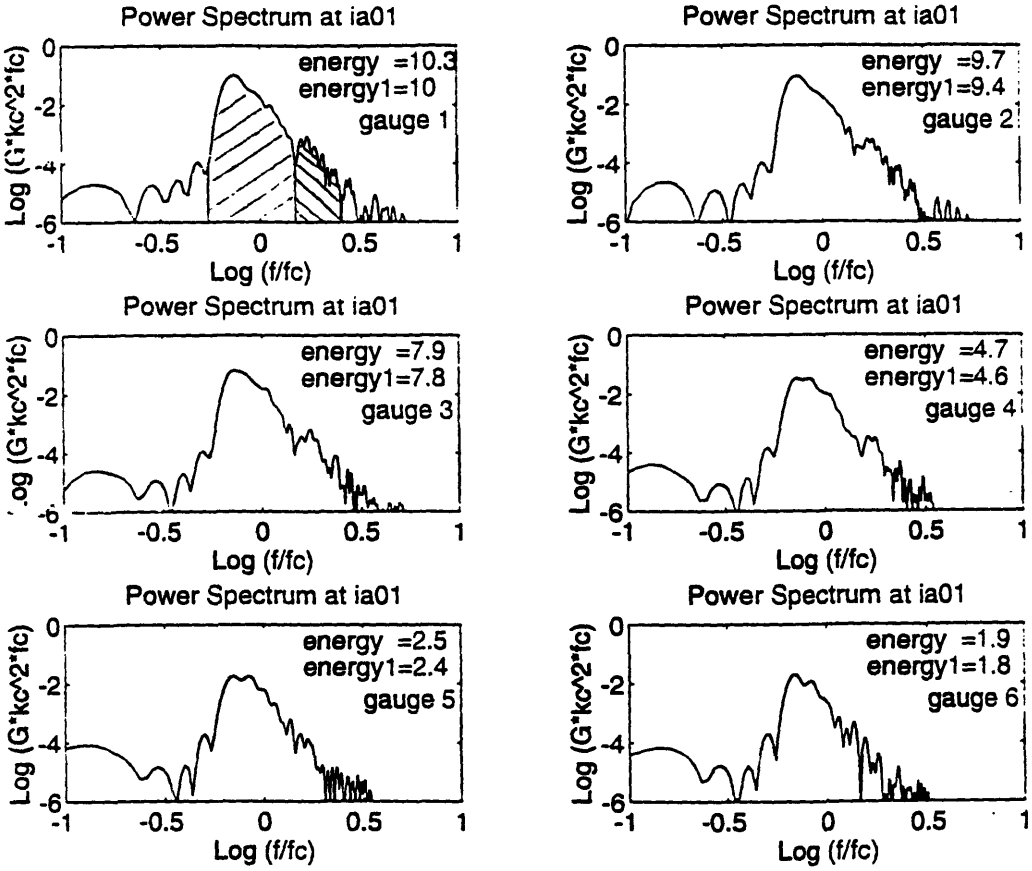

Figure 3.7 Spectra (incipient, y = 0). The energy value represents the total energy of the wave packet in cm^2. The energy1 term is the energy of the first harmonic band (input frequencies) and represents the main cap in the above figures.

higher) of the spectrum signal, because the energy estimates are nearing the resolution of the system (refer to section 3.2.1 and figure 3.4). From figure 3.7, the total energy is $10.3cm^2$. The energy associated with the first band of frequencies, energy1, is $10.0cm^2$. The energy for the second band, energy2, is $0.2cm^2$ which is two orders of magnitude less than that of the energy term. The third band of harmonics has an energy content of $0.01cm^2$, an order of magnitude less than that of energy2. Since the energy is proportional to the square of the amplitude, an energy3 value of $0.01cm^2$ roughly corresponds to an amplitude estimate of 0.1cm or 1mm. The wave gauge system is capable of sampling to within 1mm. However, when the waves being generated add up to over 10cm, the wave gauge recordings are not trusted beyond a 1mm resolution, and hence the energy estimates for higher bands of harmonics greater than the second meaningful.

3.3.4 Role of the Second Harmonic Band

For the incipient case, two focusing events are observed in the basin. The location of the first corresponds to that of the plunger, and the second to that of the spiller. To understand the roles of both the first and second bands, the energy values for each are calculated and the variations are plotted versus longitudinal distance. These are shown in figure 3.8 for the incipient case along the centerline. The term E/Eo on the y-axis is the ratio of the energy for a specified range of frequencies at a point downstream, y, to the corresponding energy value at the first upstream location, y = 0. The role of the first band, for the incipient case, is simply to describe the leakage losses as the packet progresses down the basin. However, there is an increase in energy in the second harmonic band as the wave packet focuses, and there is a decrease as the wave packet disperses. Hence, the second harmonic band indicates the approach to conditions of potential breaking activity. This signature is not detected in the first band.

For the plunger case, the breaker occurs upstream and then the wave packet disperses further on downstream in the region beyond the control volume. Similar to the incipient case, variations in the energy are computed (figure 3.9). Qualitatively, the first band describes the loss due to leakage and breaking, whereas the second depicts the buildup of the wave before it plunges and the sudden drop at the location where the plunger is observed. So again, the role of the second band harmonic is indicative of the breaking activity taking place. Typically, focusing events which entail shorter, higher frequency waves, will depict an increase in the higher harmonics, and a breaking event will

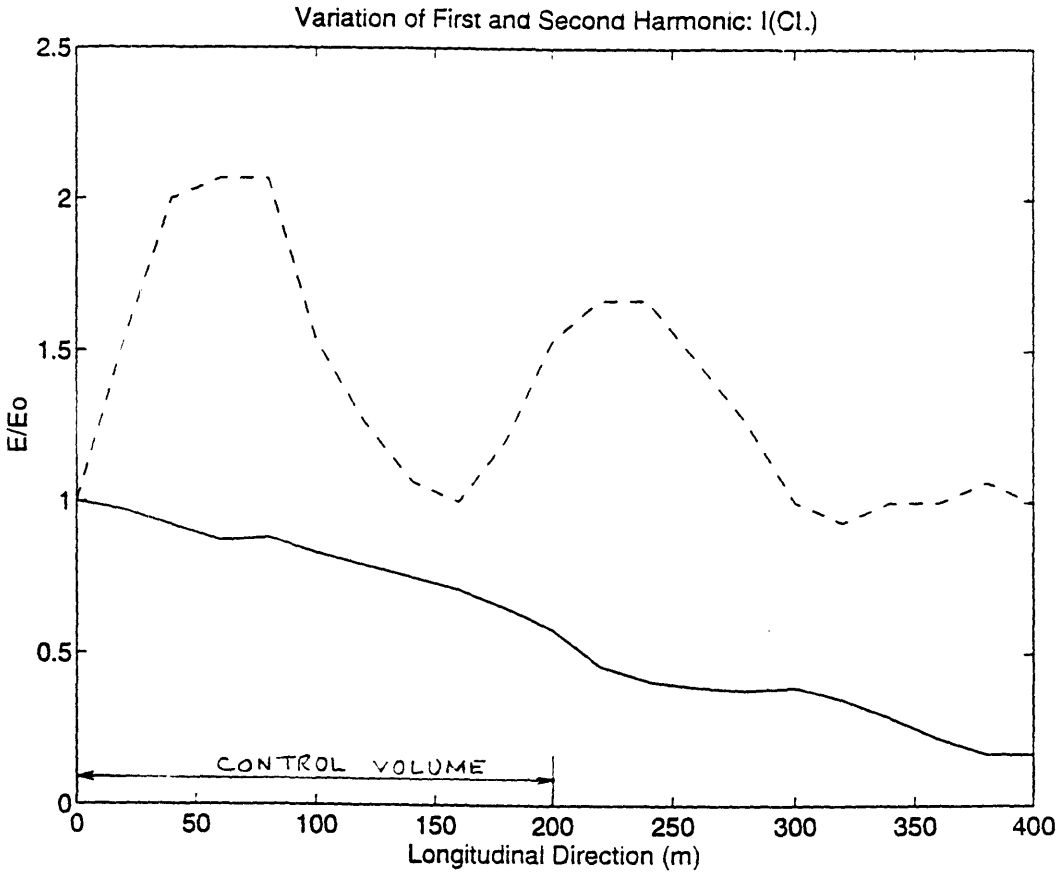

Figure 3.8 Longitudinal variation for the first (___) and second harmonic (---) bands (incipient, centerline x = 0).

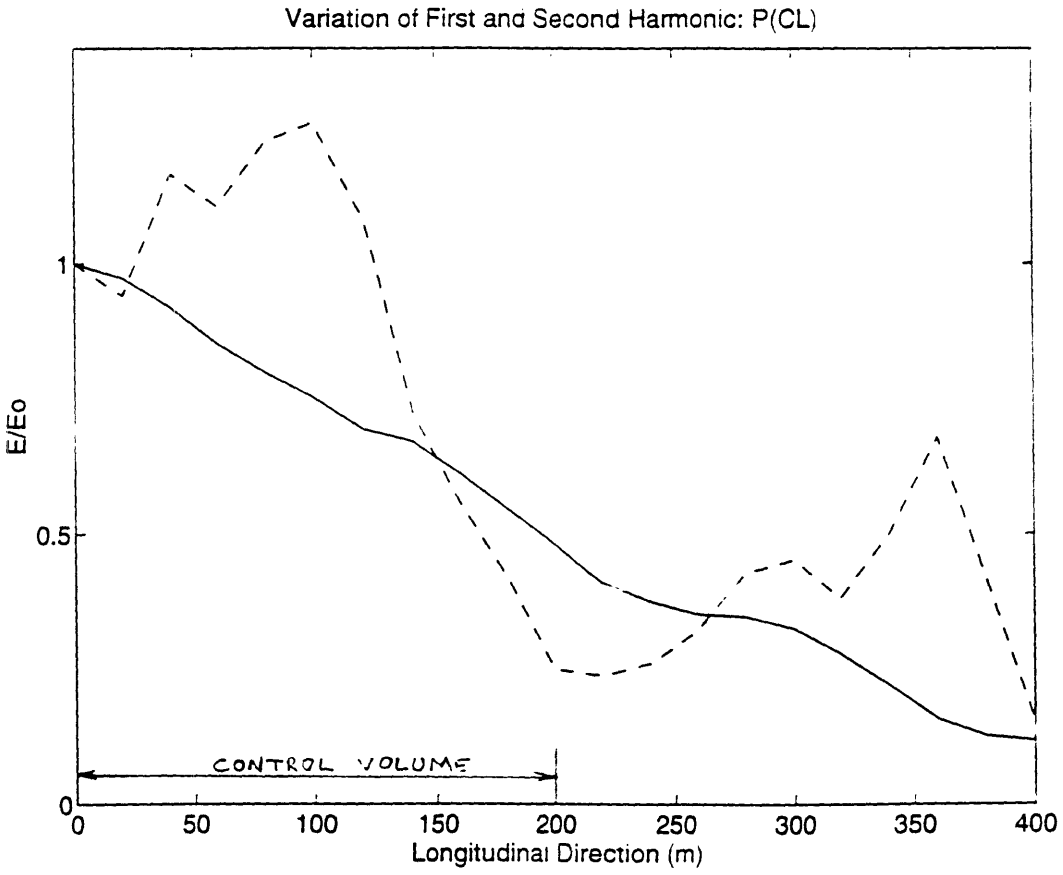

Figure 3.9 Longitudinal variation for the first (___) and second harmonic (---) bands (plunger, centerline x = 0).

describe the loss of energy from these higher harmonics. This is also observed by She (1994). Similarly, the spiller case for the centerline is shown in figure 3.10. Again, the incipient focusing upstream and the gentle spiller downstream are depicted by the behavior of the second harmonic.

3.4 Preliminary Energy Dissipation Estimates

3.4.1 Isolating the Leaked Energy and Obtaining the Energy Dissipation

Conceptually, the control volume is divided into several parallel channels. The aim is to quantify the dissipation within each channel and thus within the entire control volume. The starting point is to examine the two-dimensional plunger case, because the only form of energy loss that occurs in this case is that due to breaking. Figure 3.11 shows the variation of the energy in the first and second harmonic bands. There is a decrease of energy in the first band corresponding to breaking over the first 2m, followed by a constant value indicating that no further losses occur. Based on observation, we expect the breaking event to be associated with the higher frequencies of the packet. To take advantage of this, we define a critical value for the frequency, f_{cr}, below which the breaking activity has little effect on the spectrum. To see this, examine figure 3.12, in which the dashed line corresponds to the spectrum at the upstream end of the control volume and the solid line corresponds to the spectrum at the downstream end of the control volume after breaking has occurred. No losses occur besides breaking, and only the higher end of the frequencies suffer appreciable energy loss. Examining in particular the plot for wave gage 1, which is at the centerline, the wave energy loss is only observed above a value of $\log(f/f_c) = -0.125$ which corresponds to a value of $f = 0.81$Hz. Similarly for the remaining five wave gauges, by examining the frequencies at which the downstream spectrum deviates from the upstream one in figure 3.12, these frequencies are comparable to $f = 0.81$Hz. Hence, for the plunger case, the loss due to breaking is confined to frequency values larger than $f_{cr} = 0.81$Hz. Since the breaking activity is associated with variations in the energy content of the higher frequencies, it would be anticipated that the value for the critical frequency, f_{cr}, be close to the frequency, f_e, that equipartitions the total energy of the spectrum into two equal halves. The peak of the spectrum occurs typically at $f_p = 0.78$Hz, and $f_e = 0.86$Hz. Hence, this critical frequency occurs in between f_p and f_e. Based on the above definitions, the frequency range from 0.7Hz to 0.81Hz will be labeled as the "left" side of the spectrum and the range from

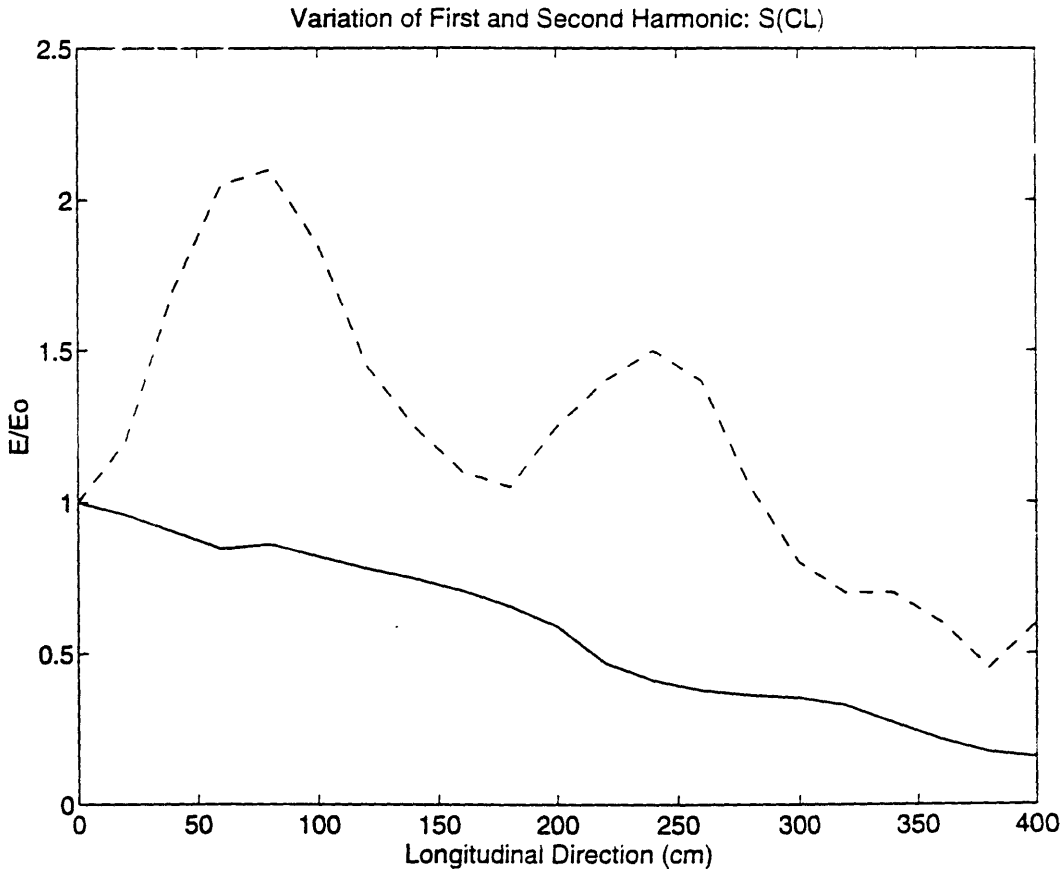

Figure 3.10 Longitudinal variation for the first (___) and second harmonic (---) bands (spiller, centerline x = 0).

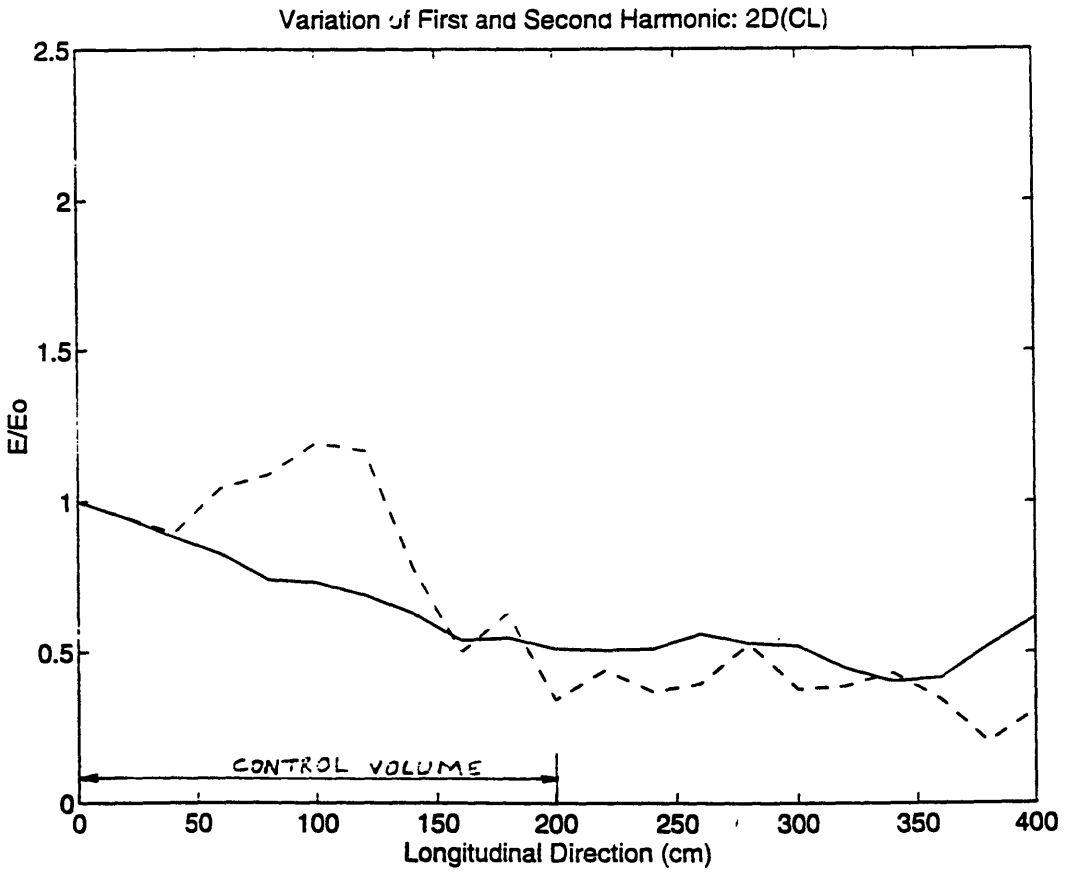

Figure 3.11 Longitudinal variation for the first (___) and second harmonic (---) bands (2D plunger, centerline x = 0).

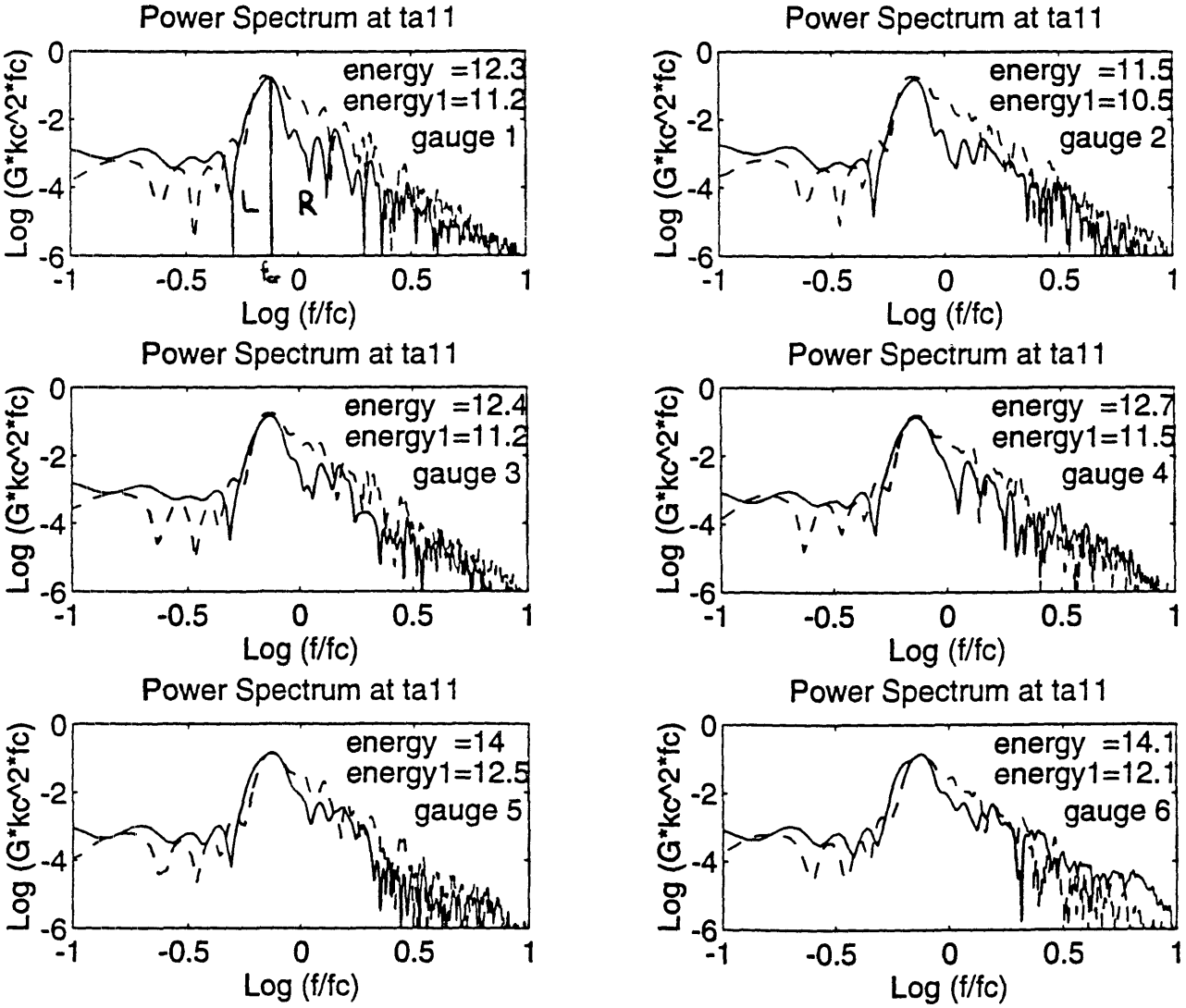

Figure 3.12 Spectra (2D plunger, y = 200cm). Wave gauge 1 was used to define the critical frequency, f_{cr}, which was used in segregating the breaking and leakage effects. The value occurs at $\log(f/f_c) = -0.125 \Rightarrow f_{cr} = 0.81$Hz. Upstream spectra (---), downstream spectra (___).

0.81Hz to 3.0Hz as the "right" side of the spectrum. The energy contained in the left and right sides of the spectrum is about 99% of the total energy of the spectrum. It will be useful to keep in mind that the f_{cr} value is close to that of f_e so that the percentage losses computed for the right side of the spectrum will be about twice those for the total energy:

(% loss in right side of spectrum) $\cong 2 *$ (% loss of total energy)

So, it is apparent in the 2D plunger case that any losses of energy in the spectrum from values below the critical frequency value of 0.81Hz are solely due to leakage. Examining the same spectral evolution for the incipient case (figure 3.13), we see that although the leakage is predominantly expressed at the low end of the spectrum, some leakage losses also occur from the high end of the spectrum. This implies that for the plunger case, the frequencies above the critical value of 0.81Hz depict losses that occur both due to leakage and due to breaking.

The next step in the analysis is to plot the energy variations to the left of f_{cr} and to the right of f_{cr} for both the incipient case and the plunger case. For instance, the plot for the centerline is shown in figure 3.14. Since the leakage is proportional to the square of the amplitude, the same percentage of wave energy loss for both the incipient and plunger results for $f < f_{cr}$. However, for $f > f_{cr}$, the energy loss in the spectrum in the incipient and plunging cases do not match and the difference is due to breaking losses. Thus, the difference between the two lines at the downstream end of the control volume represents the fractional loss of energy due to breaking alone.

The percentage energy loss E/Eo in the right side of the spectrum due to breaking alone is 20%. This corresponds to a fractional loss of 11% of the total energy as is described by the above equation. Similar plots are shown for wave gage 2 and wave gage 3 which in turn reveal dissipation estimates of 11% and 10% respectively of the total energy (figures 3.15 and 3.16). These three regions represent the breaking crest which is 1m in the lateral direction. It is expected that the dissipation estimate close to the wall is practically zero since no breaking occurs there.

Since the energy dissipation estimates are being obtained from the potential energy (wave gage) measurements, a similar analysis cannot be made in regions in which reflection, especially from the wall, has an effect on the recorded wave gage signal. Hence, in terms of describing the dissipation in the lateral direction, the three estimates obtained above are all that can be extracted from the data collected in the experiment.

A similar analysis is attempted for the spilling breaker although the location of the spiller is in a region contaminated by reflection from the beach. Based on observation, the

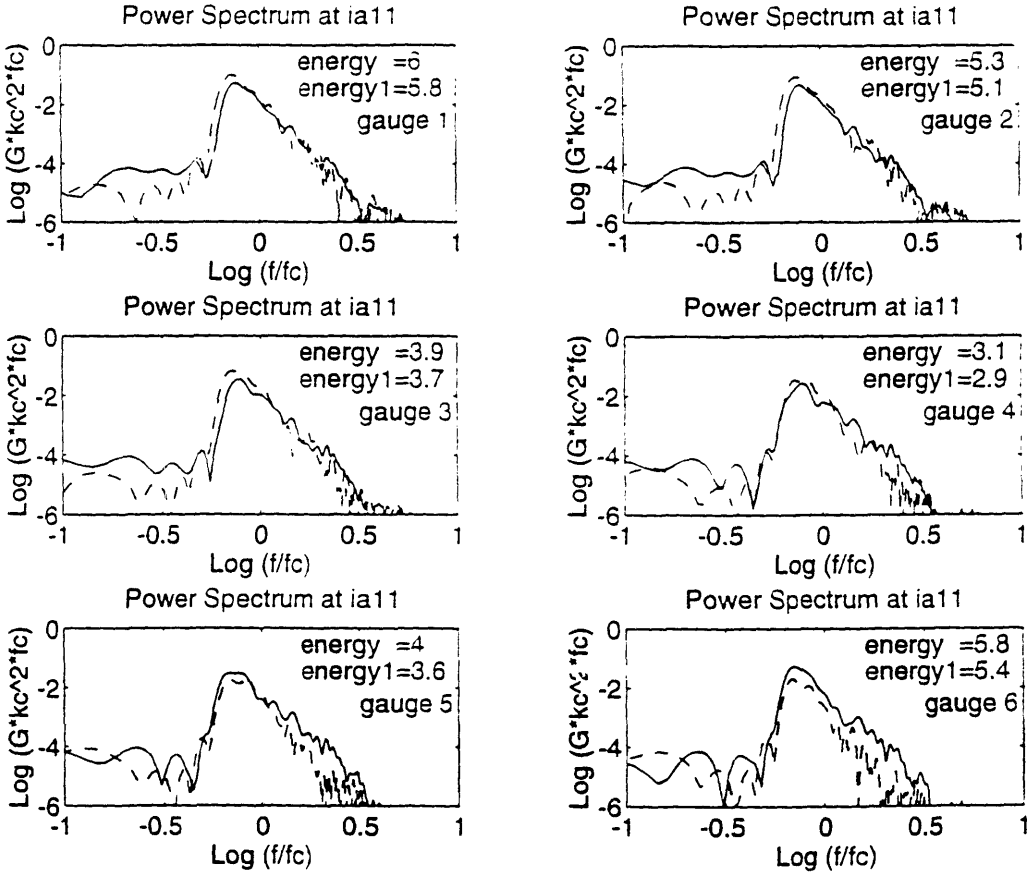

Figure 3.13 Spectra showing leakage (incipient, y = 200cm). Upstream spectra (---), downstream spectra (——).

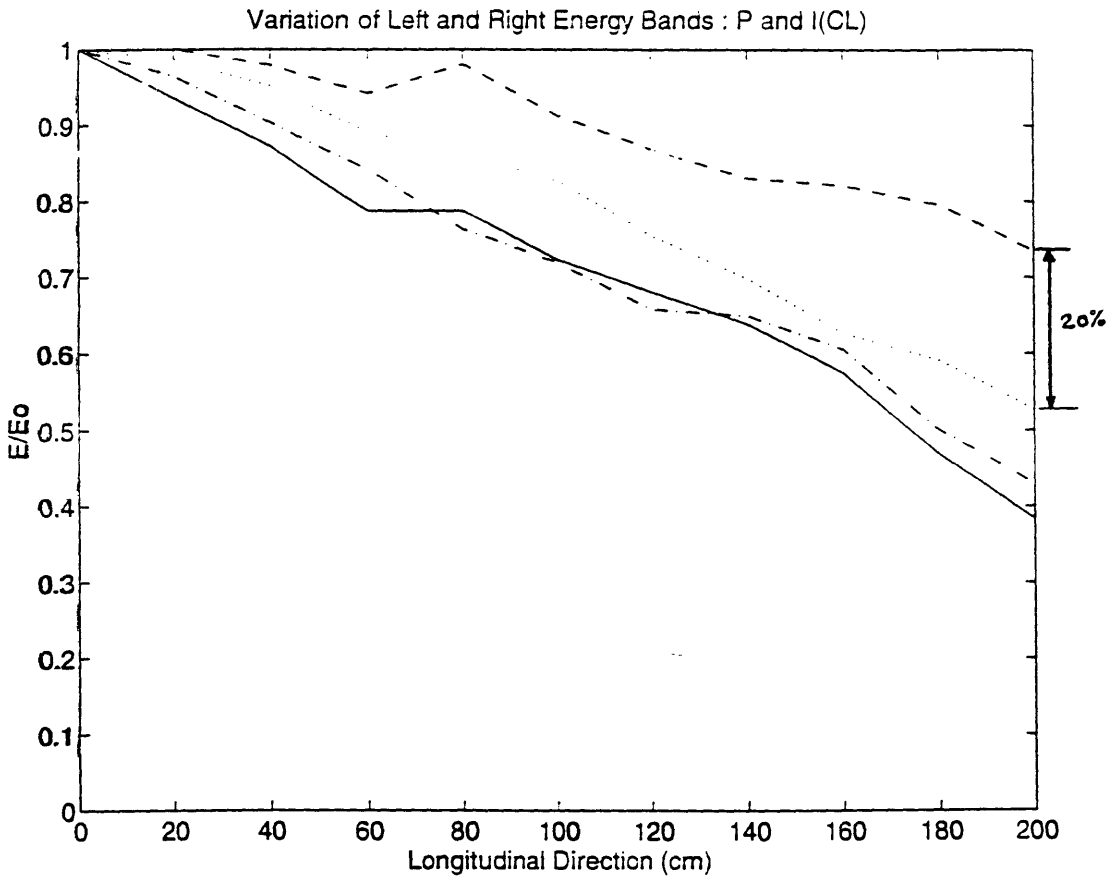

Figure 3.14 Wave energy dissipation due to breaking (plunger, centerline x = 0).
Incipient left (——), plunger left (-·-·-·), incipient right (---), plunger right (···).

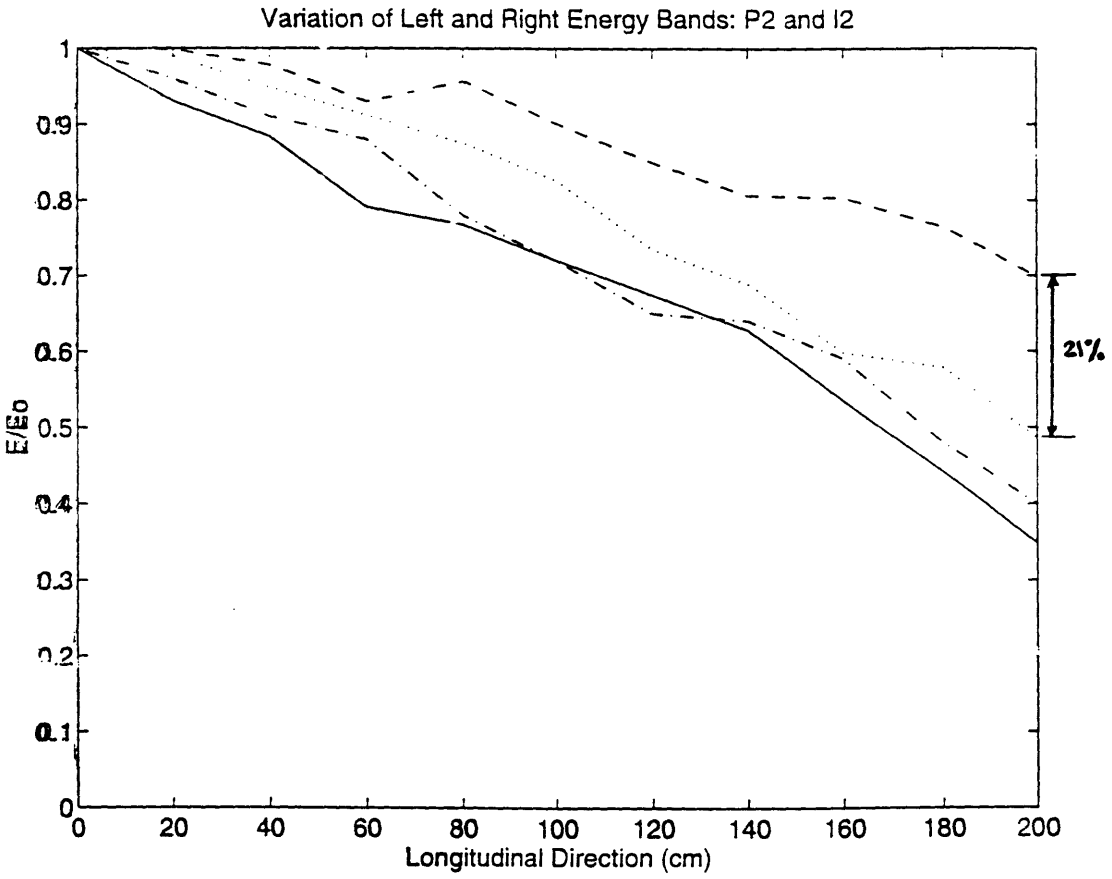

Figure 3.15 Wave energy dissipation due to breaking (plunger, x = -30cm). Incipient left (——), plunger left (-·-·-·), incipient right (---), plunger right (···).

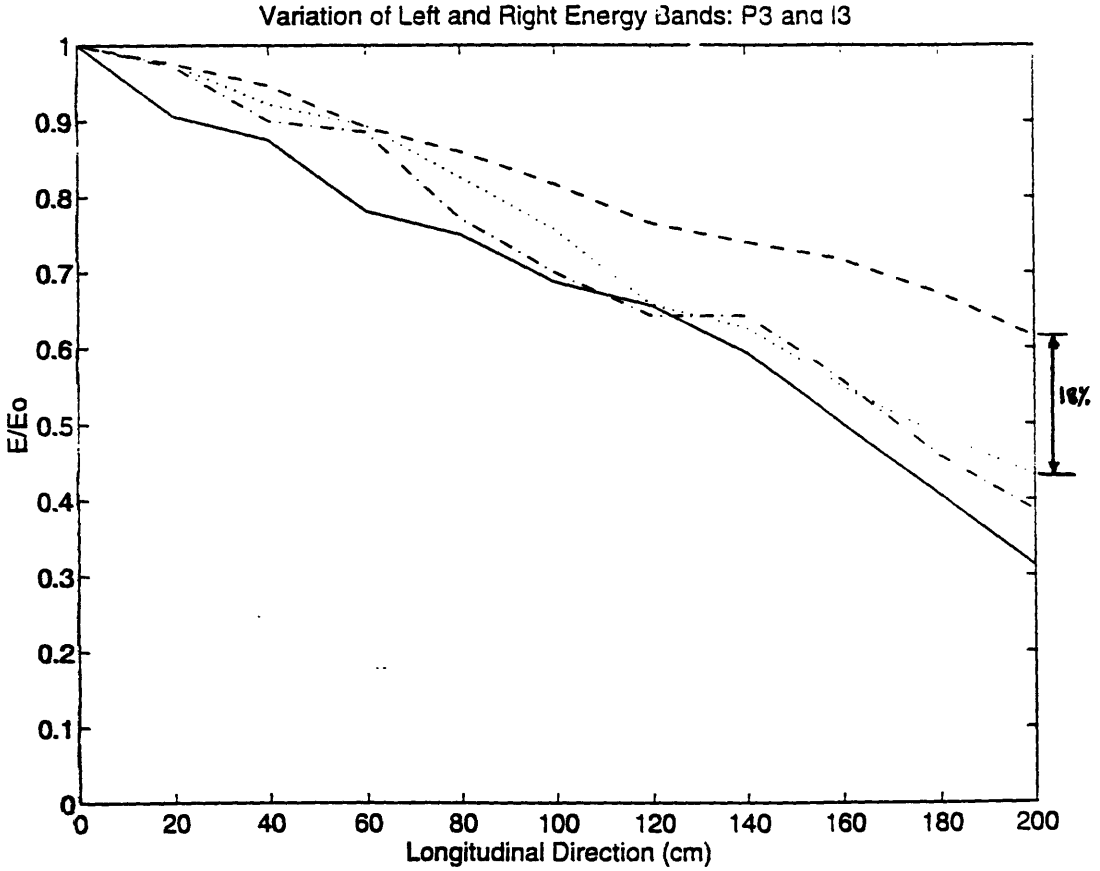

Figure 3.16 Wave energy dissipation due to breaking (plunger, x = -60cm). Incipient left (——), plunger left (-·-·-), incipient right (---), plunger right (···).

location y = 300cm is a representative location for computing the wave energy loss. Reasonable dissipation estimates are obtained and are shown in figures 3.17, 3.18, and 3.19. The wave energy loss at each of the three locations is 3%. This is likely an underestimation due to beach reflection effects.

3.4.2 Confirmation of the Obtained Energy Dissipation Values

The above approach to determine the energy dissipation estimates due to breaking involves dissecting the total losses into both leakage and breaking effects. A closer examination of this procedure reveals that the implicit assumption made is that the fractional loss of energy in the incipient case is the same as that for the plunger case for losses associated with leakage only. This being said, an easier approach can be adopted that is equivalent to the first. The idea is to plot the variation of the *total* energy (practically the sum of the energy in the first and second harmonic bands) for both the plunger and incipient on the same plot and to observe the fractional difference between the two lines at the end of the control volume. The cases for the centerline, wave gage 2, and wave gage 3 are shown in figures 3.20, 3.21, and 3.22. The respective values for the breaking dissipation estimates are 12%, 12% and 10%, and are identical (since the math is identical) to the lateral variation in the dissipation estimates obtained above within our control volume .

A similar check is done for the gentle spiller. Figures 3.23, 3.24, and 3.25 show a consistent wave energy loss of 4% which matches quite well with the 3% value observed in the previous section.

A table to summarize the above results is presented for only the three central channels. Half the basin is comprised of 7 channels. The remaining 4 out of the 7 channels have been affected by the presence of the wall. However, section 4.5 provides a more complete analysis of the 7 channels.

Table 3.1 Wave Energy Dissipation Estimate due to Breaking

Breaker Type	Channel 1	Channel 2	Channel 3
Plunger	12%	12%	10%
Spiller	4%	4%	4%

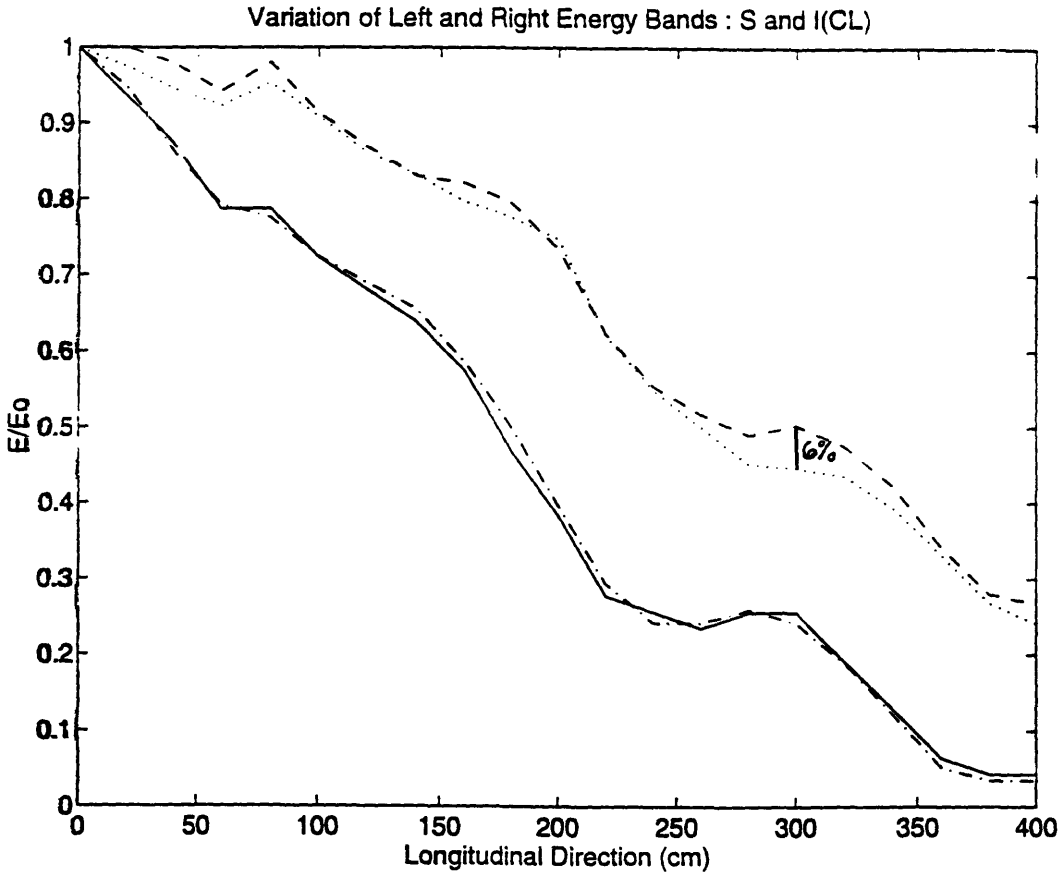

Figure 3.17 Wave energy dissipation due to breaking (spiller, centerline x = 0). Incipient left (——), spiller left (-·-·-·), incipient right (---), spiller right (···).

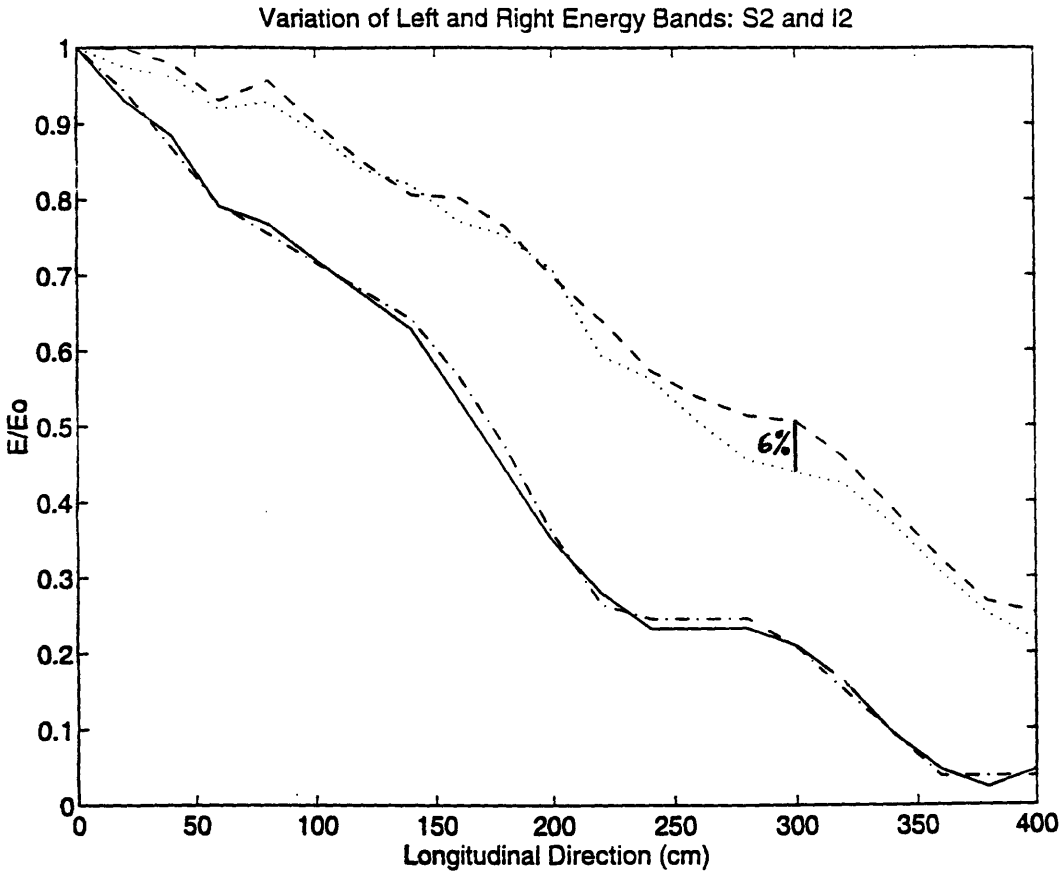

Figure 3.18 Wave energy dissipation due to breaking (spiller, x = -30cm). Incipient left (——), spiller left (-·-·-·), incipient right (---), spiller right (···).

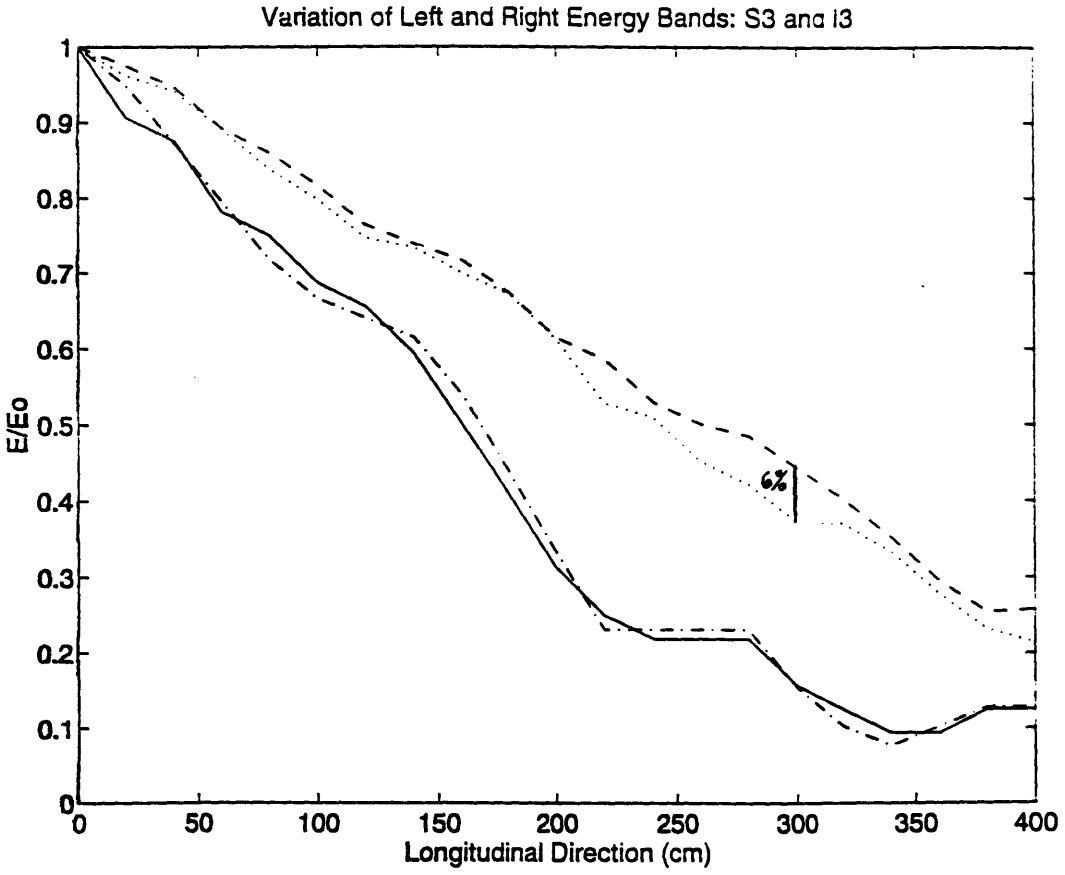

Figure 3.19 Wave energy dissipation due to breaking (spiller, x = -60cm). Incipient left (——), spiller left (-·-·-), incipient right (---), spiller right (···).

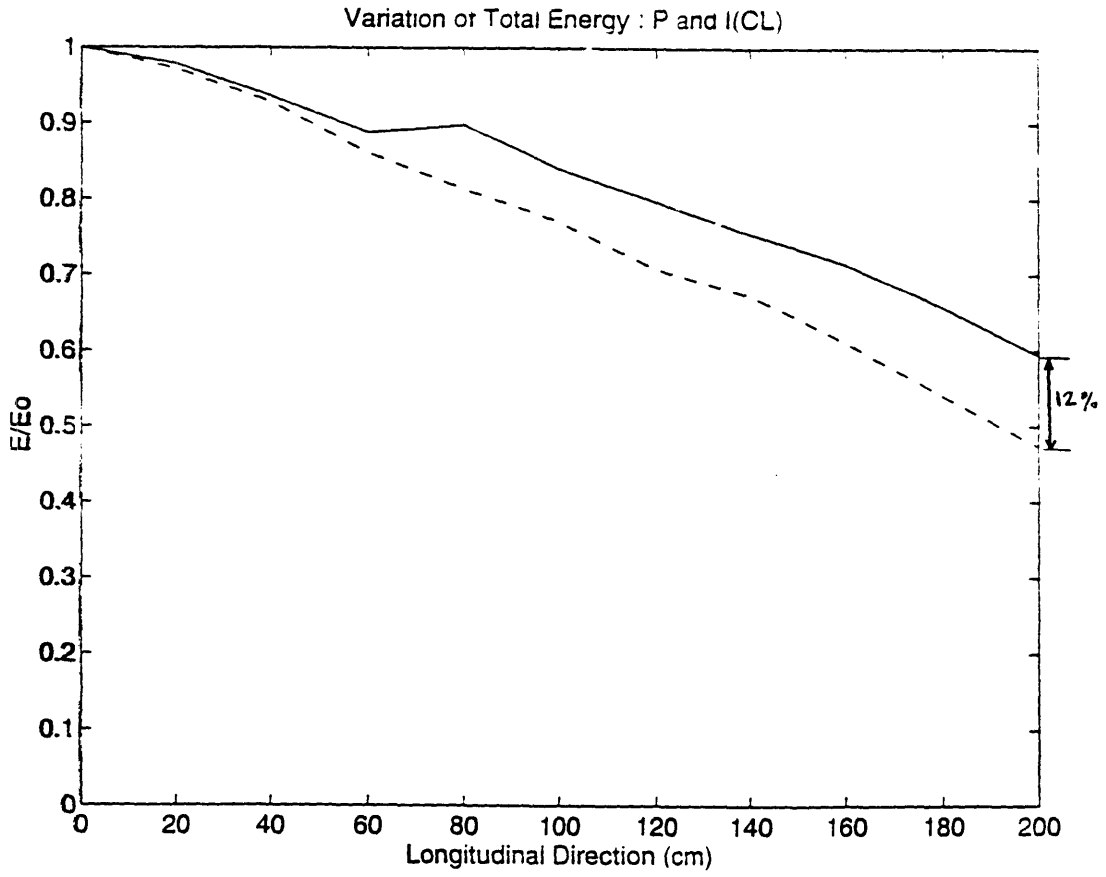

Figure 3.20 Wave energy dissipation due to breaking (plunger, centerline x = 0). Incipient (____), plunger (---).

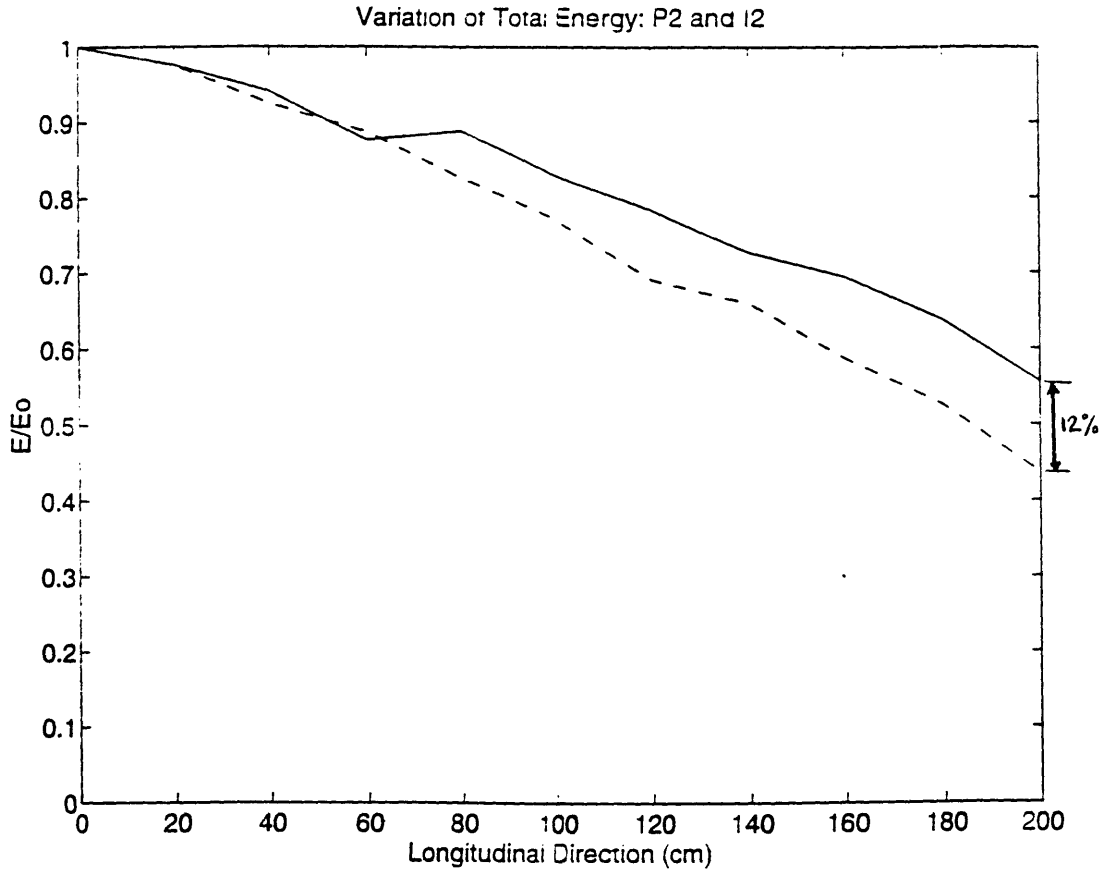

Figure 3.21 Wave energy dissipation due to breaking (plunger, x = -30cm). Incipient (____), plunger (---).

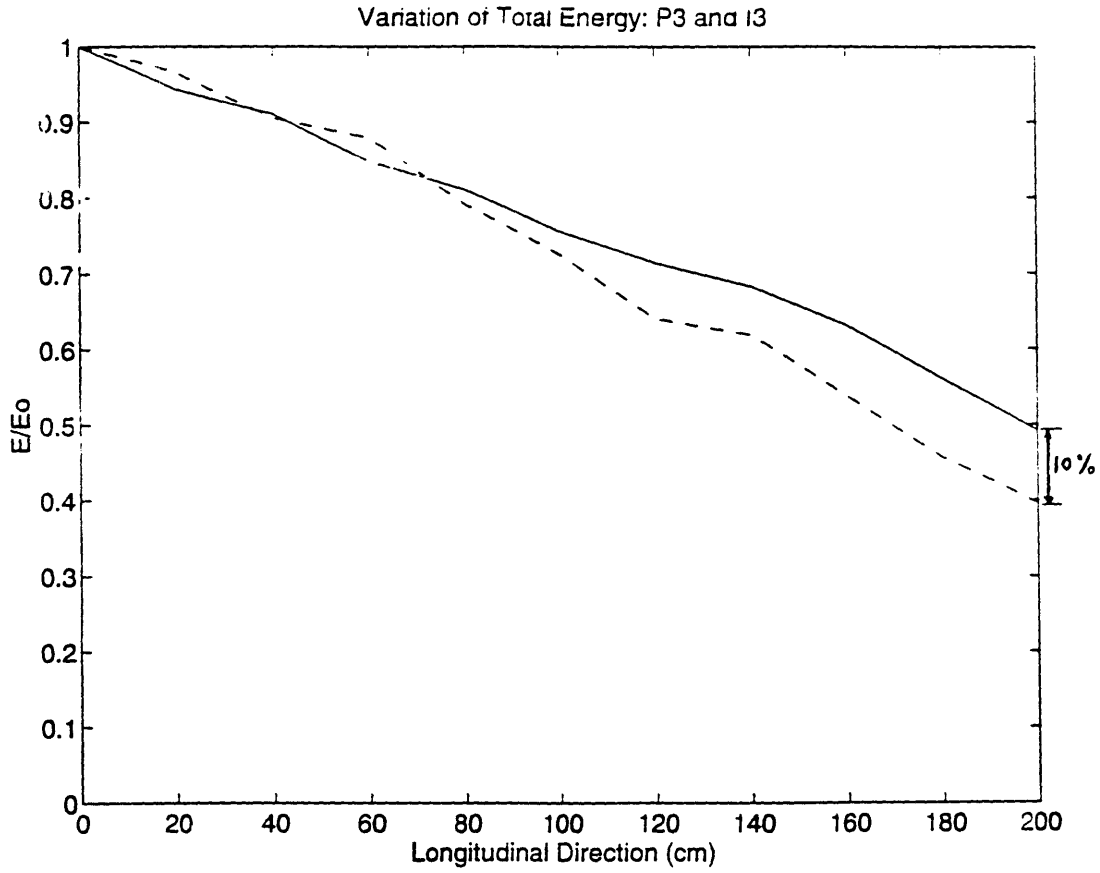

Figure 3.22 Wave energy dissipation due to breaking (plunger, x = -60cm). Incipient (——), plunger (---).

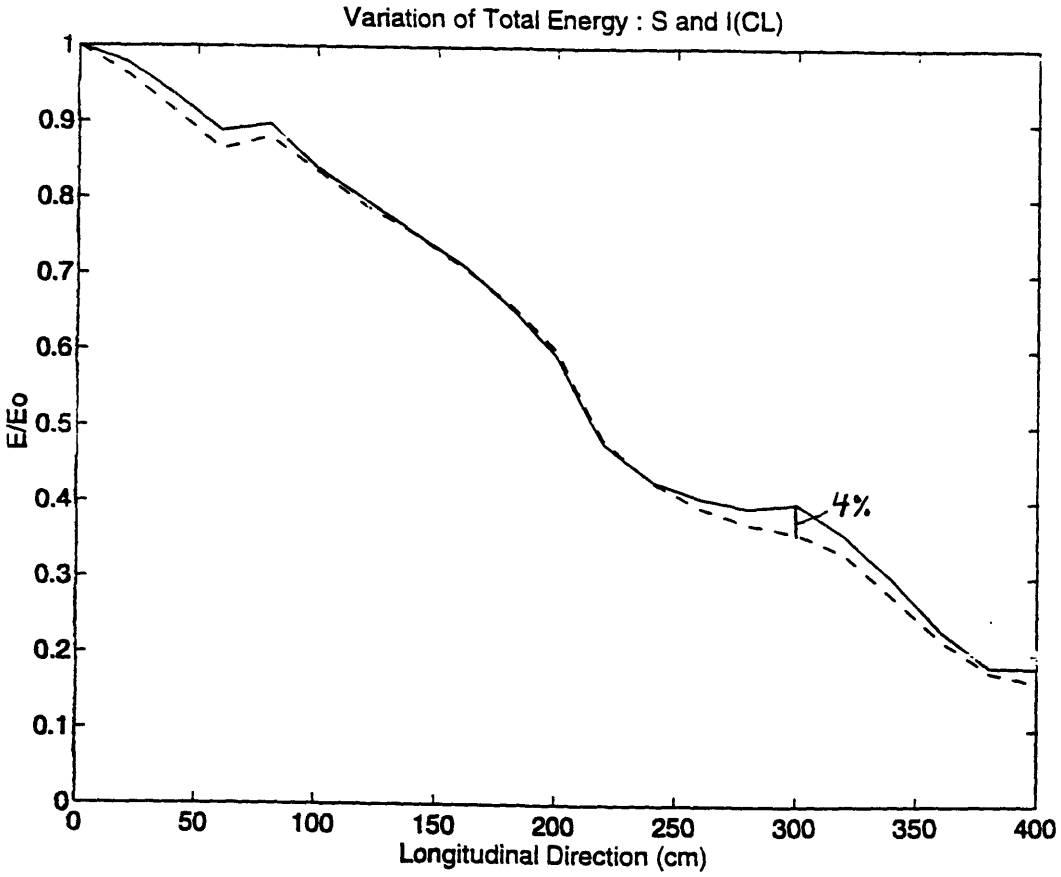

Figure 3.23 Wave energy dissipation due to breaking (spiller, centerline x = 0). Incipient (——), spiller (---).

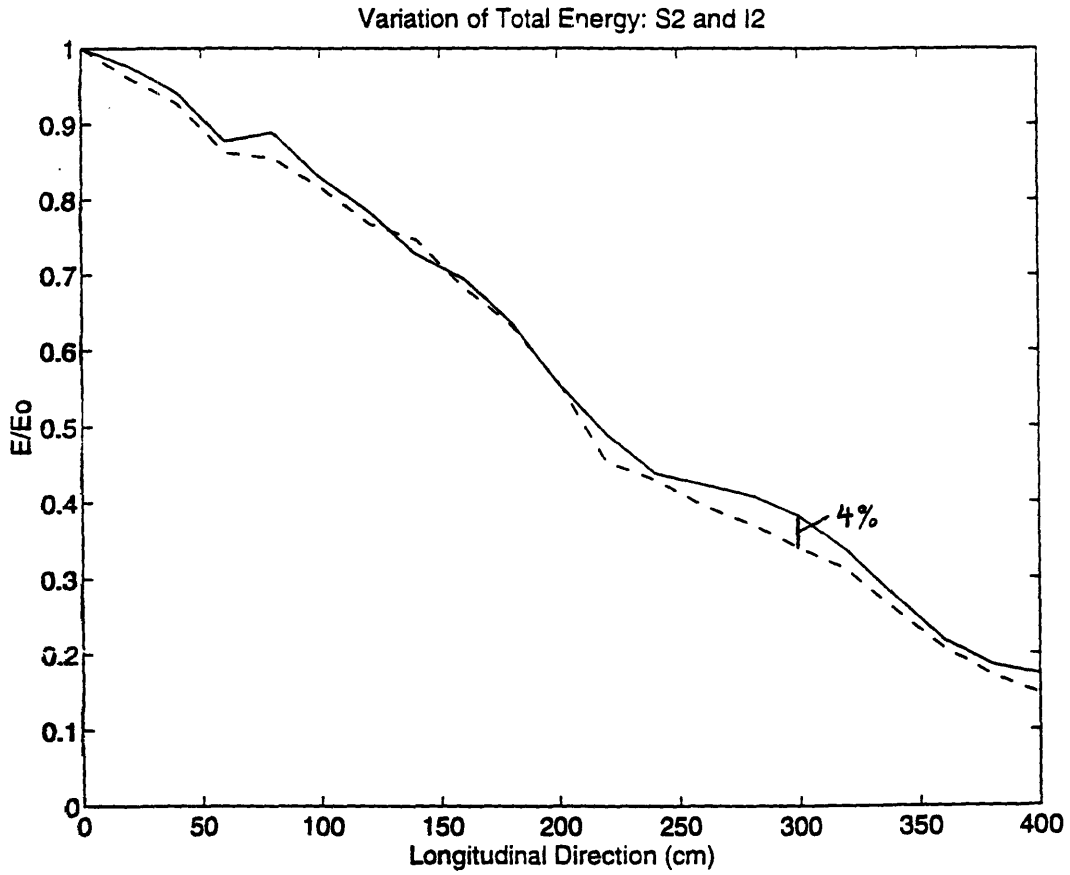

Figure 3.24 Wave energy dissipation due to breaking (spiller, x = -30cm). Incipient (——), spiller(---).

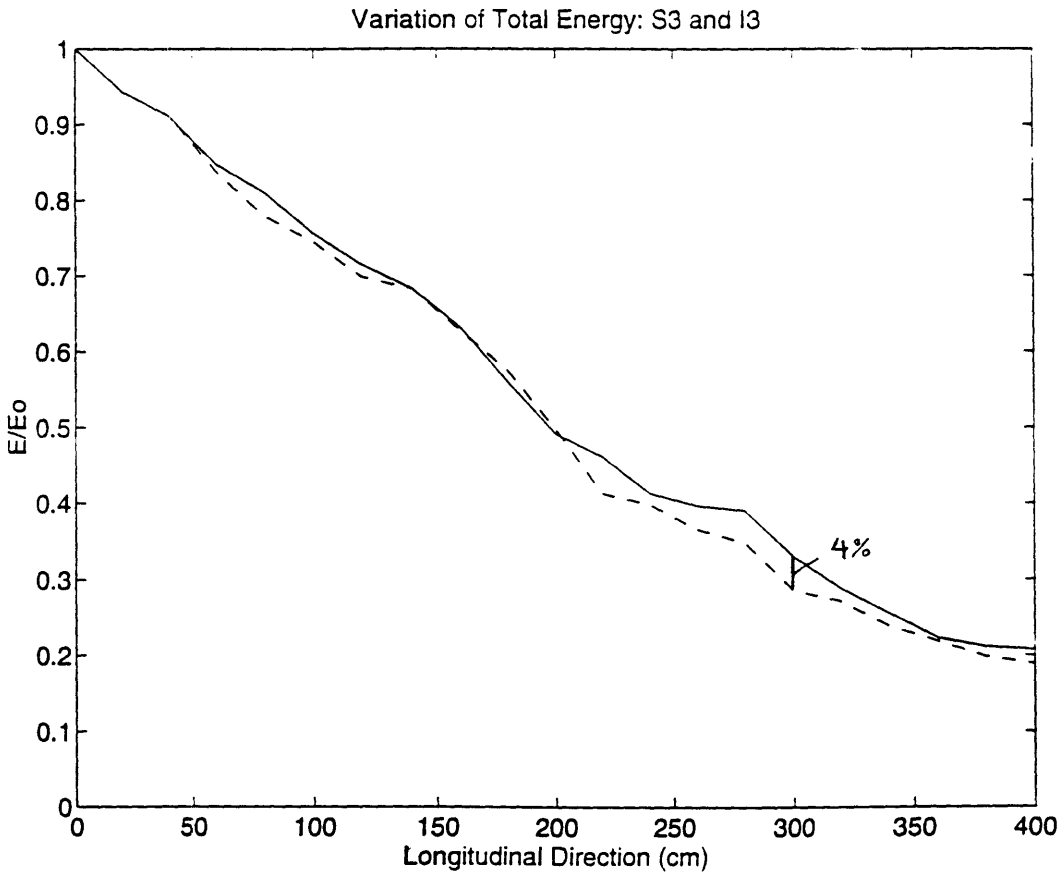

Figure 3.25 Wave energy dissipation due to breaking (spiller, x = -60cm). Incipient (——), spiller (---).

3.4.3 Comparison to Work Done by RM

In the work of RM, the conditions in the flume were assumed to be uniform in the lateral direction. Hence, at any station, only one wave gage was positioned to describe the uniform value of the propagating wave packet at that location. The flume was 25m long and 0.78m wide. The control volume was defined as a major portion of the length of the flume. There were two types of energy losses in this case: viscous dissipation and breaking. Since, the flume was long and narrow, viscous dissipation amounted to 10%. This was seen in the fractional loss of energy for the incipient case (figure 3.2.1a; Rapp, 1986). Note that the viscous dissipation estimates done by RM were off by a factor of 2, so the line due to the boundary layer dissipation was not plotted correctly, and in fact the boundary losses are in good agreement with the observed incipient case.

The control volume was long enough for the wave packet to be dispersed both sufficiently upstream and downstream of the breaking region. Hence, the waves were practically linear, and the equipartition of energy between kinetic and potential was applied. The percentage loss of wave energy from the potential energy measurements would be the same as that for the total wave energy. The total wave energy dissipated for the isolated plunger case with $ak_c = 0.39$ and $f_c = 1.08$Hz is about 28% , which would imply a dissipation of 18% for the isolated plunger case due to the breaking activity alone.

The plunger in the wave basin has an $ak_c = 0.45$. However, before any useful comparison can be made between the two studies, the ak_c for the basin needs to be modified to an equivalent characteristic wave steepness, ak_{c2}, which would produce the same signal at the wave gauges just prior to breaking if no leakage takes place. In other words, using the ak_c at hand is not correct for comparative purposes since leakage effects attenuate the amplitude of the wave packet which is a phenomena that does not occur in a narrow flume. So, in order to draw a comparison between the two studies, the term ak_{c2} is introduced.

The term ak_{c2} for the isolated plunger case turns out to be 0.37 (Appendix 3). Although the isolated plunger in the flume had an $ak_c = 0.39$, the dissipation value at $ak_c = 0.37$ was found also. From Table 3.1, the energy dissipated due to breaking in the basin is 12% at the centerline of the breaker, whereas in the flume, for the same ak_c, it is 18%.

Similarly, the ak_{c2} for the spiller and the incipient are 0.25 and 0.23 respectively (Appendix 3). Table 3.2 summarizes the results. Column (3) are the losses associated with column (2), which are the isolated breakers in the flume. Columns (5) and (6) are the losses associated with column (4) for the basin and flume respectively. The tabulated values might be somewhat misleading since a spiller was not observed in the flume until

ak_c attained values greater than 0.25, and so all values below that had no breaking loss. However, after the RM runs hit the 0.25 value, there was a sharp increase in the breaking loss values.

Table 3.2 Characteristic Wave Steepness and Dissipation Estimates due to Breaking

Breaker Type	Col. (1) ak_c (basin)	Col. (2) ak_{cRM}	Col. (3) Loss (RM)	Col. (4) ak_{c2}	Col. (5) Loss (basin)	Col. (6) Loss (RM)
Plunger	0.45	0.39	18%	0.37	12%	18%
Spiller	0.32	0.29	12%	0.25	4%	0%
Incipient	0.29	0.25	0%	0.23	0%	0%

The estimates obtained in the basin seem to somewhat underestimate the expected dissipation noted in the flume (comparison of columns (3) and (5)). However, the control volume defined is not a region in which the wave packet is dispersed, the waves linear, the energy equipartitioned, and most importantly, it is not a region in which the waves propagate unidirectionally. Hence, two suggestions are in order to further refine the energy dissipation estimates for the wave packets in the basin. The first is to also measure the velocity record at the given grid locations to get the kinetic energy. The second is to develop a model that describes the propagation of the wave packet in *two* dimensions as does occur in the wave basin. These two points are further discussed in Chapter 5.

CHAPTER 4

Wave Steepness

4.1 Wave Steepness Definition

The steepness of a wave is roughly the height to length ratio. It is a dimensionless number that is formed from the ratio of a vertical length scale to a horizontal length scale. There is no set definition as to which vertical length scale is the correct one to use, nor is there one for the horizontal length scale. Two different definitions are used in this chapter. The first is ak_c, the characteristic wave steepness, and the second is ak, the instantaneous wave steepness. Both are explained in detail below.

ak_c - characteristic steepness

In Chapter 2, the concept of characteristic wave steepness, ak_c, was introduced. To reiterate, it is the product of a, the amplitude of the individual central frequency component, and k_c, the central wavenumber. The wave group is a frequency modulated signal, and since it is difficult to isolate all the different frequencies involved, the packet is characterized by its central frequency (or central wavenumber, k_c). The practical use of such a term can be noted for field applications since it is easier to obtain and work with characteristic values that are representative of the sea state rather than with a detailed description of the waves in each breaking cell. The term ak_c is discussed extensively by RM. Based on a series of experiments, they further advocate their choice of describing wave steepness by this term (figures 3.4.2 through 3.4.4; Rapp, 1986). Moreover, it is a term which is relatively easy to parametrize.

ak - instantaneous steepness

In this term, the amplitude, a, represents the instantaneous amplitude at a given point defined as half the instantaneous height. The wavenumber k is the inverse of the instantaneous wavelength in the prescribed local region of interest. An accurate analysis of the evolution of the envelope requires monitoring the local wave steepness. A true understanding of the wave breaking process cannot be understood without the actual computation of the exact wave steepness at every point in time and space.

The ak term is computed from the time series data of surface displacement. The amplitude, a, is half the crest-trough distance at each gauge location, one can identify the particular wave in the time series $\eta(t)$ distance for the breaking wave (figure 4.1). The half period, T/2, is taken as the time between the peak of the breaking wave and the temporally preceding trough. The local instantaneous wavenumber k is obtained from the dispersion relationship using the period T. Although the wave dispersion relation in three dimensions is slightly different from that for two dimensions, the method described above is adequately representative of the instantaneous wave steepness. This is verified by generating a two-dimensional snapshot of the spatial variation of the wave form by combining wave records at several stations. From that, another estimate of the wave steepness at a point in that snapshot is computed. The two estimates match to within a few percent. The importance of the instantaneous wave steepness term in understanding the breaking process is discussed below.

4.2 Breaking Inception

The onset and persistence of breaking are defined by the appearance of whitecap. The spatial variation of the instantaneous wave steepness, ak, is plotted for the plunger, spiller, and incipient cases (figure 4.2). The generated plunger is quite vigorous and takes place over a distance of about a wavelength ($1.2\lambda_c$, this has been arbitrarily based on the length over which the ak > 0.45 in figure 4.2). The spiller on the other hand is quite weak and takes place within a very localized region ($0.2\lambda_c$). Based on this figure, the inception of breaking appears to correspond to an ak value of 0.45. Note that our data can strictly only indicate that breaking is initiated between 0.41 - 0.45, but for simplicity, the 0.45 value will be used for the remaining discussion. In other words, whitecap starts forming when the wave reaches the steepness of 0.45 for both the plunger and the spiller. The maximum steepness achieved by the incipient wave is 0.37. Stokes (1880) obtained the upper limit steepness that a wave can attain without breaking to be ak = 0.45 which corresponds to a wave height to wavelength ratio, H/L, equal to 1/7. Moreover, considerable research has been done since Stokes' time on the issue of a wave breaking steepness criterion. Analytical and experimental work has been done suggesting critical values of wave steepness between 0.40 to 0.44 (Lighthill, 1967; Longuet-Higgins 1978; Bonmarin, 1985).

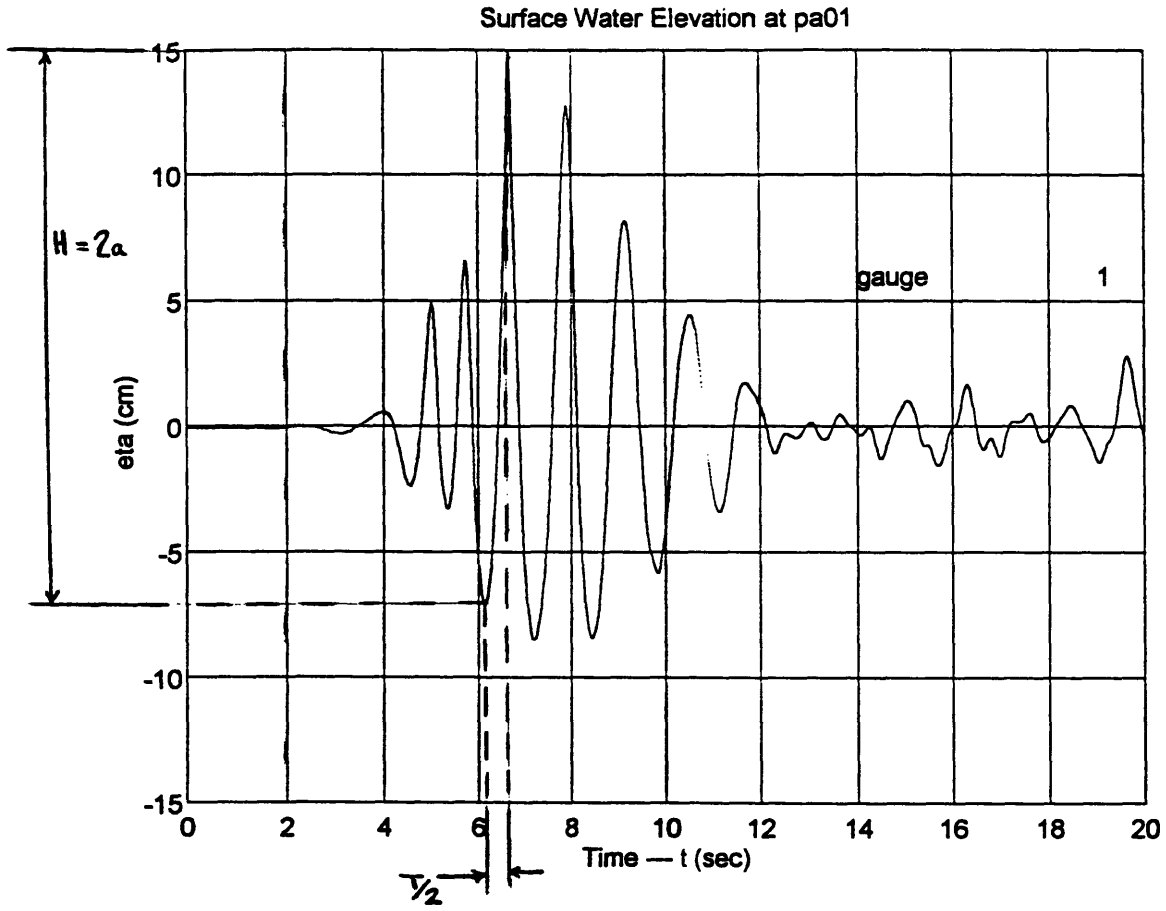

Figure 4.1 Instantaneous wave steepness.

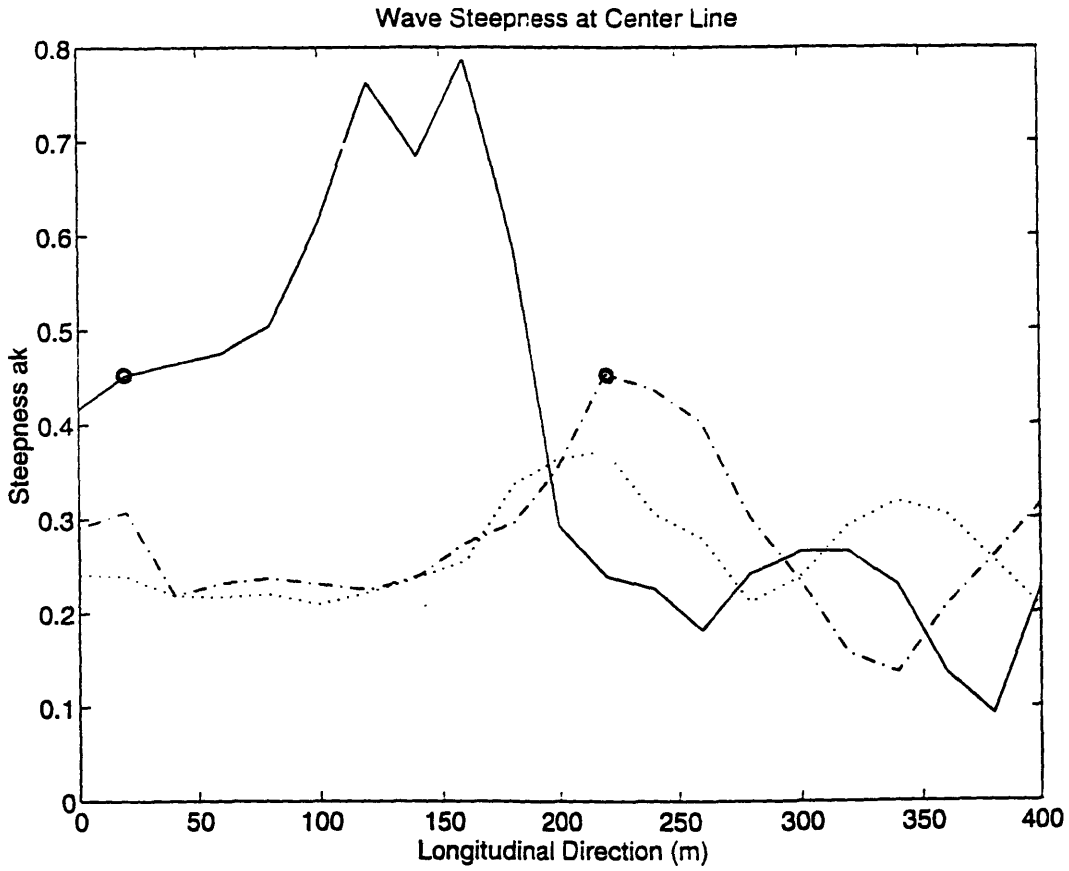

Figure 4.2 Longitudinal variation of ak. Plunger(——), spiller (-·-·-·), incipient (···). 'o' marks start of whitecap.

4.3 Criterion for Predicting Breaking

Many of the experiments referenced above were motivated by examining whether a criteria can be developed that can predict breaking. The wave steepness was thought to be a logical parameter to examine. As it turns out, the limiting wave steepness criterion adequately predicts breaking only if conditions are consistent, but no set value can be universally applicable. The explanation seems to date back to the work done by Benjamin and Feir in 1967 (Benjamin and Feir, 1967). Their work demonstrated that weakly nonlinear free-surface waves are unstable to side-band instabilities, and the tendency to form these instabilities is a function of ak. Therefore ak is an important parameter in the analysis. It is this instability mechanism that triggers breaking. With this in mind, Su and Green (1984) performed a set of experiments in which they generated breaking waves in a very long wave tank (over 100m). They showed that these instabilities are fetch-dependent and can grow and develop as a wave group propagates over longer lengths. From their experiments, they achieved breaking at a considerably lower value of wave steepness since given a longer fetch for the wave group to propagate, there will be a longer interval for the side-band instabilities to develop. In figure 6 of Tulin and Li, 1992, ak = 0.45 value corresponds to an $Ho/gT^2 = 0.023$ which lies way outside the graph. It lies in the region corresponding to the short wave tank which is the experimental facility at hand. Further evidence of the Benjamin-Feir instability was presented Holthuijsen and Herbers (1986) when they conducted an experiment in the North Sea. They found that breaking waves in the field occur over a wide range of wave steepness, including the smallest values, and that there is a complete overlap of regimes of breaking and non-breaking waves. However, the breaking waves had a steeper mean value than the non-breaking, but not by much. Hence, this study also points to the fact that the usage of the limiting criterion for wave steepness over a short length is not universally applicable since it is typical for wave groups to travel considerable distances in the ocean before breaking occurs. Yet, this criterion is applicable for predicting breaking under conditions of rapid focusing as does happen, for example, in the case of a bow wave on a ship.

Some studies have examined the rate of change of wave steepness rather than the wave steepness itself as an indicator of breaking (Van Dorn, 1975). The result of Van Dorn's work was that the wave growth rate is important in predicting breaking. To date, no satisfactory criterion has been developed that can accurately predict breaking.

So, in the current study, in order for a wave to break within a very short length, the wave has to build up quite rapidly, and thus its wave steepness attains values very close to the critical value described by Stokes.

4.4 Wave Steepness Table

The wave steepness is summarized in Table 4.1 below. The first column shows the values obtained when the whitecap starts forming. The third and fifth columns are the characteristic wave steepness values obtained for this experiment and for the RM experiment. The fourth column is the equivalent two-dimensional characteristic wave steepness introduced in section 3.4.3.

It is observed that the values for the three-dimensional case are consistently larger than those of the two-dimensional case (column (3) > column (5)). The reason for that is primarily because of lateral leakage of energy from the control volume in the breaker in the present study. To compensate for this radiation of energy, the gain had to be increased. The value for the uniform 2D plunger though is also slightly larger than its flume counterpart. Recall that the flume length was 25m, and the wave broke about 10m downstream, whereas the fetch over which the wave propagates before breaking is about 4m in the basin. Hence, it is consistent with the discussion on the Benjamin-Feir instability, for the characteristic wave steepness of the uniform case in the basin to be slightly larger than the uniform one in the flume. So, the third column lists the current values for the characteristic wave steepness while the fifth column lists those that were obtained in the RM experiment.

The second column represents a wave steepness based on the instantaneous amplitude a obtained from the first column multiplied by the characteristic wavenumber. This column is remarkably similar in value to the third column. Since the central wavenumber is the same constant, then the second and third columns are similar because the instantaneous amplitude at the point of breaking inception is identical to the amplitude of the central component of the input signal. That is somewhat of a coincidental result. No further investigation was conducted to see if there is any basis for that or not.

Table 4.1 Wave Steepness

Breaker Type	Column (1) Instantaneous $ak^{(1)}$	Column (2) Instantaneous $ak_c^{(2)}$	Column (3) $ak_c^{(3)}$	Column (4) $ak_{c2}^{(4)}$	Column (5) $ak_c^{(5)}$ (RM)
Plunger	0.45	0.47	0.45	0.37	0.39
Spiller	0.45	0.30	0.32	0.25	0.29
Incipient	0.37	0.28	0.29	0.23	0.25
2D Plunger	0.45	0.47	0.42	0.42	0.39

1. Instantaneous ak at the initiation of breaking for P, S; maximum instantaneous ak for I.
2. ak_c based on the instantaneous amplitude derived from column (1).
3. ak_c based on the RM definition of characteristic wave steepness.
4. ak_{c2}: equivalent two-dimensional characteristic wave steepness.
5. ak_c of the RM characteristic wave steepness.

4.5 Lateral Variation of ak and Dissipation Estimates due to Breaking

Due to the three-dimensionality of the breaking wave, there is a lateral variation in the wave steepness values at breaking.

Plunger:

Figure 4.3 shows a plot of the lateral variation of the wave steepness across the plunger. The region shown with wave steepness larger than the critical value of 0.45 corresponds to that region in which breaking is observed. For steepness values lower than 0.45, no breaking is observed.

Figure 4.3 can be viewed as a top view of the basin. Conceptually, one can think of the 4m width of the test section as being comprised of several channels adjacent to one another. The channels are taken to be 30cm wide since the wave gauges are 30cm apart in the lateral direction. Seven channels are defined that span half the width of the basin (i.e. 2m). The control volume spans 5 out of the 7 channels. Dissipation estimates from Table

3.1 are shown in the figure. The channels with wave steepness values below the critical value have no dissipation due to breaking. This is assumed based on the fact that no breaking is observed in those channels. For the plunger case, the dissipation estimates in channels 4 and 5 are labeled with question marks since the exact values cannot be obtained from the wave gauge records due to wall effects. However, it is clear that the values are below 10%.

Spiller

Similarly, figure 4.4 depicts the lateral variation of ak across the spiller. The critical value of 0.45 is indicated. In this case, channel 4 has an uncomputed dissipation estimate. Again, the value is clearly less than 4%. For channels 5, 6, and 7, the dissipation is based on no visual breaking.

Incipient

Figure 4.5 shows the wave steepness variation across the incipient wave. As is discussed in Chapter 3, it is assumed that no dissipation occurs for values of ak less than 0.45. For this case, all values obtained are below the critical value as is anticipated.

Figure 4.6 shows the three cases on the same plot for comparative purposes. Again, the region on the graph above ak = 0.45 reflects breaking while the lower portion does not exhibit any breaking.

Figure 4.7, similar to figure 4.6, shows the lateral variation of the characteristic wave steepness, ak_c. A similar trend is observed, but the ak_c values are less than those of the instantaneous wave steepness, ak. Much as a critical steepness of 0.45 is defined for ak, a value of about 0.30 can be visually assigned as a critical ak_c value.

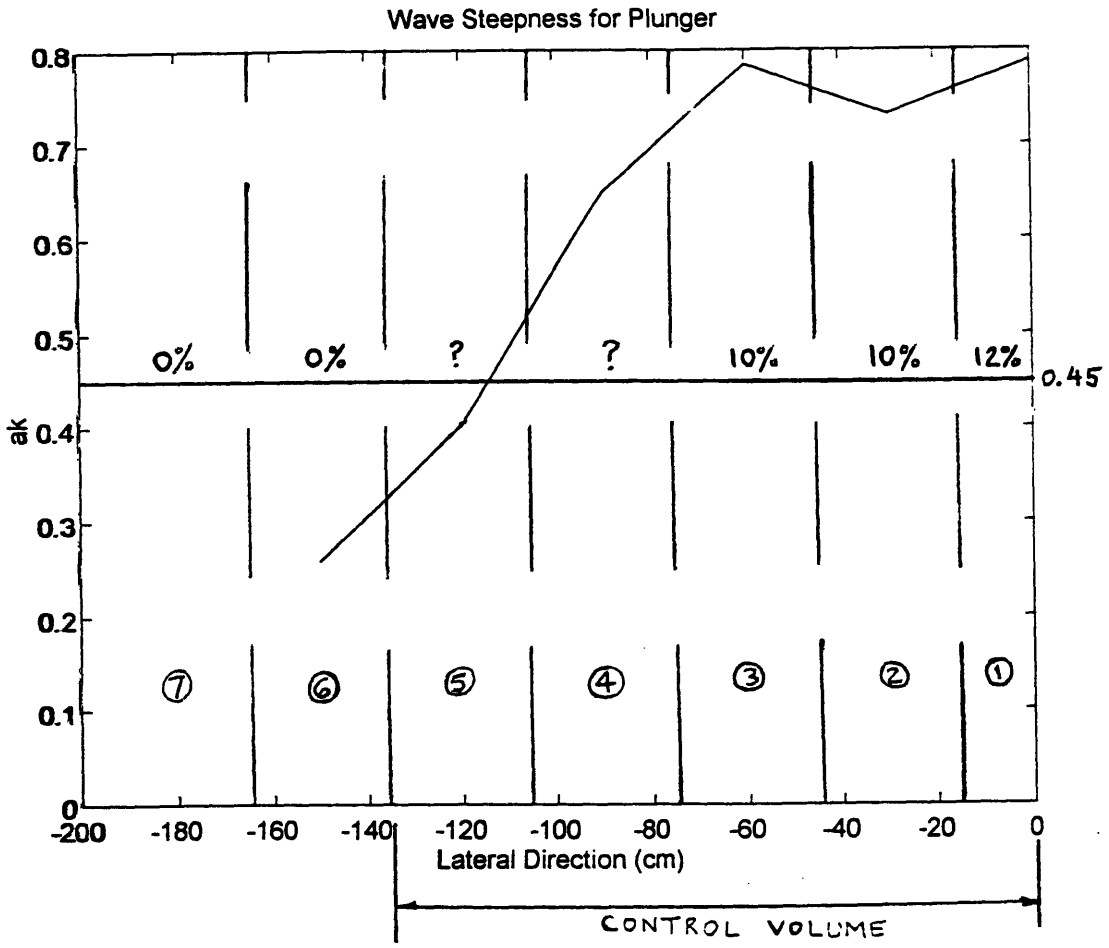

Figure 4.3 Lateral variation of ak (plunger). The 7 channels and the associated dissipation estimates due to breaking.

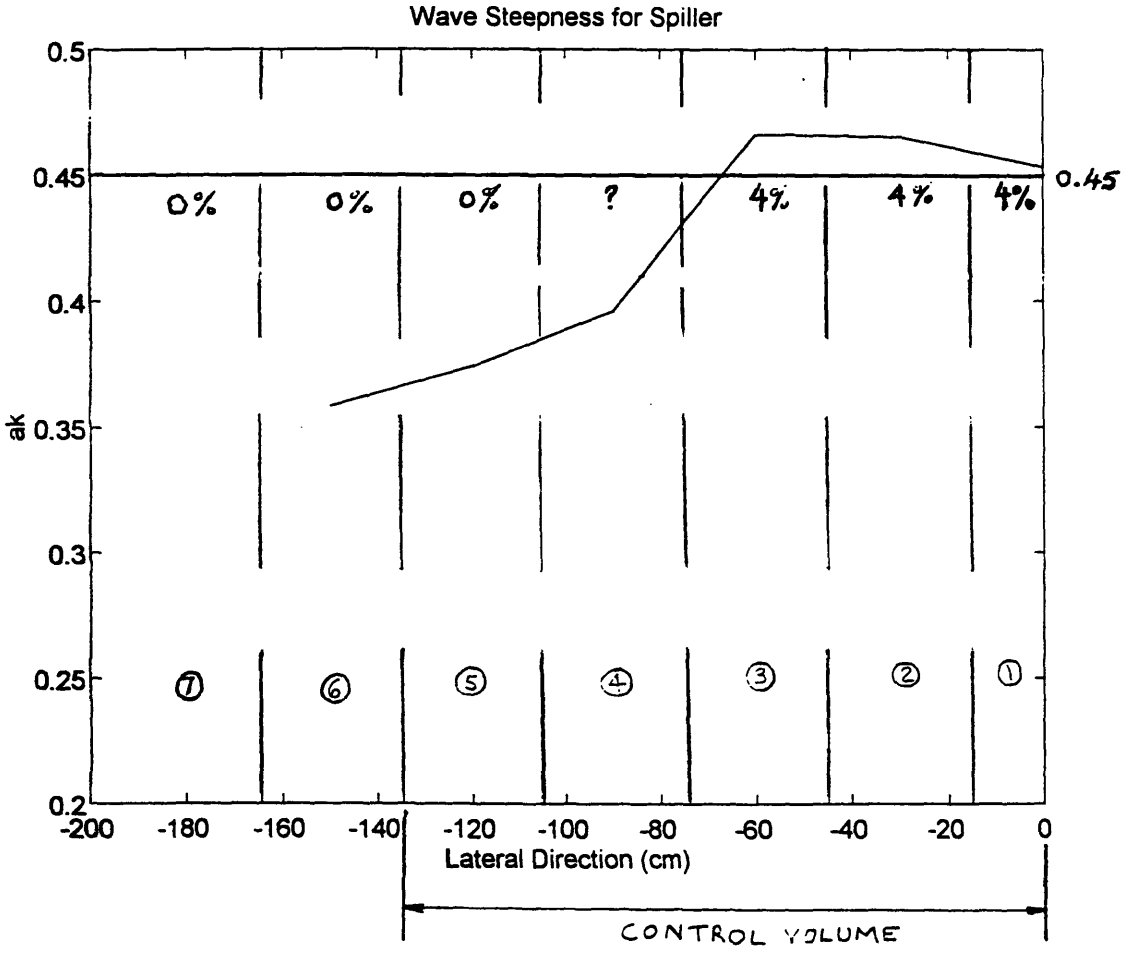

Figure 4.4 Lateral variation of ak (spiller). The 7 channels and the associated dissipation estimates due to breaking.

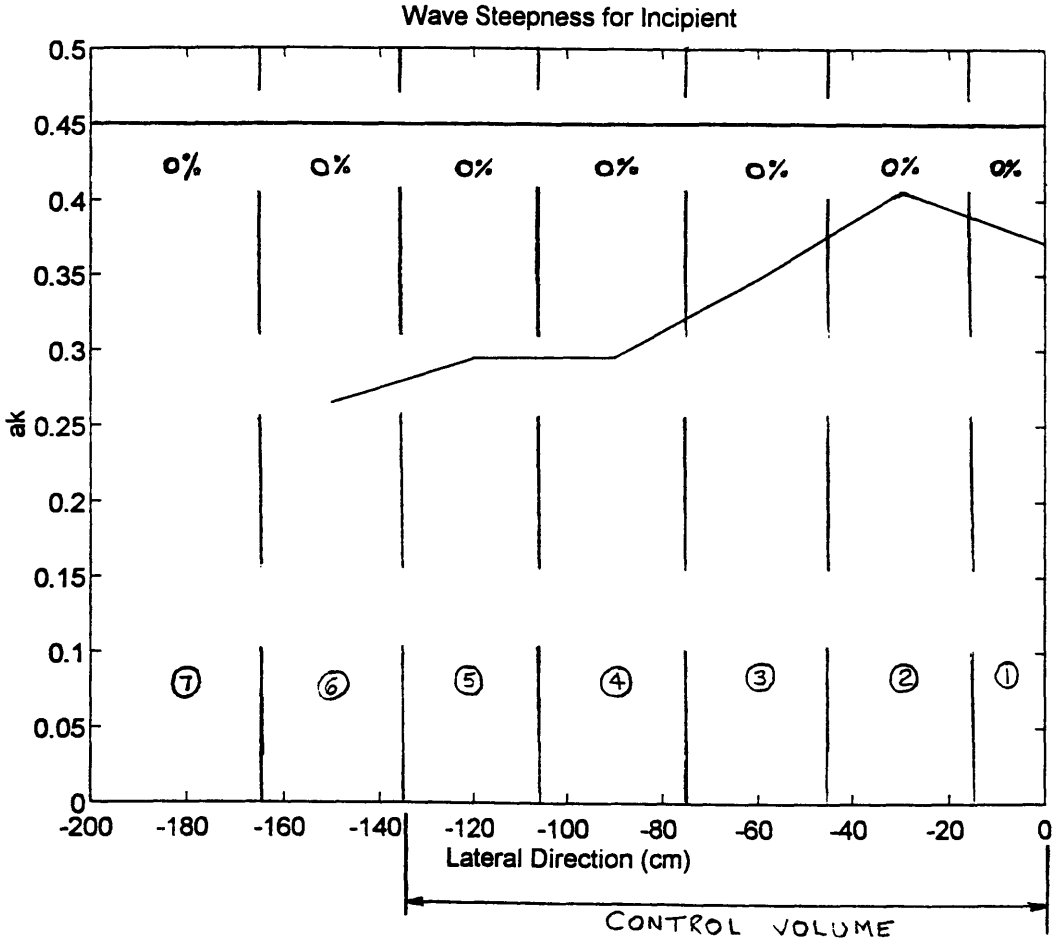

Figure 4.5 Lateral variation of ak (incipient). The 7 channels are defined, and there is no dissipation for the incipient case.

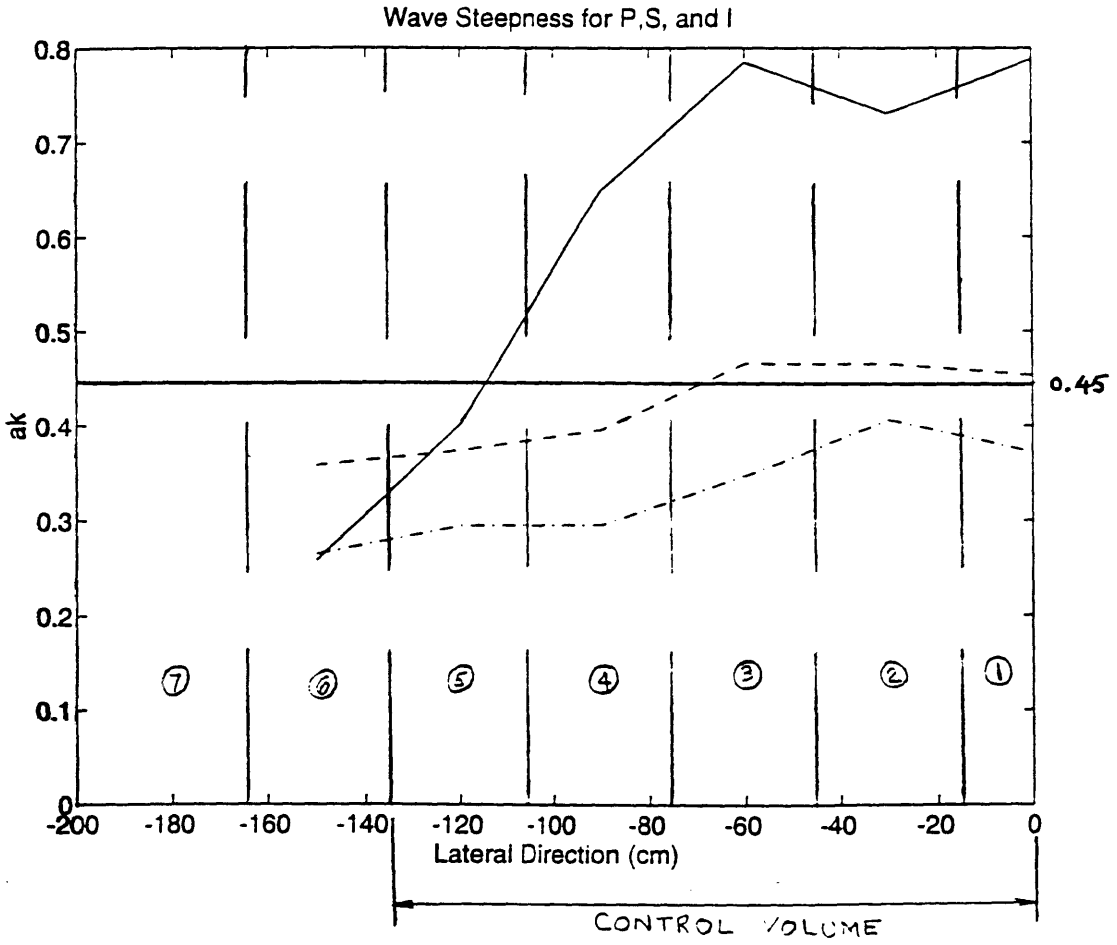

Figure 4.6 Comparison of lateral variation of ak. Plunger (___), spiller (---), incipient (-·-·-·). Critical ak = 0.41.

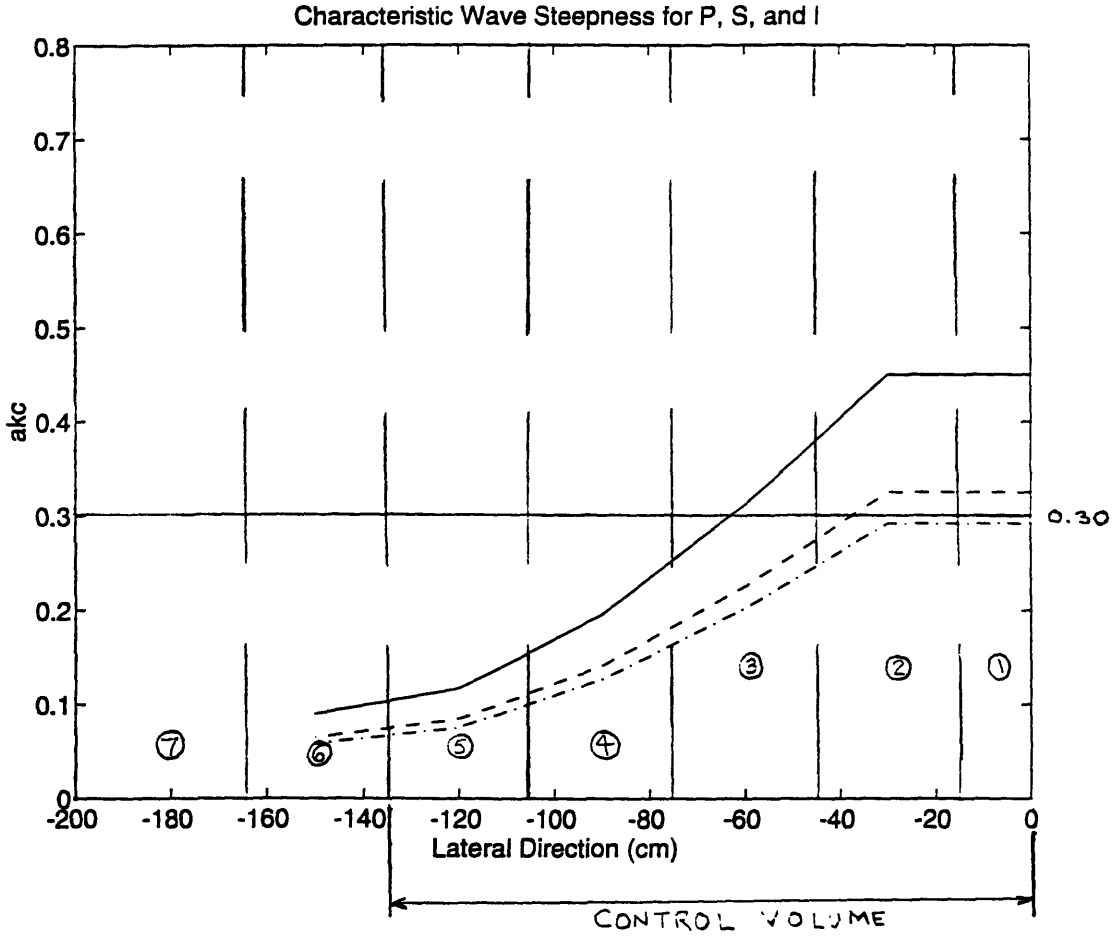

Figure 4.7 Comparison of lateral variation of ak_c. Plunger (——), spiller (---), incipient (-·-·-·). Critical $ak_c = 0.30$.

CHAPTER 5

Conclusions and Recommendations

5.1 Summary and Conclusions

Three-dimensional breaking waves are generated in a wave basin. The principle of superposition of multiple wave components is used to generate the breaker at a specified location. Three cases are run: plunger, spiller, and incipient. The signal is identical for all three cases except for the gain. Reflection effects from both the wall and the beach are excluded from the analysis. Viscous dissipation computed from the incipient case is essentially negligible for the test section that is 4m x 4m. After isolating the wave energy loss due to leakage effects, the dissipation due to breaking is obtained. The estimate for the plunger case is 12% and 4% for the spiller. The critical wave steepness value obtained for a rapidly steepening wave is ak = 0.45 while the corresponding critical value for the characteristic wave steepness is ak_c=0.30. Dissipation estimates due to breaking for waves with less steepness are assumed to be 0%.

A comparison is made between this study and that done by RM in a 2-D flume. The dissipation estimates are in reasonable agreement (see table 3.2) with the observed values in the basin, but are slightly less. The ak_c values required to produce the isolated breakers are slightly larger for the present set of experiments because of two reasons. First, energy is being radiated away from our control volume requiring a compensating increase in gain. Second, considering the evolution of the Benjamin-Feir instability, we expect waves to break at lower steepnesses given a longer propagation distance, as in the flume.

Having defined the various characteristics of the wave packets of interest, the project can advance to the next stages.

5.2 Future Work

The next step of this project is to study the evolution of the entrained bubble cloud. Parameters such as depth of penetration and persistence of the turbulent cloud will be studied. These can be viewed as output parameters of the breaking event. Having the

characteristic wave parameters determined above (which can be thought of as input conditions), the new output parameters can be expressed in terms of them. The experimental setup for this phase is fully operational. The setup includes a COHU underwater camera (monochrome) that will be filming at 33ms per image. These images can be viewed directly on the computer monitor via a Data Translation 3501 frame grabber card. The software that does the image processing, Global Lab Image, is also from Data Translation. The images will be saved on a video cassette for processing. The images will represent cross-sections, both in the longitudinal and lateral directions, of the three-dimensional flow field. These cross-sections are demarcated by a lightsheet generated by having a Coherent, Inc. 5W argon ion laser beam which is passed through a 10m fiber optic cable and expanded by a cylindrical lens. Since the beam will pass through a 10m length of fiber optic cable, its power will be attenuated to 3.2W at the output end.

A third stage in this project will entail doing velocity measurements of the flow field. This will be done using Laser Doppler Velocimetry (LDV) with a system purchased from Dantec. The argon ion laser used in this case is fan cooled since it is rated at 300mW. The focal length of the probe which is 16cm in air will be 28cm when fully submersed in water. The system can measure velocities in the two directions parallel to the lens. The first reason for doing velocity measurements is to study the turbulence associated with breaking. The second is to obtain the associated kinetic energy of the wave packet since the above analysis is based only on the potential energy measurements which provides good first estimates of the dissipation.

Furthermore, the wave packet does not propagate unidirectionally. Hence, a two-dimensional energy model has to be developed that incorporates the bidirectional propagation of the wave envelope. The experimental data will be used to verify the model and to compute the dissipation estimates for the different breakers.

Finally, it is suggested that the spiller be moved upstream so that it falls in a region, i.e. the control volume shown in figure 3.5, that is not affected by beach or wall reflection. This will likely require the existence of two spillers in the basin; however, the analysis for the upstream spiller, which is of interest, should be unaffected by the occurrence of a second one further downstream.

Future work in the wave basin might also include expanding the width of the test section. There are two main advantages in doing that. First, the effect of the side wall can be eliminated, and second, the crest length can be varied.

REFERENCES

Banner, M.L. 1990. "The influence of wave breaking on the surface pressure distribution in wind wave interactions," Journal of Fluid Mechanics, 211: 463-495.

Banner, M.L. and Cato, D.H. 1988. "Physical mechanisms of noise generation by breaking waves - a laboratory study," Sea Surface Sound - Natural Mechanisms of Surface Generated Noise in the Ocean, ed. Kerman, B.R., pp.429-436. Dordrecht: Kluwer. 639 pp.

Banner, M.L. and Fooks, E.H. 1985. "On the microwave reflectivity of small-scale breaking water waves," Proceedings of the Royal Society, London Series A, 399: 93-109.

Banner, M.L. and Melville W.K. 1976. "On the separation of air flow over water waves," Journal of Fluid Mechanics, 77: 825-891.

Banner, M.L. and Peregrine, D.H. 1993. "Wave breaking in deep water," Annual Review of Fluid Mechanics, 25: 373-397.

Benjamin, T.B. and Feir, J.E. 1967. "The disintegration of wave trains in deep water. Part 1. Theory," Journal of Fluid Mechanics, 27: 417-430.

Bonmarin, P. 1989. "Geometric properties of deep-water breaking waves," Journal of Fluid Mechanics, 209: 405-433.

Bonamarin, P and Ramamonjiarisoa, A. 1985. "Deformation of breaking of deep water gravity waves," Experiments in Fluids, 3: 11-16.

Csanady, G.T. 1990. "Momentum flux in breaking wavelets," Journal of Geophysical Research, 95(C8): 13289-13299.

Dean, R.G. and Dalrymple, R.A. 1984. *Water Wave Mechanics for Engineers and Scientists*, Prentice-Hall, Inc.

Dommermuth, D.G., Yue, D.K.P, Lin, W.M., Rapp, R.J., Chan, E.S., and Melville, W.K. 1988. "Deep-water plunging breakers: a comparison between potential theory and experiments," Journal of Fluid Mechanics, 189: 423-442.

Donelan, M., Longuet-Higgins, M.S., and Turner, J.S. 1972. "Periodicity in whitecaps," Nature, 239: 449-450.

Greenhow, M. 1983. "Free surface flows related to breaking waves," Journal of Fluid Mechanics, 118: 221-239.

Holthuijsen, L.H. and Herbers, T.H.C. 1986. "Statistics of breaking waves observed as whitecaps in the open sea," Journal of Physical Oceanography, 16: 290-297.

Hunt, J.N. 1952. "Viscous damping of waves over an inclined bed in a channel of finite width," Houille Blanche, 6: 836.

Kjeldsen, S.P. 1984. "Whitecapping and wave crest lengths in directional seas," Symposium on Description and Modelling of Directional Seas, Paper no. B-6.

Kjeldsen, S.P. and Myrhaug, D. 1978. "Kinematics and dynamics of breaking waves," *Report STF60 A78100. Ships in Rough Seas, Pt. 4.* Trondheim: Norwegian Hydrodynamics Labs.

Lighthill, M.J. 1967. "Some special cases treated by the Whitham theory," Proc. Roy. Soc. Lond. A, 299: 28-53.

Longuet-Higgins, M.S. 1974. "Breaking waves in deep or shallow water," Proccedings 10th Conference on Naval Hydrodynamics, M.I.T., 597-605.

Longuet-Higgins, M.S. 1978a. "The instabilities of gravity waves of finite amplitude in deep water. I. Subharmonics," Proc. Roy. Soc. Lond. A, 360: 471-488.

Longuet-Higgins, M.S. 1978b. "The instabilities of gravity waves of finite amplitude in deep water. II. Subharmonics," Proc. Roy. Soc. Lond. A, 360: 489-505.

Longuet-Higgins, M.S. 1980. "On the forming of sharp corners at a free surface," Proc. Roy. Soc. Lond. A, 371: 453-478.

Perlin, M. 1995. ONR Conference "Free Surface Turbulence," Pasadena, Feb28 - Mar3 1995.

Rapp, R.J. and Melville, W.K. 1990. "Laboratory measurements of deep water breaking waves," Phil. Trans. R. Soc. London Ser. A, 331: 735-780.

She, K., Greated, C.A., and Easson, W.J. 1992. "Experimental study of three-dimensional wave," Preprint, Edinburgh University Physics Department.

She, K., Greated, C.A., and Easson, W.J. 1994. "Experimental study of three-dimensional wave breaking," Journal of Waterway, Port, Coastal, and Ocean Engineering, 120(1): 20-36.

Su, M.Y. and Green, A.W. 1984. "Wave breaking and nonlinear instability coupling," The Ocean Surface, pp 31-38.

Toba, Y. and Chen, M. 1973. "Quantitative expression of the breaking of wind waves on the sea surface," Recordings Oceanography Works (Japan), 23: 1-11.

Tulin, M.P. and Li, J.J. 1992. "On the breaking of energetic waves," International Journal of Offshore and Polar Engineering, 2(1): 46-53.

Van Dorn, W.G. and Pazan, S.E. 1975. "Laboratory investigation of wave breaking," Scripps Institute of Oceanography. Ref. No. 75-121, AOEL Report No. 71.

APPENDIX 1

BREAKING WAVE GENERATION PROGRAM

```
/*****************************************************************/
/* PIPELINE.C
/* March 1994
/* Ziad Zakharia
/*
/* This program generates a breaking wave in the wave basin.
/* The wave-wave interaction induced breaking is generated by a frequency
/* modulated wave packet.
/* Note that the conditions produced are that of deep-water waves.
/* One has to specify the breaking location, time to breaking, and water
/* depth. Moreover, one has to enter the center frequency of the wave
/* train and the frequency range. The frequency-modulated waves in the
/* wave train have constant steepness of 0.1.
/* Note that this program produces temporal tapering of the wave packet
/* at the initial and final stages of the wave paddles' motion. However,
/* note that the input signal is windowed such that an isolated breaker
/* is generated in the basin. Hence, this aids in no multiple breaking
/* occuring.
/* Also 3 paddles on each side of the main paddles provide spatial
/* tapering for the breaking wave. The spatial tapering tapers to a set
/* value, tap.
/* Four data files are generated. The first one (2-D array) contains
/* the variations of the paddles motion (i.e. the input signal). Note
/* that no transfer function is being implemented in the analysis. The
/* second (1-D array) has the input signal only for the center paddle. The
/* third (2-D array) however has the unwindowed variation of the input
/* signal of the paddles motion. This third file is used for comparative
/* purposes to ensure that we are not truncating the actual input signal
/* to the paddles at too early a time. The fourth one (2-D array)
/* contains the temporal and spatial variation of the waveform as it
/* progresses in time down the basin.
/* The whole analysis was based on linear theory; however, it is evident
/* that the breaking wave analysis is quite nonlinear.
/* This program doesn't take into account the effects of reflection.
/* The paddles are treated as if they are stationary, i.e. the variations
/* in their positions is considered negligible; this is justified since
/* the stroke to wavelength ratio is about 0.1 or 10%.
/* Note: only 13 out of the 47 paddles are being used. The rest are idle.
/* Note appertaining .dat files for this ver: x*, x*a, x*b, x*c
/* Note that all info appertaining to data file x*c is suppressed here.
/*****************************************************************/
```

```
#include <stdio.h>
#include <math.h>

#define SR 0.04  /* i.e. sample rate is 25 Hz */

float eo[501],eo1[501],eo2[501],ph[33],om[33],am[33],am1[33],
    c[33], rk1[33], x[33],
    e[33][85], ej[251], eta[85][251], eost[48][501];
int info[5];

float sq(float value);

main()
{
 FILE *fptr1, *fptr2, *fptr3;
 char name1[70], name2[70], name3[70], name4[70];
 float tl,f,xb,tb,h,fc,fd,tap,pi,fs,tpi,dfd,om2,rko,rk;
 int ncom,i, j, k, a, b, t0;

 /* input required */
 printf("Enter breaking location, start time, water depth\n");
 scanf("%f %f %f", &xb,&tb,&h);
 printf("Enter center frequency, frequency range\n");
 scanf("%f %f", &fc, &fd);
 printf("\n\nEnter # of main paddles to be used (# < 6): ");
 scanf("%d", &a);
 printf("\n\nEnter starting paddle number (16<#<%d): ", 23-a);
 scanf("%d",&b);
 printf("\n\nPercent (e.g. 0.6 is 60%) to which side paddles are tapered: ");
 scanf("%f", &tap);
 printf("\n\nEnter filename1: ");
 scanf("%s",name1);
 if ((fptr1=fopen(name1,"w")) == NULL)
 {
  printf("Can't open file!\n");
  exit(1);
 }
 printf("\n\nEnter filename2: ");
 scanf("%s", name2);
 if ((fptr2=fopen(name2,"w")) == NULL)
 {
  printf("Can't open file!\n");
  exit(1);
 }
 printf("\n\nEnter filename3: ");
```

```
  scanf("%s",name3);
  if ((fptr3=fopen(name3,"w")) == NULL)
  {
   printf("Can't open file!\n");
   exit(1);
  }
/*  printf("\n\nEnter filename4: ");
  scanf("%s",name4);
  if ((fptr4=fopen(name4,"w")) == NULL)
  {
   printf("Can't open file!\n");
   exit(1);
  }*/

  fprintf(fptr1,"Alpha \n");
  fprintf(fptr3,"Alpha \n");
  info[0]=501;  /* number of data points */
  info[1]= (int) (1.0/SR+0.1);
  info[2]=0;
  info[3]=0;
  info[4]=0;
  for (i=0;i<5;i++)
  {
   fprintf(fptr1, "%d ", info[i]);
   fprintf(fptr3, "%d ", info[i]);
  }
  fprintf(fptr1,"\n");
  fprintf(fptr3,"\n");

  /* calculating the various important parameters in wave mechanics */
  fs=fc-fd/2.0;
  pi=4*atan(1);
  ncom=32;
  tpi=2*pi;
  dfd=fd/(ncom-1);
  for (i=1;i<(ncom+1);i++)
  {
   f=fs+(i-1)*dfd;
   om2=tpi*tpi*(f*f);
   rko=tpi*(f*f)/1.56;
   rk=om2/(9.81*tanh(rko*h));
   while((fabs(rk/rko-1)>=0.001))
   {
    rko=rk;
    rk=om2/(9.81*tanh(rko*h));
```

```
  }
  rk1[i] = rk;
  om[i]=tpi*f;
  c[i] = om[i]/rk1[i];
  ph[i]=-om[i]*tb+rk*xb;
  /* waves in wave train are of constant steepness of 0.1 */
  am[i]=(0.1/rk)*(sinh(2*rk*h)+2*rk*h)/(4*sq(sinh(rk*h)));
  am1[i] = (0.1/rk);
 }

 /* calculating the paddle motion and surface elevation at the paddle
    variations with time */
 for (j=0;j<501;j++)
 {
  eo[j]=0; eo1[j]=0; /* not nec. */
  tl= SR*(j);
  for (i=1;i<(ncom+1);i++)
  {
   eo[j]=eo[j]+am[i]*cos(-1*om[i]*tl-ph[i]);
   eo1[j]=eo1[j]+am1[i]*cos(-1*om[i]*tl-ph[i]);
  }
 }

 /* stepping through 251 time frames (i.e. 10 seconds)
     and through the whole 8.4m basin */
/*  for (j = 0; j<251; j++)
 {
  for (i=1;i<(ncom+1);i++)
   x[i] = c[i]*(j*SR)\;
  for (k=0; k<85; k++)  * k is distance in tens of cm *
  {
   for (i=1;i<(ncom+1);i++)
   {
       if (x[i] > (k*0.1))
       {
        t0 = (int)(((k*0.1)/c[i])/SR);  * dimensionless time *
        if (j<100)
          e[i][k] = am1[i]*cos(rk1[i]*(k*0.1-xb)-om[i]*(j*SR-tb))*
                          (1-sq(cos((j-t0)*pi/200)));
        else if ((j>=100) && (k*0.1)>(c[i]*(j-100)*SR))
          e[i][k] = am1[i]*cos(rk1[i]*(k*0.1-xb)-om[i]*(j*SR-tb))*
                          (1-sq(cos((j-t0)*pi/200)));
        else if ((j>=400) && (k*0.1)<(c[i]*(j-400)*SR)) *wrong, but uneff since j<250 *
          e[i][k] = am1[i]*cos(rk1[i]*(k*0.1-xb)-om[i]*(j*SR-tb))*
                          (1-sq(cos((500-j)*pi/200)));
```

```
        else
          e[i][k] = am1[i]*cos(rk1[i]*(k*0.1-xb)-om[i]*(j*SR-tb));
       }
       else
        e[i][k] = 0.0;
       ej[k] = ej[k] + e[i][k];
   }
   eta[k][j] = ej[k];
   ej[k] = 0.0;
  }
}*/

for(j=0;j<501;j++) /* equating eo2 to eo for later use in the third file */
  eo2[j] = eo[j];

/* incorporating temporal tapering effects for the first two data files */
for(j=0;j<501;j++)
{
 if (j<=100)
 {
  eo[j]=eo[j]*(1-sq(cos((j)*pi/200)));
  eo1[j] = eo1[j]*(1-sq(cos((j)*pi/200)));
 }
 /*arbitrary cutoff of input signal i.s. based on plot of unwindowed i.s.*/
 if ( (j>=((tb+0)-4)*25) && (j<=((tb+0)*25)) )
 {
  eo[j]=eo[j]*(1-sq(cos((((int)(tb)+0)*25-j)*pi/200)));
  eo1[j]=eo1[j]*(1-sq(cos((((int)(tb)+0)*25-j)*pi/200)));
 }
 if ( (j>(tb+0)*25) && (j<=500) )
 {
  eo[j] = 0.0;
  eo1[j] = 0.0;
 }
}

/* incorporating temporal tapering effects for the third data file */
/* the third data file is the unwindowed input signal at the center paddle*/
for(j=0;j<501;j++)
{
 if (j<=100)
   eo2[j]=eo2[j]*(1-sq(cos((j)*pi/200)));
 if (j>=400)
   eo2[j]=eo2[j]*(1-sq(cos((500-j)*pi/200)));
}
```

```
/* incorporating spatial tapering effects for the third data file */
for(j=0;j<501;j++)
{
 for(i=b+1;i<b+a-1;i++) /* for main paddles */
   eost[i][j] = eo2[j];
 for(i=13;i<b-4;i++)  /* for side paddles */
   eost[i][j] = eo2[j]*tap;
 for(i=b+a+4;i<26;i++)  /* for side paddles */
   eost[i][j] = eo2[j]*tap;
 for(i=b-4;i<b+1;i++) /* for 3 (really 5) side paddles on each side */
 {
   eost[i][j] = eo2[j]*(1-(1-tap)*sq(cos((4-(b-i))*pi/8)));
   eost[b+a+(b-i-1)][j] = eost[i][j];
 }
 for(i=1;i<13;i++)  /* for unused paddles */
   eost[i][j] = 0.0;
 for(i=26;i<48;i++) /* for unused paddles */
   eost[i][j] = 0.0;
}
/* writing to third data file only */
for (j=0;j<501;j++)
{
 for (i=1;i<48;i++)
   fprintf(fptr3, "%.8f ", eost[i][j]);
 fprintf(fptr3, "\n");
}
fclose(fptr3);

/* incorporating spatial tapering effects for the first data file */
for(j=0;j<501;j++)
{
 for(i=b+1;i<b+a-1;i++) /* for main paddles */
   eost[i][j] = eo[j];
 for(i=13;i<b-4;i++)  /* for side paddles */
   eost[i][j] = eo[j]*tap;
 for(i=b+a+4;i<26;i++)  /* for side paddles */
   eost[i][j] = eo[j]*tap;
 for(i=b-4;i<b+1;i++) /* for 3 (really 5) side paddles on each side */
 {
   eost[i][j] = eo[j]*(1-(1-tap)*sq(cos((4-(b-i))*pi/8)));
   eost[b+a+(b-i-1)][j] = eost[i][j];
 }
 for(i=1;i<13;i++)  /* for unused paddles */
   eost[i][j] = 0.0;
 for(i=26;i<48;i++) /* for unused paddles */
```

```
    eost[i][j] = 0.0;
  }

  /* writing to the data files */
  for (j=0;j<501;j++)
  {
   for (i=1;i<48;i++)
     fprintf(fptr1, "%.8f ", eost[i][j]);
   fprintf(fptr1, "\n");
  }
  fclose(fptr1);
  for (i=0;i<501;i++)
   fprintf(fptr2, "%.8f \n", eo[i]);
  fclose(fptr2);
/*  for (k=0; k<85; k++)
  {
   for (j=0; j<251; j++)
     fprintf(fptr4, "%.8f ", eta[k][j]);
   fprintf(fptr4, "\n");
  }
  fclose(fptr4);*/
} /* end main */

float sq(float value)
 {
  float ans;
  ans=value*value;
  return ans;
 }
```

```
/*****************************************************************/
/* Variables:
/* eo[501] = Xi(t), all paddle motion variation with time. Xi = 0.5*stroke
/* eo1[501] = eta(0,t), surface elev. variation with time at center paddle
/* eo2[501] = eo[501] without any temporal tapering (see intro)
/* ph[33] = phase, phi, of the wave
/* om[33] = radian frequency, w, of the wave
/* am[33] = amplitude of Xi of a single frequency
/* am1[33] = amplitude of eta of a single frequency
/* c[33] = phase speed of a particular frequency
/* rk1[33] = wavenumber of a particular frequency
/* x[33] = distance a wave of a certain freq. has propagated over time t
/* e[33][85] = surf. elev. for a particular frequency and time
/* ej[250] = surface elevation eta(x,t) for a particular time t
/* eta[85][251] = surface elevation eta(x,t)
/* eost [48][501] = eo[501] for all the 47 paddles
/* info = a 1-D array needed for wave generation program
/* fptr and name = for data files
/* tl = elapsed time
/* f = frequency
/* xb = location of breaking
/* tb = time to breaking
/* h = water depth
/* fc = center frequency
/* fd = frequency range
/* tap = percentage to which side paddles are tapered
/* pi = 3.14...
/* fs = smallest frequency
/* tpi = 2*pi
/* dfd = constant difference between two consecutive frequencies
/* om2 = square of radian frequency
/* rko = coresspondiong deep-water wavelength
/* rk = wavenumber of a particular frequency
/* ncom = number of components (different frequencies) in wave packet
/* a = number of main paddles being used (<6)
/* b = starting paddle number (16<#<23-a)
/* t0 = dimensionless time parameter used to account for tempor. tapering
/*****************************************************************/
```

APPENDIX 2

Wave Amplitude Attenuation due to Channel Walls

The following analysis is applicable to a time periodic train of small amplitude (Hunt, 1952). It is applied here to the central characteristic values.

d = depth = 0.6m
b = basin section width = 4.0m
a = wave amplitude
υ = viscosity = 1.0×10^{-6} m^2/s
k = wavenumber
ω = radian wave frequency
y is the longitudinal direction.

The decay of the wave amplitude is given by:

$$-\frac{1}{a}\frac{\partial a}{\partial y} = B \quad \text{(for laminar boundary layers)} \qquad \text{(A2.1)}$$

where,

$$B = \frac{2k}{b}\frac{\sqrt{v}}{\sqrt{2\omega}}\frac{(kb + \sinh 2kd)}{(2kd + \sinh 2kd)}$$

Integrating equation (A2.1) with respect to y:

$$-By + \alpha = -\ln a + \beta$$
$$\alpha' e^{-By} = \beta' a$$
$$a = \alpha'' e^{-By}$$
$$a^2/a_o^2 = e^{-2By} \qquad \text{(A2.2)}$$

From (A2.1): $B = 7.0 \times 10^{-4}/m$ for $f_c = 1.08Hz$
$\Rightarrow a^2/a_o^2 = \exp(-2 \times 7.0 \times 10^{-4} y)$

for y = 4m: $a^2/a_o^2 = 99.4\%$

So, the percentage loss in wave energy due to viscous dissipation is 0.6%.
Therefore, viscous dissipation losses can be neglected for this experiment.

APPENDIX 3

Equivalent Characteristic Wave Steepness (2D - 3D)

As described in section 3.4.3, an equivalent characteristic wave steepness, ak_{c2}, is introduced in order to make meaningful comparison between this study and that done by RM. Using the ak_c value directly is not correct since the leakage attenuates the wave amplitude in the 3-D case in the basin, but no leakage occurred in the flume. The new parameter, ak_{c2}, is computed in the following way:

$$\frac{ak_{c2x}}{l_x} = \frac{ak_{ct}}{l_t}$$

where,

x stands for either P, S, or I

ak_{c2x} is the equivalent characteristic wave steepness

ak_{ct} is the ak_c obtained in the basin for the 2D plunger ($ak_{ct} = 0.42$)

l_x is the maximum wave height at a given location in the basin
(wave gauge 1 at y = 0 is chosen)

l_t is the maximum wave height for wave gauge 1 at y = 0, ($l_t = 11.7$cm).

This equation holds since for this equivalent two-dimensional analysis (no leakage), an increase in the stroke of the paddles produces a linear increase in the amplitudes being recorded. However, using the centerline location of y = 0 will tend to produce ak_{c2} values that are overestimated since more leakage occurs between the location y = 0 and breaking in the 3-D case. Figure A3.1 shows the time series $\eta(t)$ for those 4 records. The results are presented in table A3.1.

Table A3.1 Equivalent 2D Characteristic Wave Steepness Values

Breaker Type	ak_c	l (cm)	ak_{c2}
Plunger	0.45	10.2	0.37
Spiller	0.32	7.1	0.25
Incipient	0.29	6.5	0.23

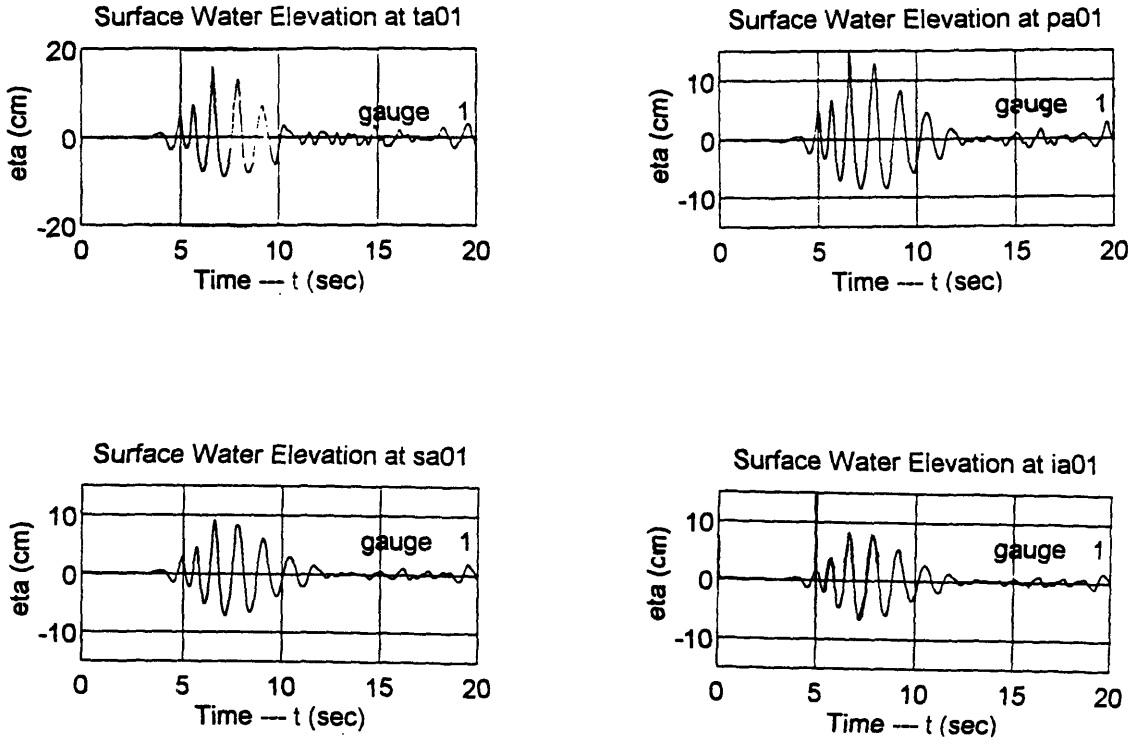

Figure A3.1 Time series $\eta(t)$: 2D plunger, plunger, spiller, and incipient at x = 0, y = 0. l_t = 11.7cm, l_p = 10.2cm, l_s = 7.1cm, and l_i = 6.5cm.

APPENDIX 4

SPECTRA PLOTS FOR PLUNGER AND INCIPIENT

Figures A4.1 - A4.11 Spectra for plunger for the entire control volume (y = 0, 20, ... 200cm)

Figures A4.12 - A4.22 Spectra for incipient for the entire control volume (y = 0, 20, ... 200cm)

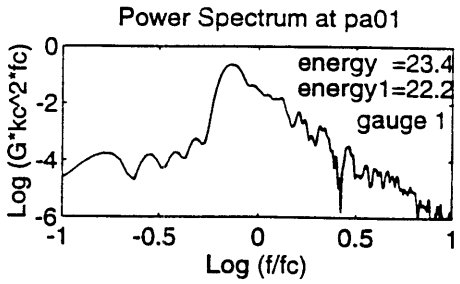
Power Spectrum at pa01
energy =23.4
energy1=22.2
gauge 1
Log (G*kc^2*fc)
Log (f/fc)

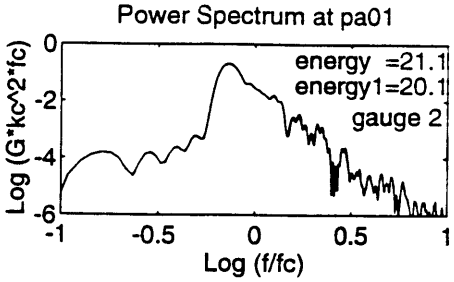
Power Spectrum at pa01
energy =21.1
energy1=20.1
gauge 2
Log (G*kc^2*fc)
Log (f/fc)

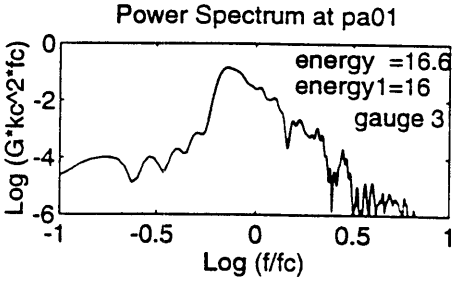
Power Spectrum at pa01
energy =16.6
energy1=16
gauge 3
Log (G*kc^2*fc)
Log (f/fc)

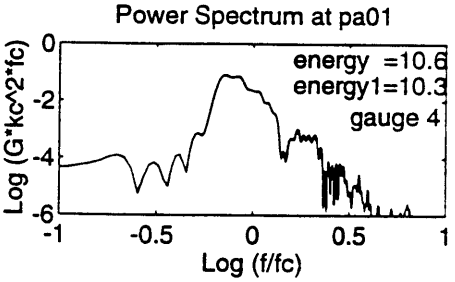
Power Spectrum at pa01
energy =10.6
energy1=10.3
gauge 4
Log (G*kc^2*fc)
Log (f/fc)

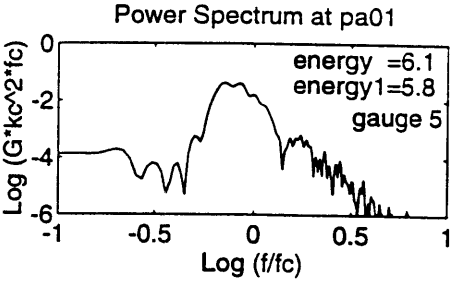
Power Spectrum at pa01
energy =6.1
energy1=5.8
gauge 5
Log (G*kc^2*fc)
Log (f/fc)

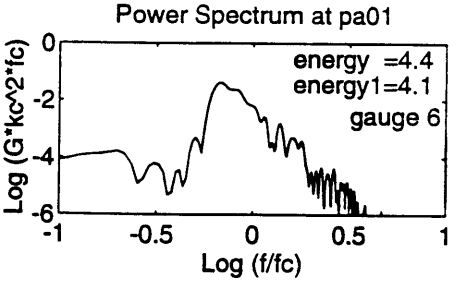
Power Spectrum at pa01
energy =4.4
energy1=4.1
gauge 6
Log (G*kc^2*fc)
Log (f/fc)

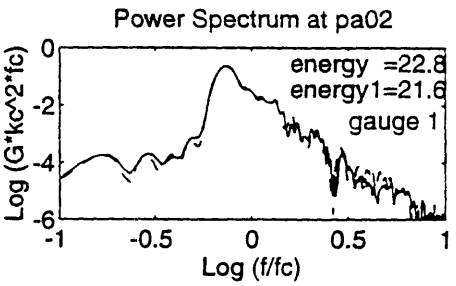
Power Spectrum at pa02
energy =22.8
energy1=21.6
gauge 1
Log (G*kc^2*fc)
Log (f/fc)

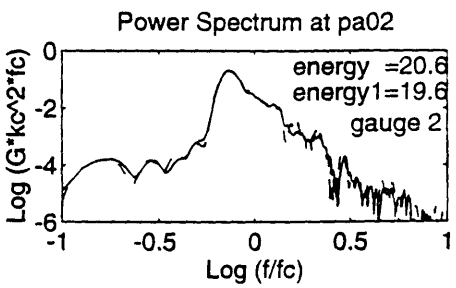
Power Spectrum at pa02
energy =20.6
energy1=19.6
gauge 2
Log (G*kc^2*fc)
Log (f/fc)

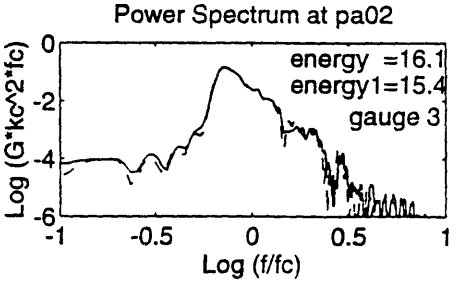
Power Spectrum at pa02
energy =16.1
energy1=15.4
gauge 3
Log (G*kc^2*fc)
Log (f/fc)

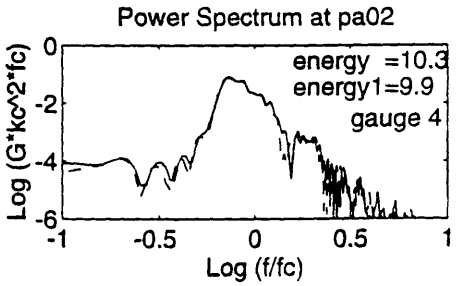
Power Spectrum at pa02
energy =10.3
energy1=9.9
gauge 4
Log (G*kc^2*fc)
Log (f/fc)

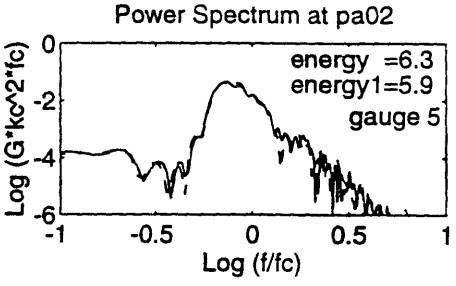
Power Spectrum at pa02
energy =6.3
energy1=5.9
gauge 5
Log (G*kc^2*fc)
Log (f/fc)

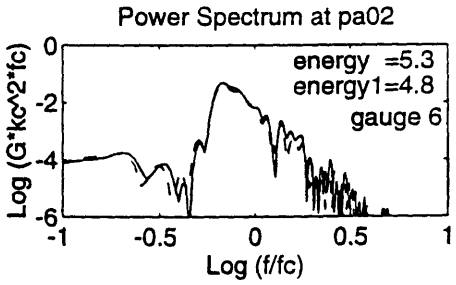
Power Spectrum at pa02
energy =5.3
energy1=4.8
gauge 6
Log (G*kc^2*fc)
Log (f/fc)

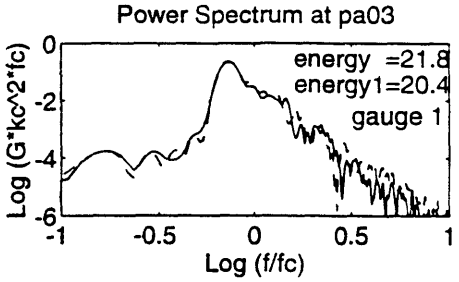
Power Spectrum at pa03
energy =21.8
energy1=20.4
gauge 1
Log (G*kc^2*fc)
Log (f/fc)

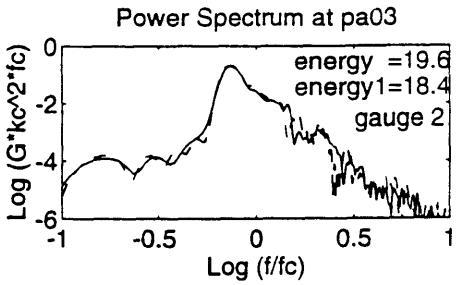
Power Spectrum at pa03
energy =19.6
energy1=18.4
gauge 2
Log (G*kc^2*fc)
Log (f/fc)

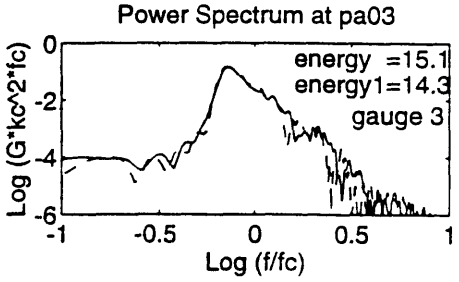
Power Spectrum at pa03
energy =15.1
energy1=14.3
gauge 3
Log (G*kc^2*fc)
Log (f/fc)

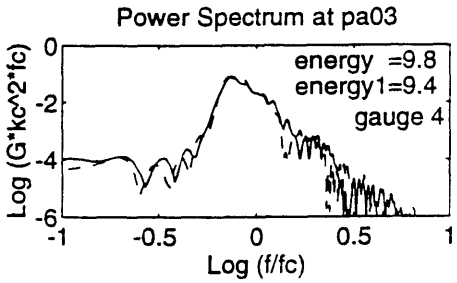
Power Spectrum at pa03
energy =9.8
energy1=9.4
gauge 4
Log (G*kc^2*fc)
Log (f/fc)

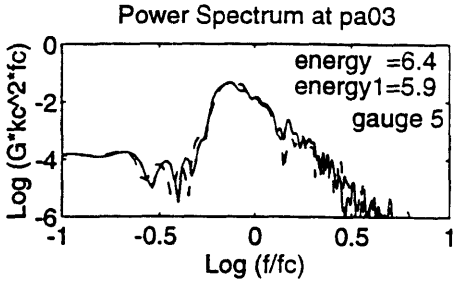
Power Spectrum at pa03
energy =6.4
energy1=5.9
gauge 5
Log (G*kc^2*fc)
Log (f/fc)

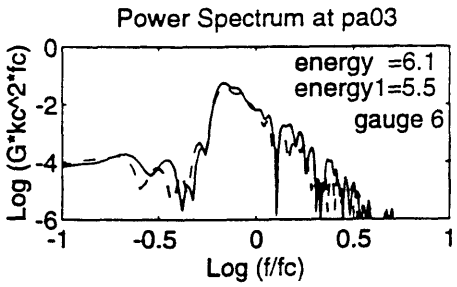
Power Spectrum at pa03
energy =6.1
energy1=5.5
gauge 6
Log (G*kc^2*fc)
Log (f/fc)

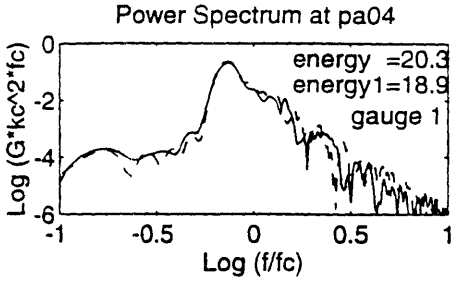
Power Spectrum at pa04
energy =20.3
energy1=18.9
gauge 1
Log (G*kc^2*fc)
Log (f/fc)

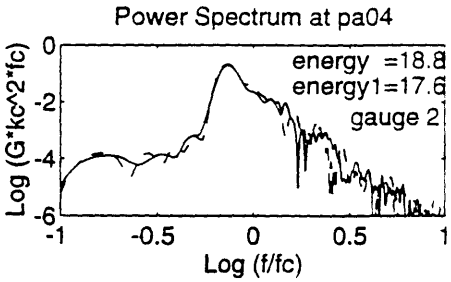
Power Spectrum at pa04
energy =18.8
energy1=17.6
gauge 2
Log (G*kc^2*fc)
Log (f/fc)

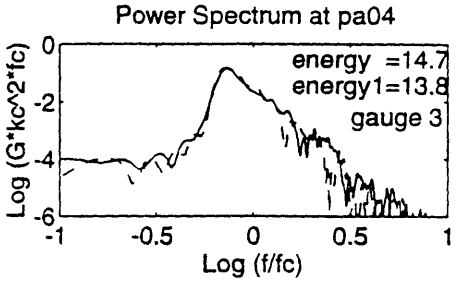
Power Spectrum at pa04
energy =14.7
energy1=13.8
gauge 3
Log (G*kc^2*fc)
Log (f/fc)

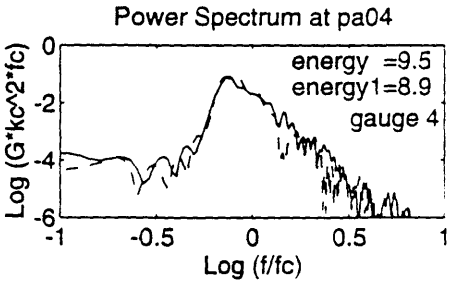
Power Spectrum at pa04
energy =9.5
energy1=8.9
gauge 4
Log (G*kc^2*fc)
Log (f/fc)

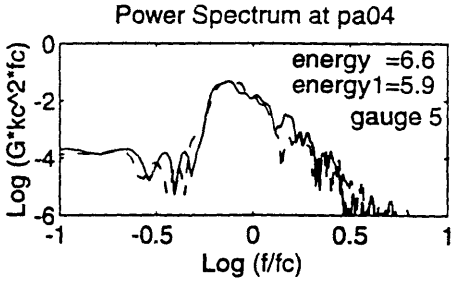
Power Spectrum at pa04
energy =6.6
energy1=5.9
gauge 5
Log (G*kc^2*fc)
Log (f/fc)

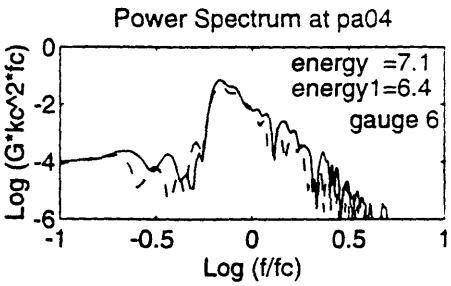
Power Spectrum at pa04
energy =7.1
energy1=6.4
gauge 6
Log (G*kc^2*fc)
Log (f/fc)

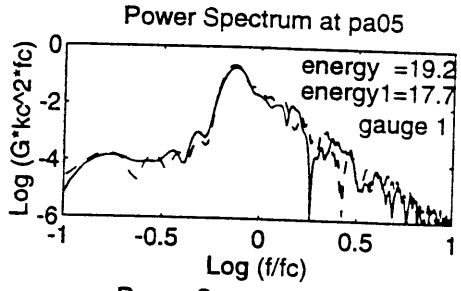
Power Spectrum at pa05
energy =19.2
energy1=17.7
gauge 1
Log (G*kc^2*fc)
Log (f/fc)

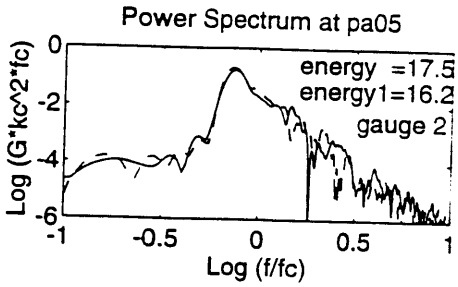
Power Spectrum at pa05
energy =17.5
energy1=16.2
gauge 2
Log (G*kc^2*fc)
Log (f/fc)

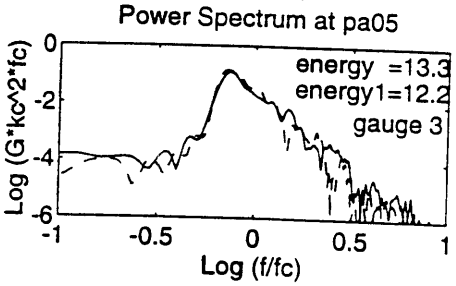
Power Spectrum at pa05
energy =13.3
energy1=12.2
gauge 3
Log (G*kc^2*fc)
Log (f/fc)

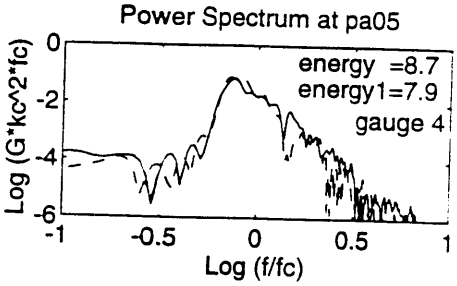
Power Spectrum at pa05
energy =8.7
energy1=7.9
gauge 4
Log (G*kc^2*fc)
Log (f/fc)

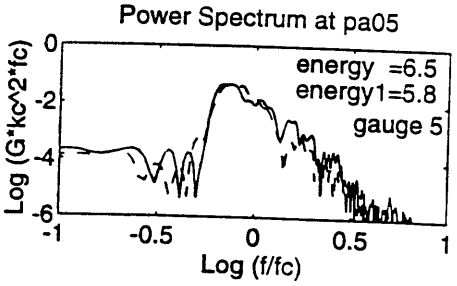
Power Spectrum at pa05
energy =6.5
energy1=5.8
gauge 5
Log (G*kc^2*fc)
Log (f/fc)

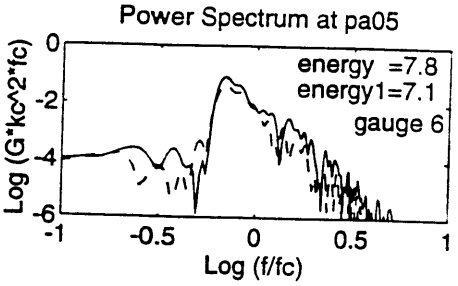
Power Spectrum at pa05
energy =7.8
energy1=7.1
gauge 6
Log (G*kc^2*fc)
Log (f/fc)

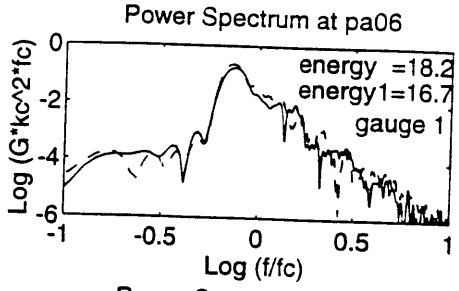
Power Spectrum at pa06
energy =18.2
energy1=16.7
gauge 1
Log (G*kc^2*fc)
Log (f/fc)

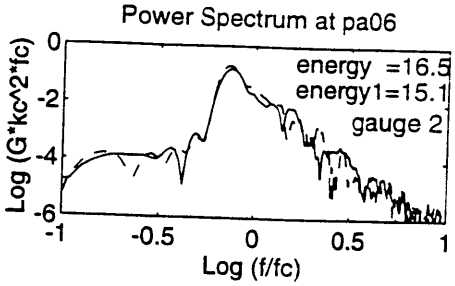
Power Spectrum at pa06
energy =16.5
energy1=15.1
gauge 2
Log (G*kc^2*fc)
Log (f/fc)

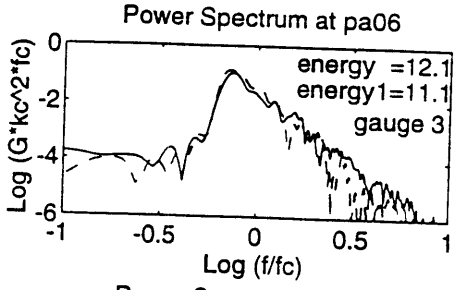
Power Spectrum at pa06
energy =12.1
energy1=11.1
gauge 3
Log (G*kc^2*fc)
Log (f/fc)

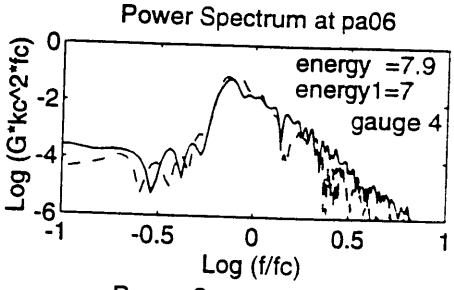
Power Spectrum at pa06
energy =7.9
energy1=7
gauge 4
Log (G*kc^2*fc)
Log (f/fc)

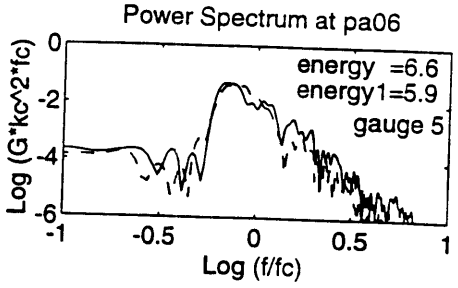
Power Spectrum at pa06
energy =6.6
energy1=5.9
gauge 5
Log (G*kc^2*fc)
Log (f/fc)

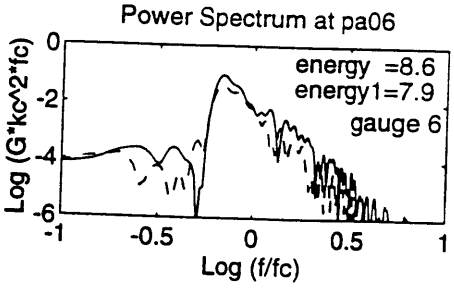
Power Spectrum at pa06
energy =8.6
energy1=7.9
gauge 6
Log (G*kc^2*fc)
Log (f/fc)

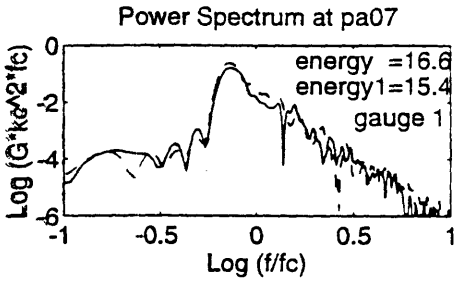
Power Spectrum at pa07
energy =16.6
energy1=15.4
gauge 1
Log (G*kc^2*fc)
Log (f/fc)

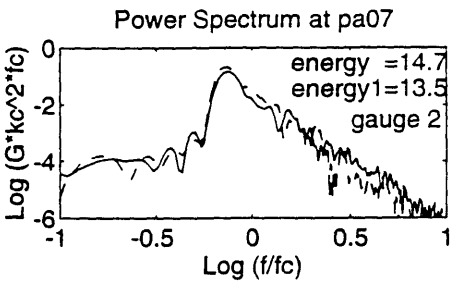
Power Spectrum at pa07
energy =14.7
energy1=13.5
gauge 2
Log (G*kc^2*fc)
Log (f/fc)

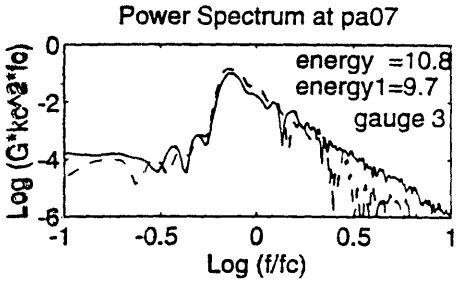
Power Spectrum at pa07
energy =10.8
energy1=9.7
gauge 3
Log (G*kc^2*fc)
Log (f/fc)

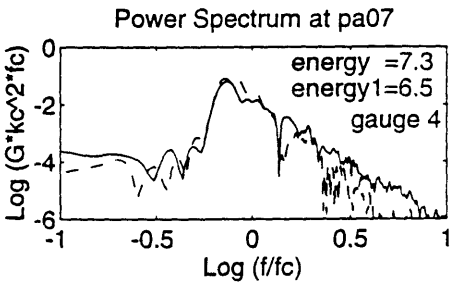
Power Spectrum at pa07
energy =7.3
energy1=6.5
gauge 4
Log (G*kc^2*fc)
Log (f/fc)

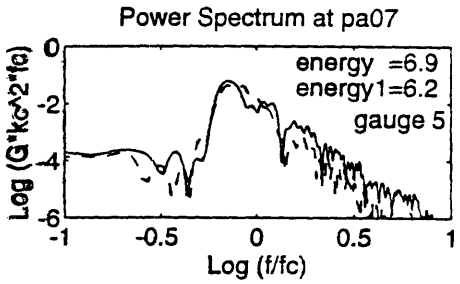
Power Spectrum at pa07
energy =6.9
energy1=6.2
gauge 5
Log (G*kc^2*fc)
Log (f/fc)

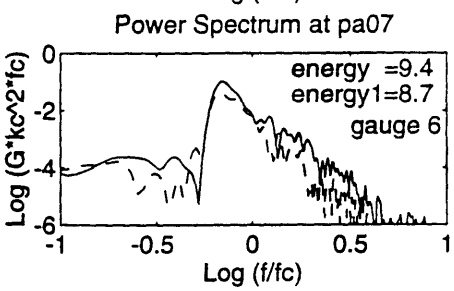
Power Spectrum at pa07
energy =9.4
energy1=8.7
gauge 6
Log (G*kc^2*fc)
Log (f/fc)

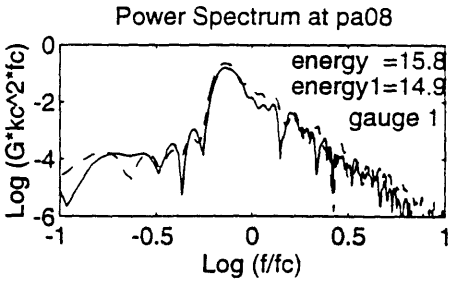
Power Spectrum at pa08
energy =15.8
energy1=14.9
gauge 1
Log (G*kc^2*fc)
Log (f/fc)

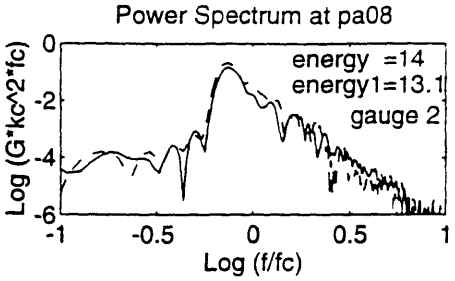
Power Spectrum at pa08
energy =14
energy1=13.1
gauge 2
Log (G*kc^2*fc)
Log (f/fc)

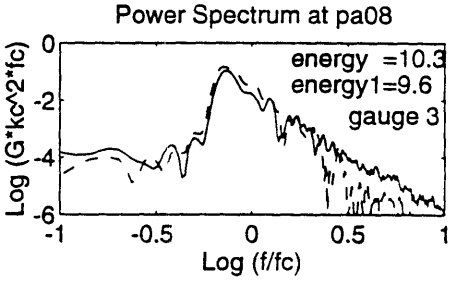
Power Spectrum at pa08
energy =10.3
energy1=9.6
gauge 3
Log (G*kc^2*fc)
Log (f/fc)

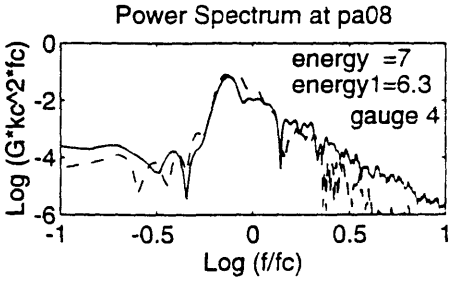
Power Spectrum at pa08
energy =7
energy1=6.3
gauge 4
Log (G*kc^2*fc)
Log (f/fc)

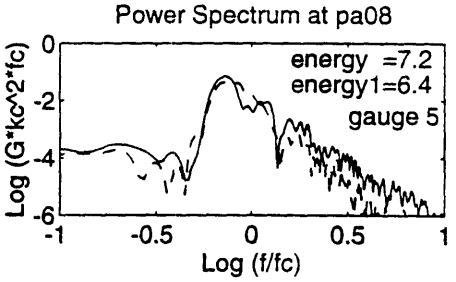
Power Spectrum at pa08
energy =7.2
energy1=6.4
gauge 5
Log (G*kc^2*fc)
Log (f/fc)

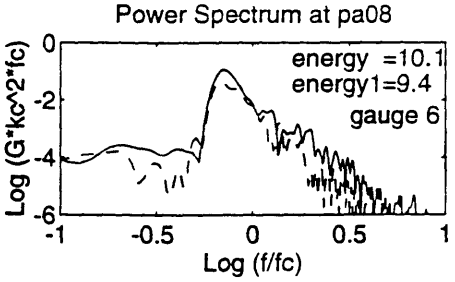
Power Spectrum at pa08
energy =10.1
energy1=9.4
gauge 6
Log (G*kc^2*fc)
Log (f/fc)

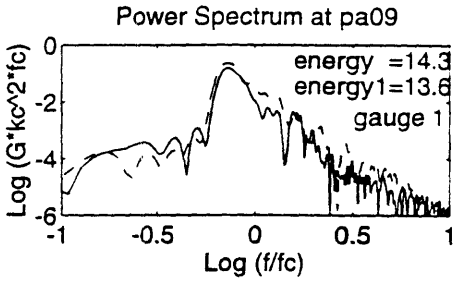
Power Spectrum at pa09
energy =14.3
energy1=13.6
gauge 1
Log (G*kc^2*fc)
Log (f/fc)

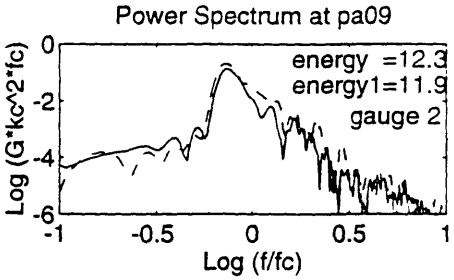
Power Spectrum at pa09
energy =12.3
energy1=11.9
gauge 2
Log (G*kc^2*fc)
Log (f/fc)

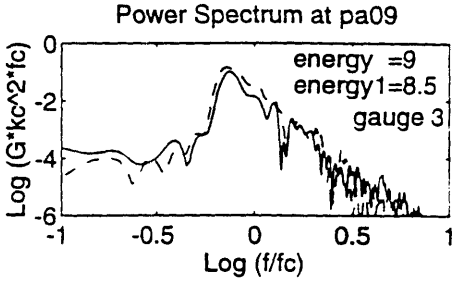
Power Spectrum at pa09
energy =9
energy1=8.5
gauge 3
Log (G*kc^2*fc)
Log (f/fc)

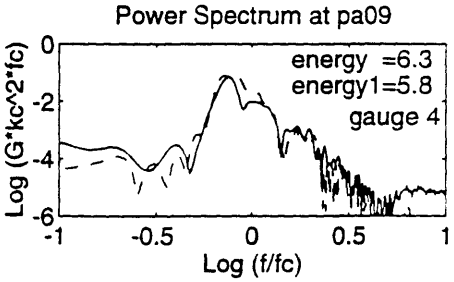
Power Spectrum at pa09
energy =6.3
energy1=5.8
gauge 4
Log (G*kc^2*fc)
Log (f/fc)

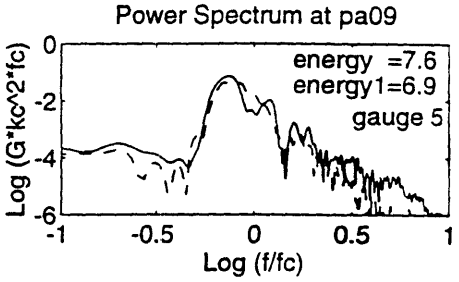
Power Spectrum at pa09
energy =7.6
energy1=6.9
gauge 5
Log (G*kc^2*fc)
Log (f/fc)

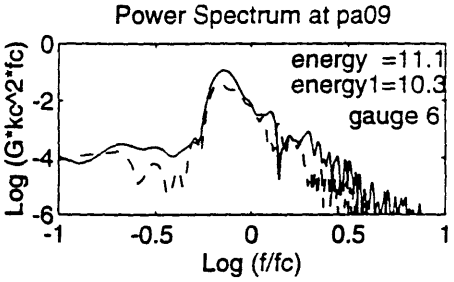
Power Spectrum at pa09
energy =11.1
energy1=10.3
gauge 6
Log (G*kc^2*fc)
Log (f/fc)

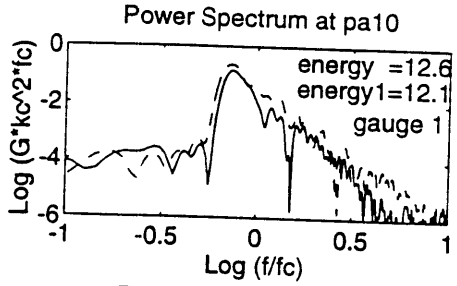
Power Spectrum at pa10
energy =12.6
energy1=12.1
gauge 1
Log (G*kc^2*fc)
Log (f/fc)

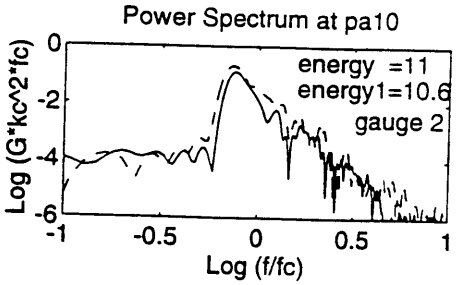
Power Spectrum at pa10
energy =11
energy1=10.6
gauge 2
Log (G*kc^2*fc)
Log (f/fc)

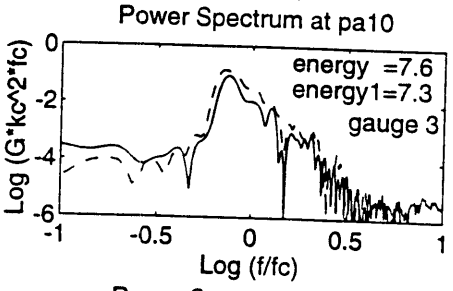
Power Spectrum at pa10
energy =7.6
energy1=7.3
gauge 3
Log (G*kc^2*fc)
Log (f/fc)

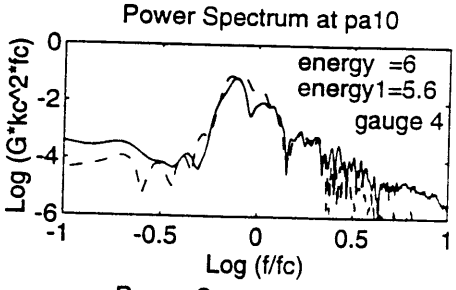
Power Spectrum at pa10
energy =6
energy1=5.6
gauge 4
Log (G*kc^2*fc)
Log (f/fc)

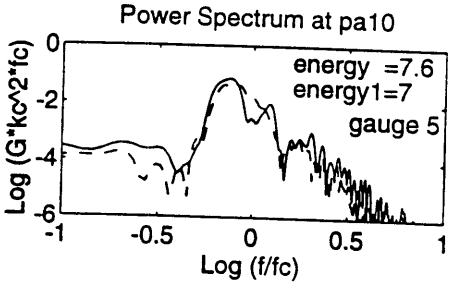
Power Spectrum at pa10
energy =7.6
energy1=7
gauge 5
Log (G*kc^2*fc)
Log (f/fc)

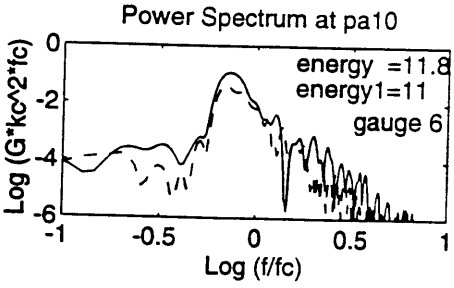
Power Spectrum at pa10
energy =11.8
energy1=11
gauge 6
Log (G*kc^2*fc)
Log (f/fc)

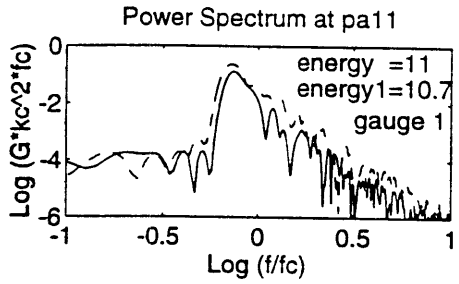
Power Spectrum at pa11
energy =11
energy1=10.7
gauge 1
Log (G*kc^2*fc)
Log (f/fc)

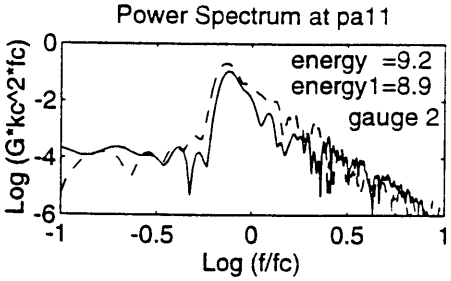
Power Spectrum at pa11
energy =9.2
energy1=8.9
gauge 2
Log (G*kc^2*fc)
Log (f/fc)

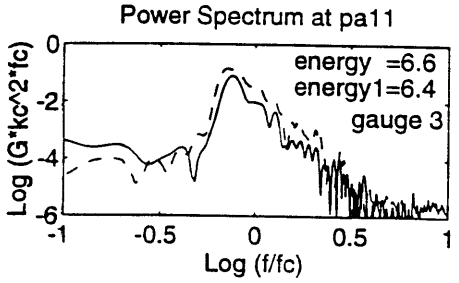
Power Spectrum at pa11
energy =6.6
energy1=6.4
gauge 3
Log (G*kc^2*fc)
Log (f/fc)

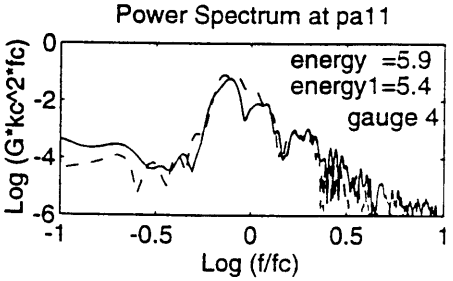
Power Spectrum at pa11
energy =5.9
energy1=5.4
gauge 4
Log (G*kc^2*fc)
Log (f/fc)

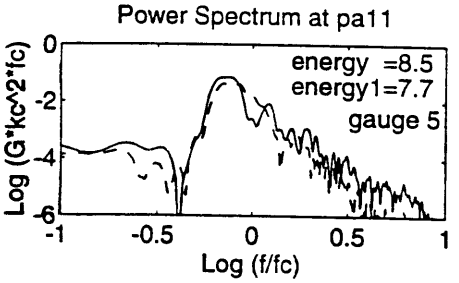
Power Spectrum at pa11
energy =8.5
energy1=7.7
gauge 5
Log (G*kc^2*fc)
Log (f/fc)

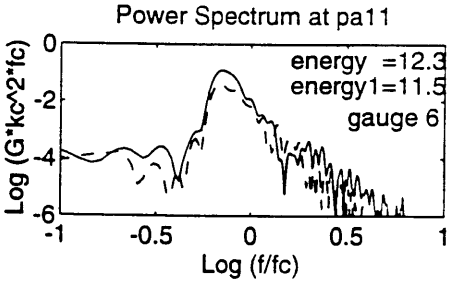
Power Spectrum at pa11
energy =12.3
energy1=11.5
gauge 6
Log (G*kc^2*fc)
Log (f/fc)

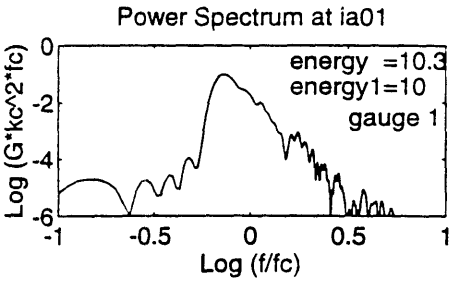
Power Spectrum at ia01
energy =10.3
energy1=10
gauge 1
Log (G*kc^2*fc)
Log (f/fc)

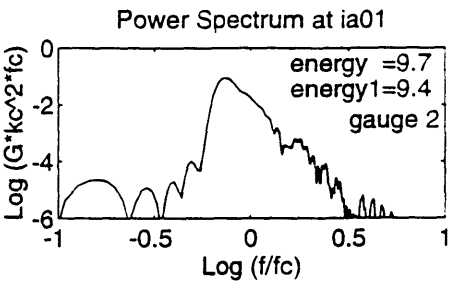
Power Spectrum at ia01
energy =9.7
energy1=9.4
gauge 2
Log (G*kc^2*fc)
Log (f/fc)

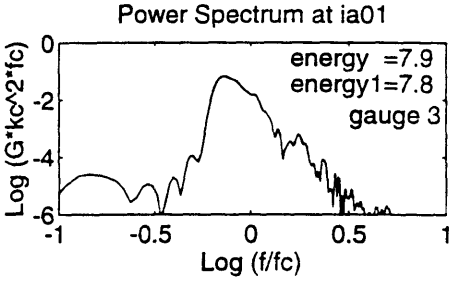
Power Spectrum at ia01
energy =7.9
energy1=7.8
gauge 3
Log (G*kc^2*fc)
Log (f/fc)

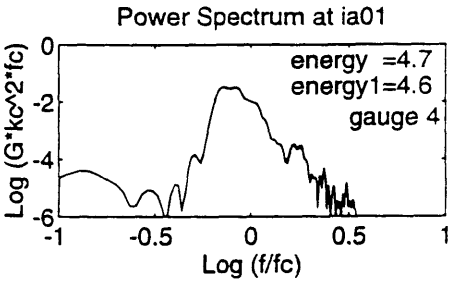
Power Spectrum at ia01
energy =4.7
energy1=4.6
gauge 4
Log (G*kc^2*fc)
Log (f/fc)

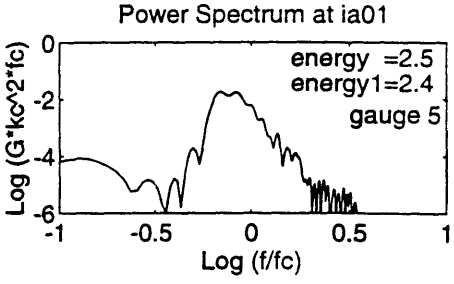
Power Spectrum at ia01
energy =2.5
energy1=2.4
gauge 5
Log (G*kc^2*fc)
Log (f/fc)

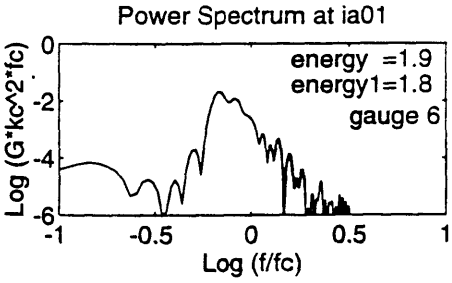
Power Spectrum at ia01
energy =1.9
energy1=1.8
gauge 6
Log (G*kc^2*fc)
Log (f/fc)

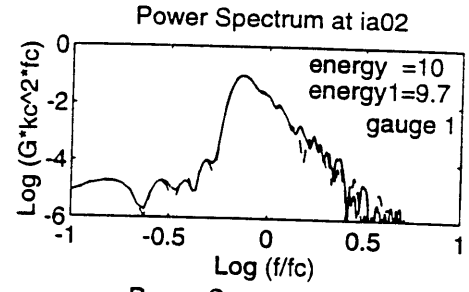
Power Spectrum at ia02
energy =10
energy1=9.7
gauge 1
Log (G*kc^2*fc)
Log (f/fc)

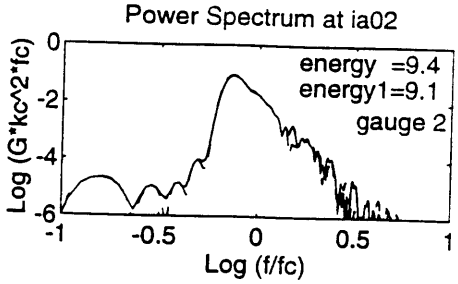
Power Spectrum at ia02
energy =9.4
energy1=9.1
gauge 2
Log (G*kc^2*fc)
Log (f/fc)

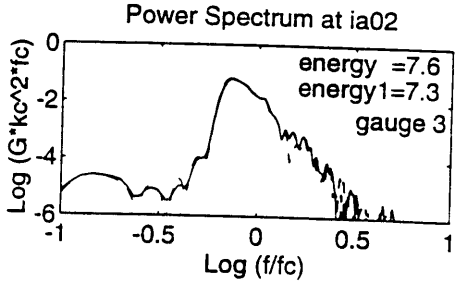
Power Spectrum at ia02
energy =7.6
energy1=7.3
gauge 3
Log (G*kc^2*fc)
Log (f/fc)

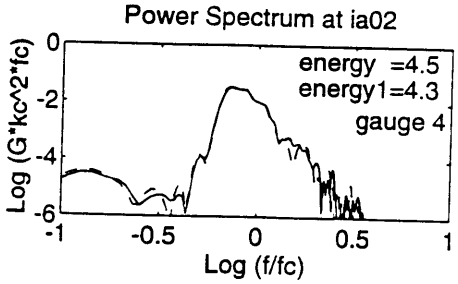
Power Spectrum at ia02
energy =4.5
energy1=4.3
gauge 4
Log (G*kc^2*fc)
Log (f/fc)

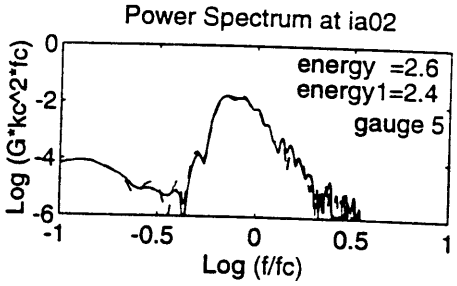
Power Spectrum at ia02
energy =2.6
energy1=2.4
gauge 5
Log (G*kc^2*fc)
Log (f/fc)

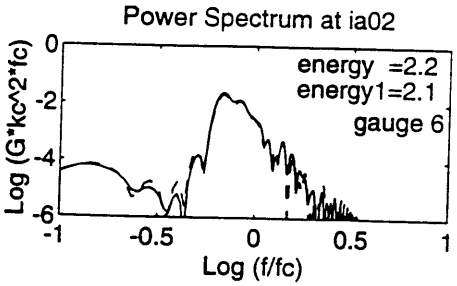
Power Spectrum at ia02
energy =2.2
energy1=2.1
gauge 6
Log (G*kc^2*fc)
Log (f/fc)

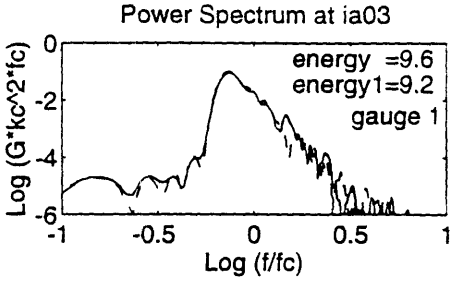
Power Spectrum at ia03
energy =9.6
energy1=9.2
gauge 1
Log (G*kc^2*fc)
Log (f/fc)

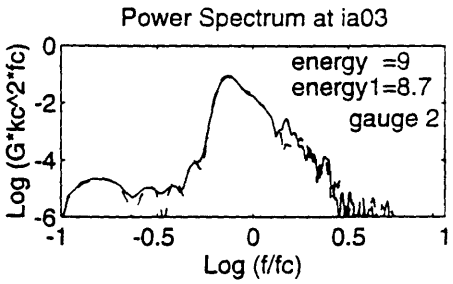
Power Spectrum at ia03
energy =9
energy1=8.7
gauge 2
Log (G*kc^2*fc)
Log (f/fc)

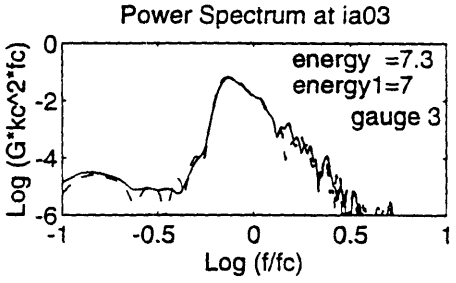
Power Spectrum at ia03
energy =7.3
energy1=7
gauge 3
Log (G*kc^2*fc)
Log (f/fc)

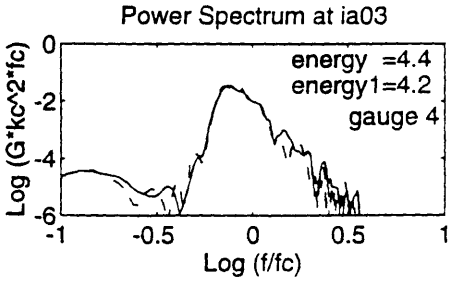
Power Spectrum at ia03
energy =4.4
energy1=4.2
gauge 4
Log (G*kc^2*fc)
Log (f/fc)

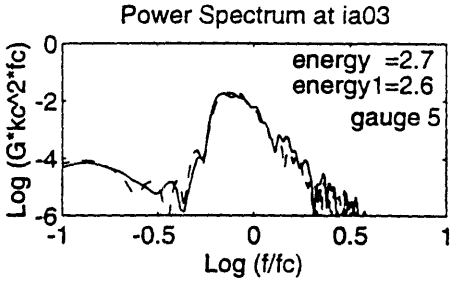
Power Spectrum at ia03
energy =2.7
energy1=2.6
gauge 5
Log (G*kc^2*fc)
Log (f/fc)

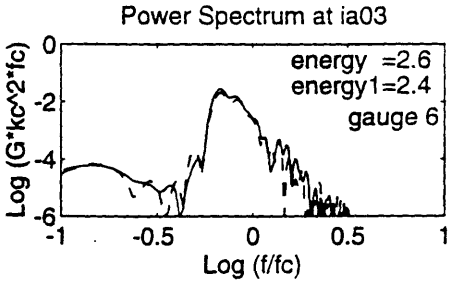
Power Spectrum at ia03
energy =2.6
energy1=2.4
gauge 6
Log (G*kc^2*fc)
Log (f/fc)

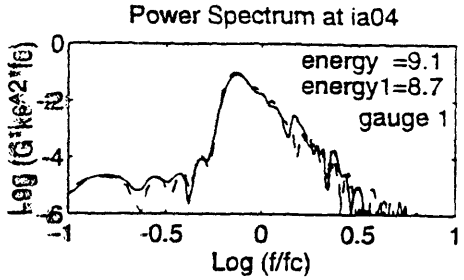
Power Spectrum at ia04
energy =9.1
energy1=8.7
gauge 1
Log (G*kc^2*fc)
Log (f/fc)

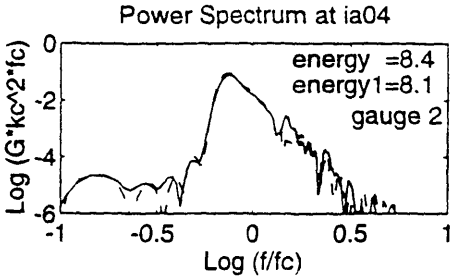
Power Spectrum at ia04
energy =8.4
energy1=8.1
gauge 2
Log (G*kc^2*fc)
Log (f/fc)

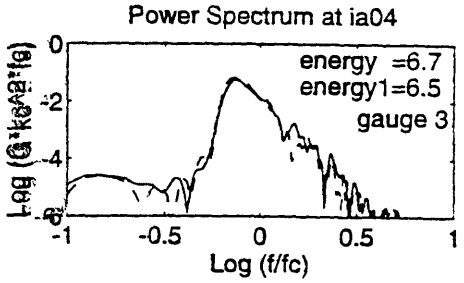
Power Spectrum at ia04
energy =6.7
energy1=6.5
gauge 3
Log (f/fc)

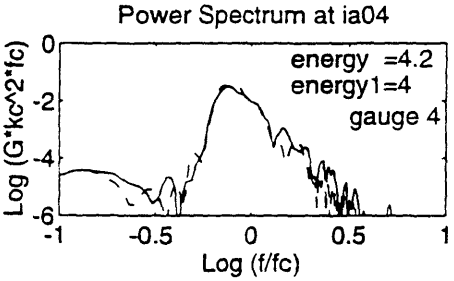
Power Spectrum at ia04
energy =4.2
energy1=4
gauge 4
Log (G*kc^2*fc)
Log (f/fc)

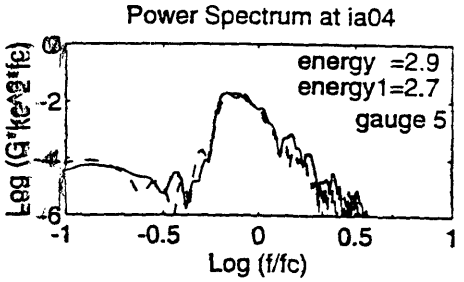
Power Spectrum at ia04
energy =2.9
energy1=2.7
gauge 5
Log (f/fc)

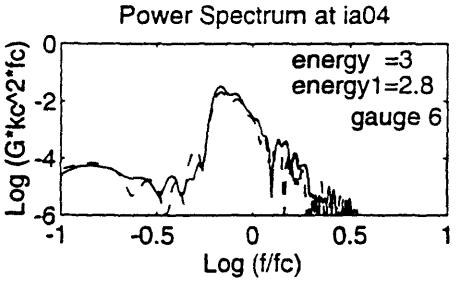
Power Spectrum at ia04
energy =3
energy1=2.8
gauge 6
Log (G*kc^2*fc)
Log (f/fc)

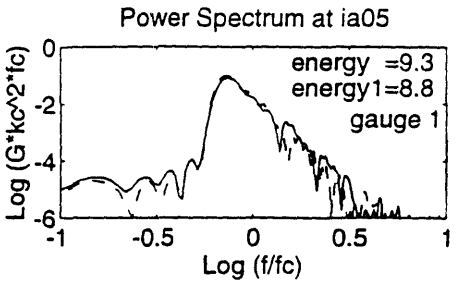
Power Spectrum at ia05
energy =9.3
energy1=8.8
gauge 1
Log (G*kc^2*fc)
Log (f/fc)

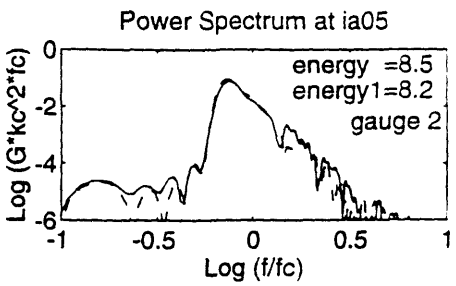
Power Spectrum at ia05
energy =8.5
energy1=8.2
gauge 2
Log (G*kc^2*fc)
Log (f/fc)

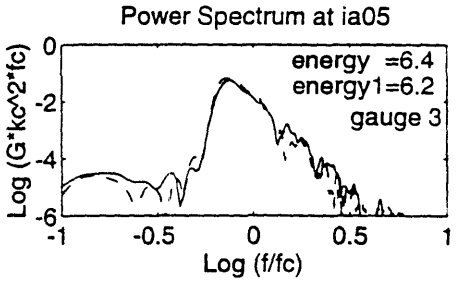
Power Spectrum at ia05
energy =6.4
energy1=6.2
gauge 3
Log (G*kc^2*fc)
Log (f/fc)

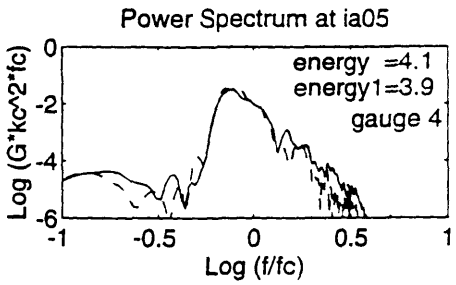
Power Spectrum at ia05
energy =4.1
energy1=3.9
gauge 4
Log (G*kc^2*fc)
Log (f/fc)

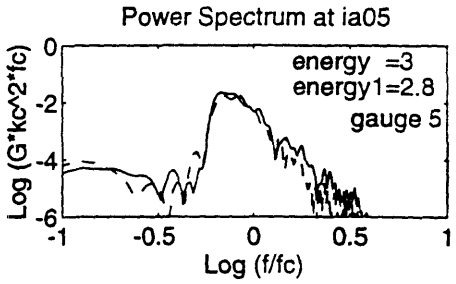
Power Spectrum at ia05
energy =3
energy1=2.8
gauge 5
Log (G*kc^2*fc)
Log (f/fc)

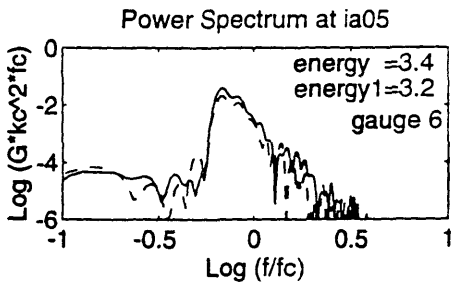
Power Spectrum at ia05
energy =3.4
energy1=3.2
gauge 6
Log (G*kc^2*fc)
Log (f/fc)

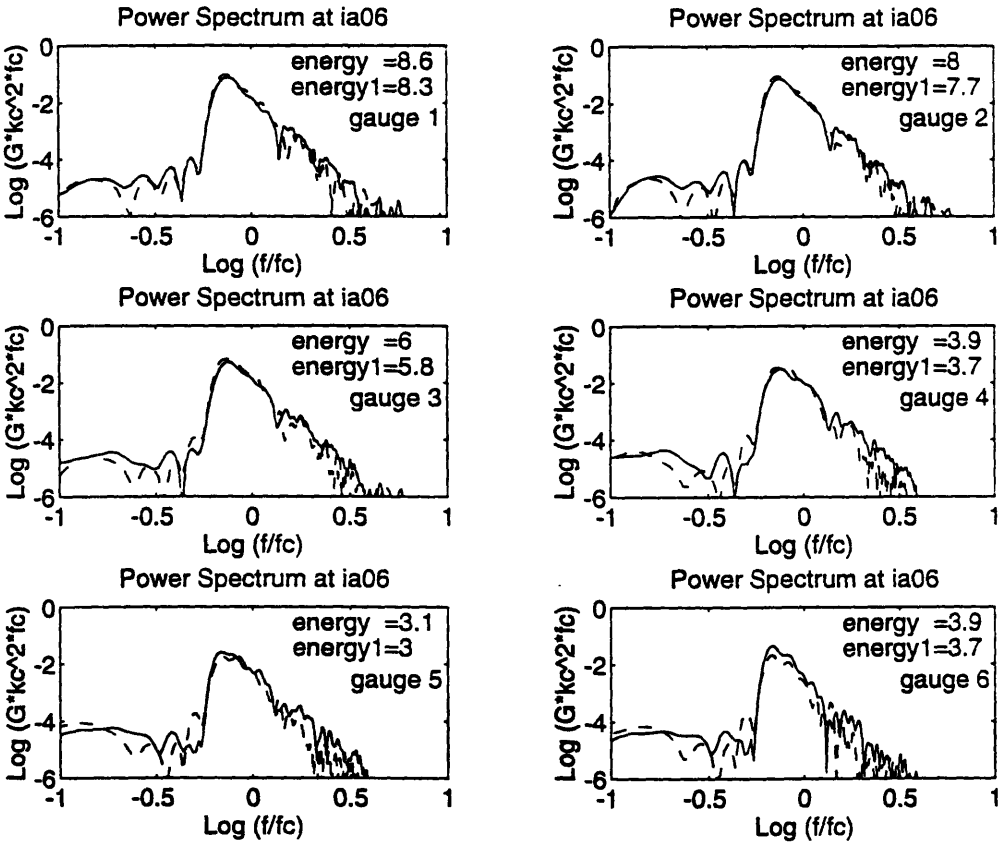
Power Spectrum at ia06
energy =8.6
energy1=8.3
gauge 1
Log (G*kc^2*fc)
Log (f/fc)
Power Spectrum at ia06
energy =8
energy1=7.7
gauge 2
Log (G*kc^2*fc)
Log (f/fc)
Power Spectrum at ia06
energy =6
energy1=5.8
gauge 3
Log (G*kc^2*fc)
Log (f/fc)
Power Spectrum at ia06
energy =3.9
energy1=3.7
gauge 4
Log (G*kc^2*fc)
Log (f/fc)
Power Spectrum at ia06
energy =3.1
energy1=3
gauge 5
Log (G*kc^2*fc)
Log (f/fc)
Power Spectrum at ia06
energy =3.9
energy1=3.7
gauge 6
Log (G*kc^2*fc)
Log (f/fc)

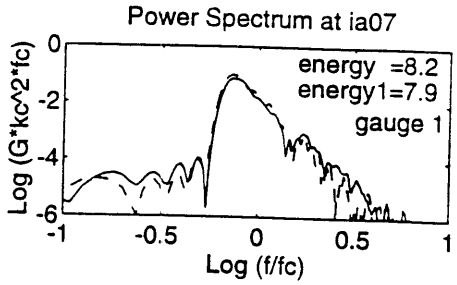
Power Spectrum at ia07
energy =8.2
energy1=7.9
gauge 1
Log (G*kc^2*fc)
Log (f/fc)

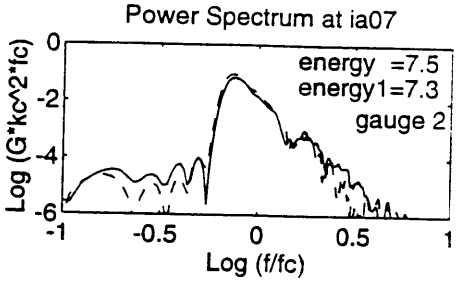
Power Spectrum at ia07
energy =7.5
energy1=7.3
gauge 2
Log (G*kc^2*fc)
Log (f/fc)

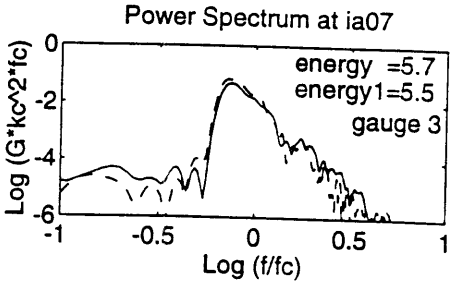
Power Spectrum at ia07
energy =5.7
energy1=5.5
gauge 3
Log (G*kc^2*fc)
Log (f/fc)

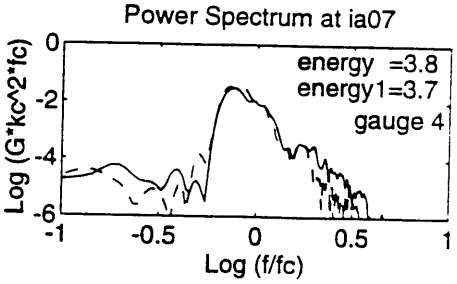
Power Spectrum at ia07
energy =3.8
energy1=3.7
gauge 4
Log (G*kc^2*fc)
Log (f/fc)

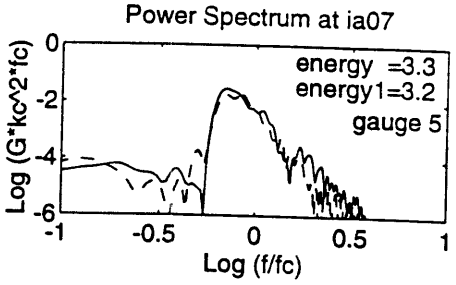
Power Spectrum at ia07
energy =3.3
energy1=3.2
gauge 5
Log (G*kc^2*fc)
Log (f/fc)

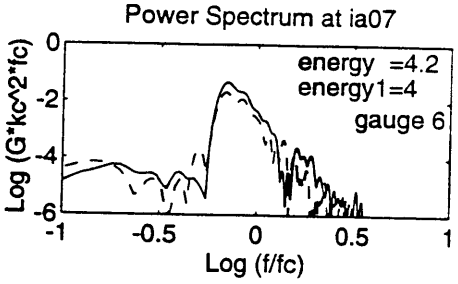
Power Spectrum at ia07
energy =4.2
energy1=4
gauge 6
Log (G*kc^2*fc)
Log (f/fc)

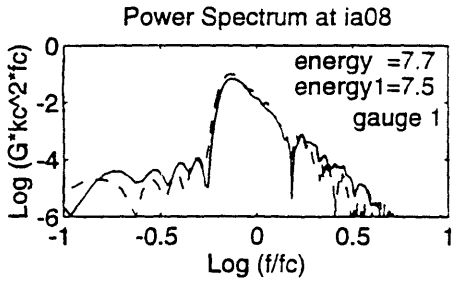
Power Spectrum at ia08
energy =7.7
energy1=7.5
gauge 1
Log (G*kc^2*fc)
Log (f/fc)

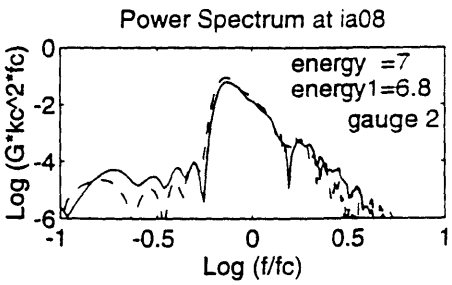
Power Spectrum at ia08
energy =7
energy1=6.8
gauge 2
Log (G*kc^2*fc)
Log (f/fc)

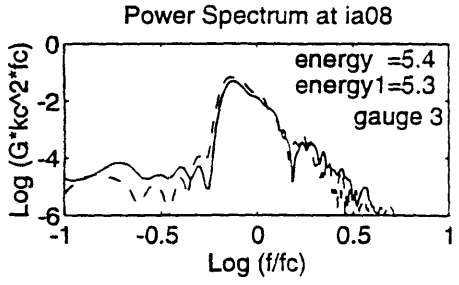
Power Spectrum at ia08
energy =5.4
energy1=5.3
gauge 3
Log (G*kc^2*fc)
Log (f/fc)

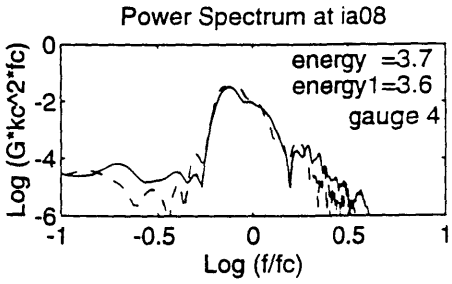
Power Spectrum at ia08
energy =3.7
energy1=3.6
gauge 4
Log (G*kc^2*fc)
Log (f/fc)

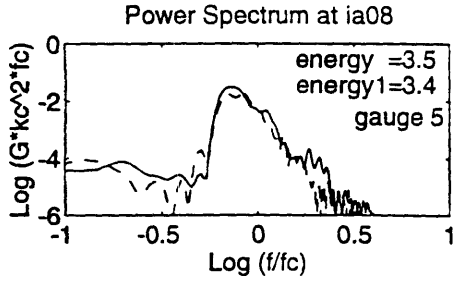
Power Spectrum at ia08
energy =3.5
energy1=3.4
gauge 5
Log (G*kc^2*fc)
Log (f/fc)

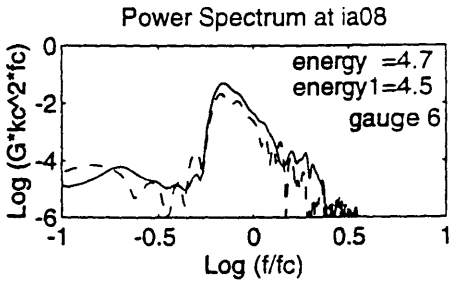
Power Spectrum at ia08
energy =4.7
energy1=4.5
gauge 6
Log (G*kc^2*fc)
Log (f/fc)

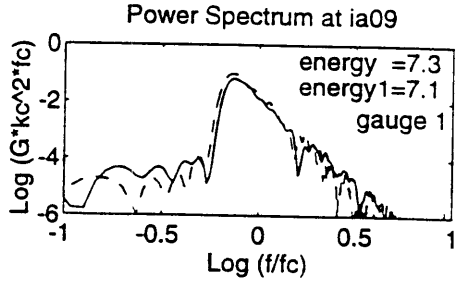
Power Spectrum at ia09
energy =7.3
energy1=7.1
gauge 1
Log (G*kc^2*fc)
Log (f/fc)

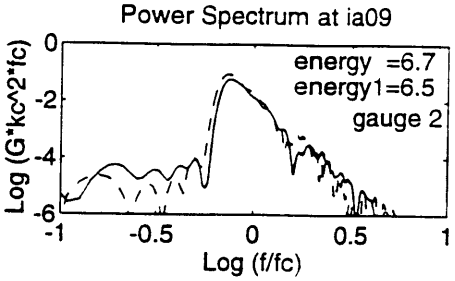
Power Spectrum at ia09
energy =6.7
energy1=6.5
gauge 2
Log (G*kc^2*fc)
Log (f/fc)

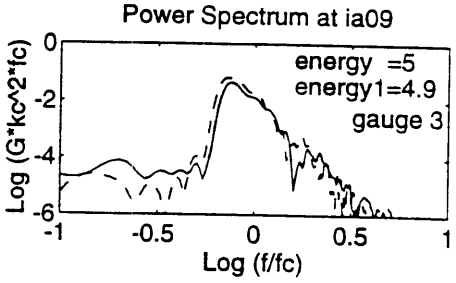
Power Spectrum at ia09
energy =5
energy1=4.9
gauge 3
Log (G*kc^2*fc)
Log (f/fc)

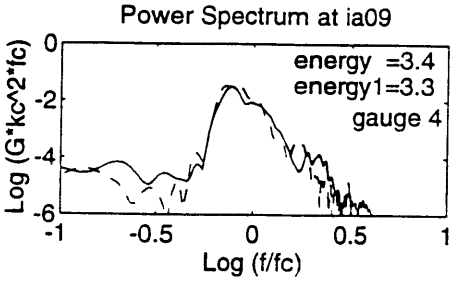
Power Spectrum at ia09
energy =3.4
energy1=3.3
gauge 4
Log (G*kc^2*fc)
Log (f/fc)

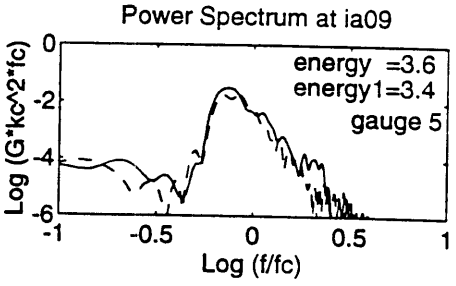
Power Spectrum at ia09
energy =3.6
energy1=3.4
gauge 5
Log (G*kc^2*fc)
Log (f/fc)

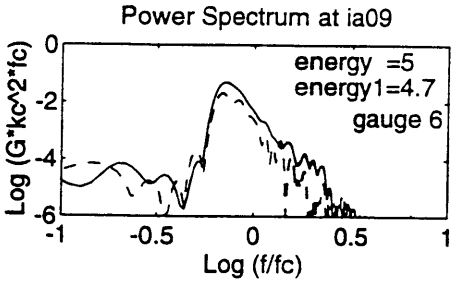
Power Spectrum at ia09
energy =5
energy1=4.7
gauge 6
Log (G*kc^2*fc)
Log (f/fc)

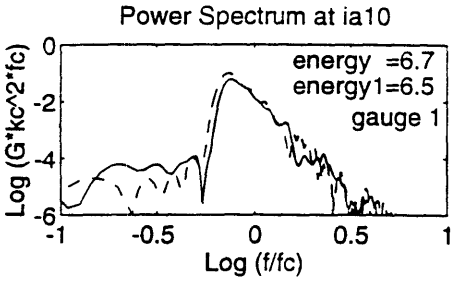
Power Spectrum at ia10
energy =6.7
energy1=6.5
gauge 1
Log (G*kc^2*fc)
Log (f/fc)

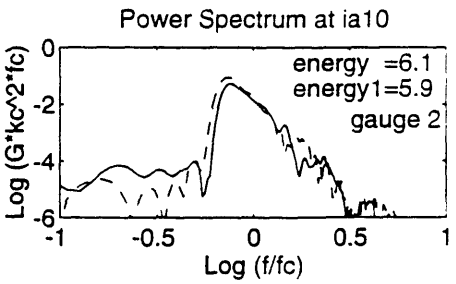
Power Spectrum at ia10
energy =6.1
energy1=5.9
gauge 2
Log (G*kc^2*fc)
Log (f/fc)

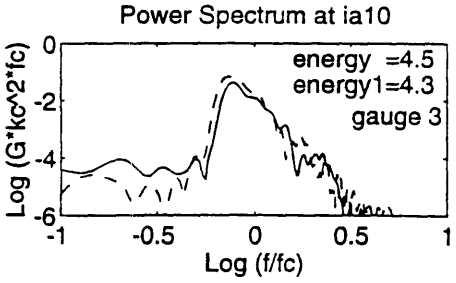
Power Spectrum at ia10
energy =4.5
energy1=4.3
gauge 3
Log (G*kc^2*fc)
Log (f/fc)

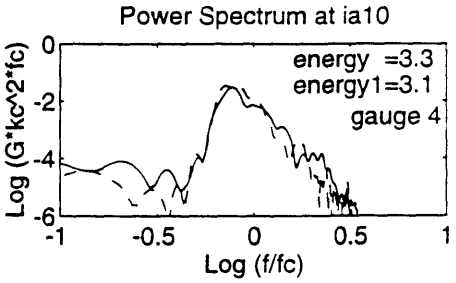
Power Spectrum at ia10
energy =3.3
energy1=3.1
gauge 4
Log (G*kc^2*fc)
Log (f/fc)

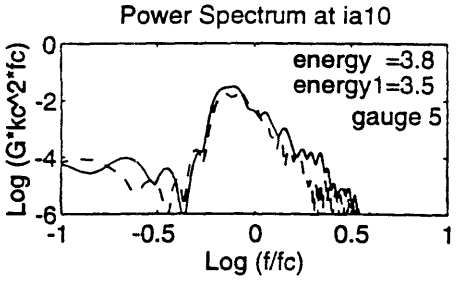
Power Spectrum at ia10
energy =3.8
energy1=3.5
gauge 5
Log (G*kc^2*fc)
Log (f/fc)

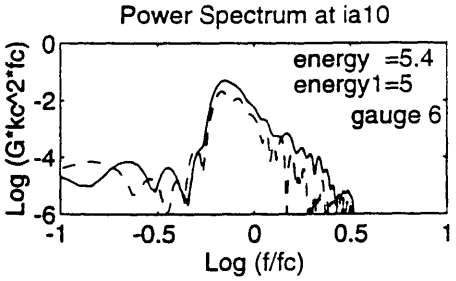
Power Spectrum at ia10
energy =5.4
energy1=5
gauge 6
Log (G*kc^2*fc)
Log (f/fc)

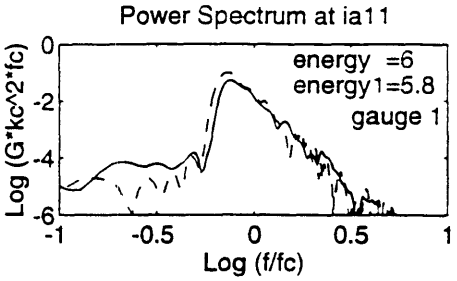
Power Spectrum at ia11
energy =6
energy1=5.8
gauge 1
Log (G*kc^2*fc)
Log (f/fc)

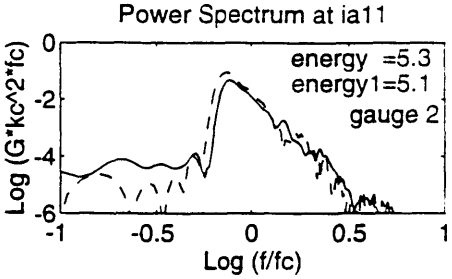
Power Spectrum at ia11
energy =5.3
energy1=5.1
gauge 2
Log (G*kc^2*fc)
Log (f/fc)

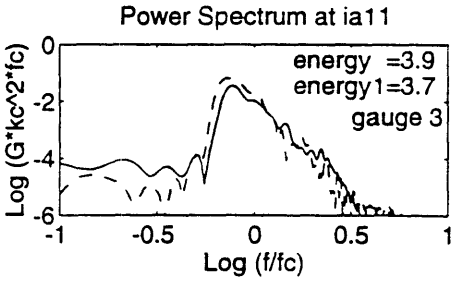
Power Spectrum at ia11
energy =3.9
energy1=3.7
gauge 3
Log (G*kc^2*fc)
Log (f/fc)

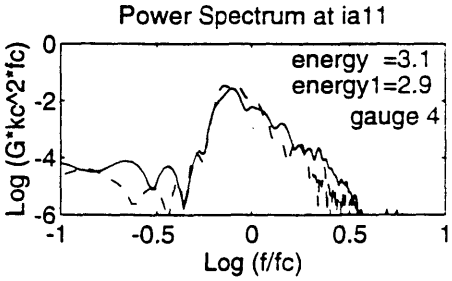
Power Spectrum at ia11
energy =3.1
energy1=2.9
gauge 4
Log (G*kc^2*fc)
Log (f/fc)

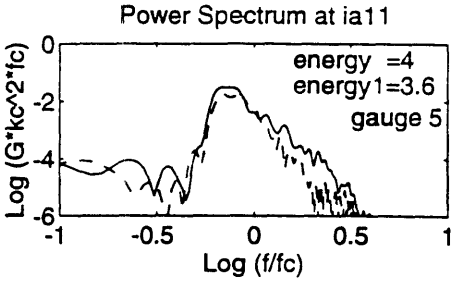
Power Spectrum at ia11
energy =4
energy1=3.6
gauge 5
Log (G*kc^2*fc)
Log (f/fc)

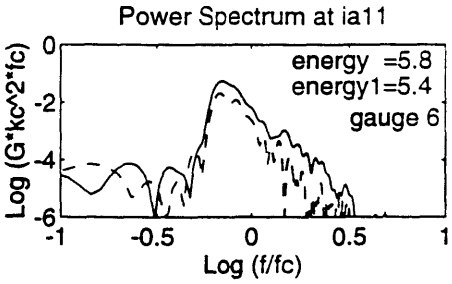
Power Spectrum at ia11
energy =5.8
energy1=5.4
gauge 6
Log (G*kc^2*fc)
Log (f/fc)